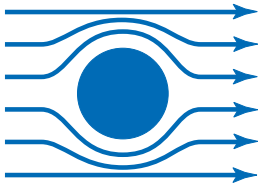

TECHNISCHE UNIVERSITÄT MÜNCHEN

WALTHER-MEIßNER-INSTITUT FÜR TIEF-TEMPERATURFORSCHUNG

BAYERISCHE AKADEMIE DER WISSENSCHAFTEN

Ferromagnetic Resonance at Low Temperatures

Diploma thesis

Christoph Zollitsch

Advisor: Prof. Dr. R. Gross

Garching, November 28, 2011

Challenge accepted!

Barney Stinson

Contents

This is gonna be legen — wait for it ...

Barney Stinson

Chapter 1.

Intoduction

As 1946 J. H. E. Griffiths [1] and E. K. Zavoiskii [2] independently reported on anomalous Larmor frequencies, observed in magnetic spectroscopy experiments in the microwave frequency range, a novel experimental method was born, today known as ferromagnetic resonance (FMR). This spectroscopy technique allows a variety of investigations on ferromagnetic or antiferromagnetic materials, such as magnetic anisotropies, magnetoelastics, and as investigated in this thesis, relaxation processes [3]. Typical, FMR experiments are performed down to low temperatures, specifically to the temperature of pumped helium of about 1 K [4]. Though, performing FMR below 1 K is interesting for the identification of the limiting damping mechanisms of magnetic systems, it is not common these days, due to the experimental challenges. The fundamental core of this is to take ferromagnetic resonance to the millikelvin regime, combining microwave broadband transmission spectroscopy with temperatures reached by a dilution refrigerator. Hereby, experiments in a temperature range of 40 mK to 50 mK were accomplished. Although, being limited to relatively low powers, these temperatures bring the advantage of a high signal to noise ratio, due to the suppression of the thermally excited background. Eventually hereby, solely the magnetic response of the excited system may be investigated. Chapter 4 introduces the newly established millikelvin FMR setup as well as shows initial experiments on the well known ferromagnetic material Cobalt.

The focus of Chapter 5 is upon the temperature dependence of the magnetic relaxation on the rare-earth impurity concentration of the magnetic system. Initially, the effect of RE impurities and impurity concentration on the magnetic damping was extensively studied in the ferrimagnetic insulator Yttrium Iron Garnet (YIG) [5]. Here, the RE impurities offer an additional path of relaxation for the magnetic system of

YIG, via an anisotropic exchange. This contribution to relaxation exhibits a strong temperature dependency, in particular for low temperatures, because relaxation can only take place when the RE dopant is thermally excited. In the beginnings of the new millennium it was demonstrated, that the doping of transition metals and transition metal alloys with RE elements also results in an increase of the magnetic damping [6], [7]. One particular system of interest is RE doped Permalloy, showing that the physical principle of RE induced line width broadening in YIG can also be transfered to Permalloy [8]. Since Permalloy finds many applications in modern magnetic storage technologies [8] or is used as spin injector in spin-valve measurements [9] an independent control of the magnetic damping is of great interest, because hereby the switching speed of the magnetic system can be tuned. The currently reported FMR line width measurements for various RE dopants and RE doping concentrations, have been performed in a temperature range between 350 K and 100 K. In Chapter 5 of this thesis the temperature range is extended to the millikelvin range for a thin film of Permalloy, doped with one atomic percent of the RE element Holmium. During the measurements in a very broad temperature range of 300 K to 50 mK, an up-to-now undocumented shift of the FMR by $\sim$ 14 GHz at low temperatures is observed and attributed to the ferromagnetic ordering of the RE dopant.

A second perspective of FMR in the millikelvin range is the possible access to quantum phenomena. The temperatures allow in principle to demote the number of photons in a cavity way below one, making single photon experiments possible. This experimental aspect is commonly used in the emerging field of circuit quantum electrodynamics (circuit QED), which investigates hybrid systems composed of artificial two-level systems called quantum bits (qubit) and harmonic oscillators, realized in form of superconducting (SC) microwave resonators [10]. Here, single photons interact with single atoms, which allow to study on a fundamental level the interaction of photons and matter. In these experiments it is mandatory that the coupling strength exceeds the present relaxation phenomena, which is the so-called strong coupling limit. If the hybrid system exhibits strong coupling, coherent superpositions of light and matter excitations can be achieved. This results in a system, where the levels are described by the number of photons and the ground and excited state of the two-level system. Such hybrid systems are appealing to quantum information processing, due to their fast processing speed and their customizability [11]. Nevertheless, storage of quantum states is limited to the lifetimes of the SC qubit or resonator, limited typically to μs

timescales [12]. Recently, spin ensembles are considered for storing quantum states by cavity-qubit hybrid systems [13], [14]. Here, the photon resonator acts as a relay between the spin ensemble and the qubit. For this purpose the coupling of the resonator and the spins is required to be strong. This is not the case for single spins. Although, by coupling a whole ensemble of spins to the resonator the strength is enhanced by the square root of the number of spins [13], as demonstrated for spin ensembles, consisting of individual non-interacting spins such as nitrogen-vacancy centers in diamond or Cr^{3+} in ruby [15], [16], [17], [18]. Unfortunately, the material hosting the independent spins, needs to be large in order to provide a sufficiently high number of spins, while keeping them individual. An alternaitve route is to allow the coupling between photons and exchange locked spin ensembles, as is proposed [19], [20]. Due to high spin density in such systems, the number of spins required for strong coupling could be integrated into small volumes, allowing to investigate multiple spin ensembles coupled to a single cavity. In the final chapter of this thesis a first experiment in this direction was performed on a SC coplanar microwave resonator-ferrimagnetic Galium doped YIG hybrid system. The coupling between the systems is experimentally investigated and, analyzing the relaxation rates of the resonator and the spin system it is concluded, that the system operates in the strong coupling regime.

When I get sad I stop being sad and be awesome instead. True story

Barney Stinson

Chapter 2.

Theory

This Chapter presents a fundamental description of the phenomenon of ferromagnetic resonance (FMR). The phenomenon is described by using the Landau-Lifshitz-Gilbert (LLG) equation as a theoretical characterization of the magnetization dynamics. Alternatively, the Bloch Bloembergen equation will be presented. These two equations introduce the magnetic relaxation process in different ways, focusing on differing damping mechanisms. The relevant damping mechanisms in metals will be discussed in relation to their significance. Using a free energy approach, the ferromagnetic resonance condition is calculated and the impact of additional terms contributing to the free energy is discussed. Based on the Landau-Lifshitz-Gilbert equation an expression for the magnetic susceptibility is derived, for the case of a thin film. Finally an introduction to the theory of superconducting microwave resonators will be given and a way their characteristic parameters can be calculated.

2.1. Principles of Ferromagnetic Resonance

Ferromagnetic resonance is a spectroscopy method to investigate the anisotropy properties of the magnetic system as well as its dynamics. Typically, the specimen is placed in a static magnetic field $\mathbf{H}_0$ and electromagnetic radiation is applied in the Gigahertz regime [3]. When the radiation is resonantly absorbed, the magnetic moment is tilted slightly out of the equilibrium position, resulting in a precessional motion. To understand the condition for magnetic resonance, solely the Zeeman effect is considered as a start. The effect splits electronic spin states into multiplets by application of a external static magnetic field $\mathbf{H}_0$ [3]. This is illustrated in Fig. 2.1 for a single electron. Here, the applied static field results in an (for positive g-factor) increase of

the spin-up ($m_j = +1/2$) and a lowering of the spin-down ($m_j = -1/2$) quantum state. The energy difference is given by

$$\Delta E = g\mu_{\mathrm{B}}\mu_0 \Delta m_j H_0, \tag{2.1}$$

where μ_{B} and μ_0 are the Bohr magneton and the vacuum permeability, respectively. Δm_{j} is the difference between the magnetic quantum numbers of the states in a multiplet. According to the section rules of dipole radiation, allowed transitions are found for [22]

$$\Delta m_j = 0,\ \pm 1. \tag{2.2}$$

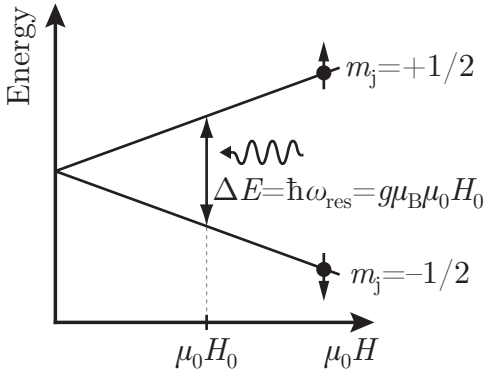

Figure 2.1.: Zeeman energy splitting with respect to the magnetic field H_0 [21].

Since only one quantum number may be occupied at the same time in any Zeeman multiplet, only transitions with $\Delta m_{\mathrm{j}} = \pm 1$ are of relevance. To induce such a transition, not only the polarization needs to be correct, the energy of the incident electromagnetic radiation also needs to be equal to the energy splitting ΔE. Hence, the spin system is excited, when the energy of the electromagnetic radiation used for the excitation matches the Zeeman splitting,

$$\hbar\omega = \Delta E = g\mu_{\mathrm{B}}\mu_0 \Delta m_j H_0. \tag{2.3}$$

Here, the reduced Planck constant $\hbar$ and the angular frequency ω of the electromagnetic radiation. By considering a specific transition with $\Delta m_{\mathrm{j}} = 1$, a universal relationship between radiation frequency ω and resonance field H_{res} can be obtained from Eqn. 2.3 [3]:

$$\omega_{\mathrm{res}} = \gamma\mu_0 H_0\ ; \quad \gamma = \frac{g\mu_{\mathrm{B}}}{\hbar}, \tag{2.4}$$

introducing the gyro magnetic ratio γ. For a single spin the resonant absorption of radiation would result in a flip of its magnetic moment. However, in FMR not only one spin is under investigation, but a whole ensemble of spins (Fig. 2.2(a)). Those are all linked together by the exchange interaction, bringing them into a precessional motion, by the magnetic field component $\mathbf{h}_1$ of the electromagnetic radiation (Fig. 2.2(b),(c)). The precessional motion of the individual magnetic moments present in the sample is characterized by the lamor-frequency [23]. The phase between the moments may

be, but must not necessarily be phase locked, compare with Fig. 2.2(b),(c). This phenomenon is identified as a quasi-particle, the so-called magnon or spin wave and consequently a wave vector $\mathbf{q}$ can be assigned to it. If the phase is locked, the excitation is described as a uniform mode with wave vector $\mathbf{q} = 0$, which is the typical form of excitation in a homogeneous static magnetic field and a homogeneous electromagnetic field* (Fig. 2.2(b)). Modes with a wave vector $\mathbf{q} \neq 0$ are preferentially excited with inhomogeneous microwave magnetic fields (Fig. 2.2(c)). In contrast to the system of a single spin, described in (2.4), in magnetic media the magnetization

*electromagnetic field = microwave

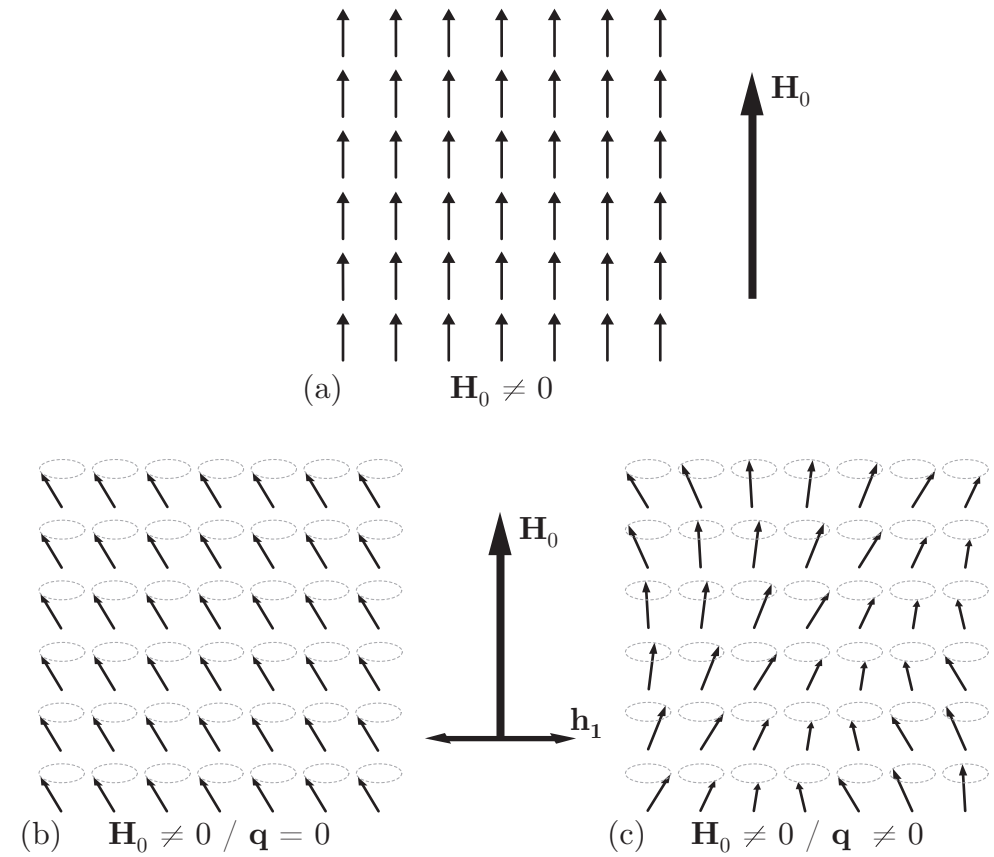

Figure 2.2.: Principle procedures for FMR, by means of a two dimensional ferromagnet. (a) ferromagnet completely magnetized by an externally applied static magnetic field $\mathbf{H}_0$. (b) precessing magnetic moments induced by an alternating magnetic field $\mathbf{h}_1$ applied in a plane perpendicular to $\mathbf{H}_0$. The motion is phase locked, representing a uniform mode ($\mathbf{q} = 0$). (c) non uniform precessing magnetic moments ($\mathbf{q} \neq 0$).

$\mathbf{M}$ of the sample adds up with the externally applied magnetic field,

$$\mu_0\mathbf{H}_0 \Leftarrow 1 \text{ spin } \Longleftrightarrow \text{ magnetic system} \Rightarrow \mathbf{B}_0 = \mu_0(\mathbf{M} + \mathbf{H}_0), \tag{2.5}$$

described by the magnetic induction $\mathbf{B}_0$. This leads to a significant modification of (2.4). Here, the interactions predominant in a ferromagnet, such as demagnetization fields and anisotropies, contribute to the resonance condition (cf. Sec. 2.3). Up to now we have only considered the energetical argument for the description of FMR. This allows to account for the resonance conditions, but not for e.g. the line width of the absorption spectra. The line width allows the extraction of the damping rate and mechanism on which this thesis concentrates.
To include these effects, an equation of motion for the precessing magnetic moments is introduced, that will be presented in the next section.

2.2. Landau-Lifshitz and Gilbert Equation

To describe a many body system, like all the magnetic moments of a ferromagnetic sample, a suitable model has to be developed. Since in FMR the magnetic system is homogeneously magnetized along an externally applied static magnetic field $\mathbf{H}_0$, a magnetization vector $\mathbf{M}$ can be defined, that is the vector sum of the magnetic moments $\mathbf{m}$ per unit volume V [3]. This reduces a many body problem to a single body problem, describing the system as one giant molecule with the magnetization $\mathbf{M}$, the so-called macrospin. The macrospin can be seen in analogue to a spinning top. A displacement from the rotation axis leads to a torque, which results in a precession around the initial rotation axis. This hold for the macrospin as well. Here, the displacement is triggered by the alternating magnetic field $\mathbf{h}_1$. Atomic theory relates the excitation to a definite polarization of $\mathbf{h}_1$, relative to the axis of quantization. There is only an excitation if $\mathbf{h}_1$ is polarized in a plane perpendicular to the axis of quantization, i.e. the direction of $\mathbf{H}_0$ [3]. L. D. Landau and E.M. Lifshitz described this by the phenomenological Landau-Lifshitz (LL) equation [24]:

$$\frac{\mathrm{d}\mathbf{M}}{\mathrm{d}t} = -\gamma\mu_0\mathbf{M} \times \mathbf{H}_{\text{eff}}, \tag{2.6}$$

with

$$\mathbf{H}_{\text{eff}} = \mathbf{H}_0 + \mathbf{h}_1 + \hat{\mathbf{N}}\mathbf{M}. \tag{2.7}$$

In Sec. 2.5 the driving imposed by $\mathbf{h}_1$ on the magnetization will be discussed and shown, that $\mathbf{h}_1$ induces a motion of the magnetization vector. (2.7) replaces the external applied field $\mathbf{H}_0 + \mathbf{h}_1$ by an effective internal magnetic field $\mathbf{H}_{\text{eff}}$. Inside the ferromagnetic sample the externally applied fields are modified by the demagnetization field. It depends on the shape of the sample and is characterized by the demagnetization tensor:

$$\hat{\mathbf{N}} = \begin{pmatrix} N_{xx} & N_{xy} & N_{xz} \\ N_{yx} & N_{yy} & N_{yz} \\ N_{zx} & N_{zy} & N_{zz} \end{pmatrix}, \tag{2.8}$$

that fulfills the identity:

$$\text{tr}(\hat{\mathbf{N}}) = N_{\text{xx}} + N_{\text{yy}} + N_{\text{zz}} = 1. \tag{2.9}$$

For ellipsoidal shaped samples $\hat{\mathbf{N}}$ reduces to a diagonal matrix [25]. Equation 2.7 describes a free precession of the magnetization around $\mathbf{H}_{\text{eff}}$, conserving the length of $\mathbf{M}$ and the angle between $\mathbf{M}$ and $\mathbf{H}_{\text{eff}}$. The latter results in an infinitely long magnetization precession, if it is once excited. To account for the relaxation of the magnetization a phenomenological damping was introduced to the LL equation by L. D. Landau and E.M. Lifshitz [24]. It was further modified by T. L. Gilbert, who considered a damping similar to the viscous damping in classical mechanics [26], yielding the Landau-Lifshitz-Gilbert (LLG) equation:

$$\frac{\mathrm{d}\mathbf{M}}{\mathrm{d}t} = -\gamma\mu_0(1+\alpha^2)[\mathbf{M} \times \mathbf{H}_{\text{eff}}] - \frac{\alpha}{M_{\text{S}}}[\mathbf{M} \times \frac{\mathrm{d}\mathbf{M}}{\mathrm{d}t}], \tag{2.10}$$

with the saturation magnetization M_{S} and the dimensionless damping parameter α. M_{S} is the length of the magnetization vector $\mathbf{M}$, when all magnetic moments point in the same direction, as it is considered in the macrospin model. Equation 2.10 is depicted in Fig. 2.3. The first term of the right hand side of the LLG equation describes the precession, the second the relaxation. The damping term acts perpendicular on the magnetization in the direction of the equilibrium position, i.e. a position parallel to $\mathbf{H}_{\text{eff}}$, resulting in a spiral motion into equilibrium.

The LLG equation thus allows to describe the precessional motion of the system including damping processes with a damping parameter α. In Chapter 4 this ansatz is used to characterize the damping rate and investigate the damping mechanism present.

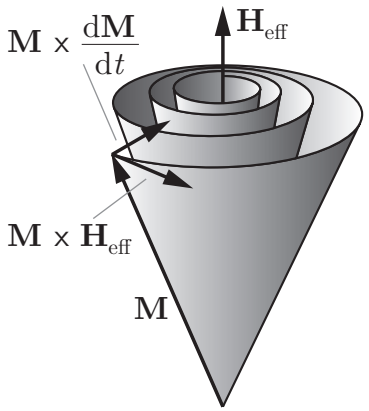

Figure 2.3.: Schematic of a excited magnetization relaxing back into equilibrium, including the directions of the torques acting on the vector **M** [21].

2.2.1. Bloch Bloembergen Equation

An alternative to the LLG equation is the ansatz by Felix Bloch [27]. Here, damping and relaxation is parametrized in form of two lifetimes, allowing to directly address the lifetimes of the spin waves. Originally this equation was intended to describe relaxation processes in nuclear magnetic resonance [3]. Since the macrospin model is equivalent to this picture, Bloch's equation is also suitable to describe magnetization dynamics.

$$\frac{\mathrm{d}\mathbf{M}}{\mathrm{d}t} = -\gamma\mu_0[\mathbf{M}\times\mathbf{H}_0] - \frac{M_\mathrm{x}}{T_2}\hat{\mathbf{x}} - \frac{M_\mathrm{y}}{T_2}\hat{\mathbf{y}} - \frac{M_\mathrm{z}-M_0}{T_1}\hat{\mathbf{z}}\ ; \quad \mathbf{M} = \begin{pmatrix} M_\mathrm{x} \\ M_\mathrm{y} \\ M_\mathrm{z} \end{pmatrix}. \tag{2.11}$$

Here, $(\hat{\mathbf{x}}, \hat{\mathbf{y}}, \hat{\mathbf{z}})$ denote the unit vectors of the Cartesian coordinate system used, M_0 is the strength of the equilibrium magnetization [28]. Bloch's equation describes the precession in the same way as the LL equation, but treats relaxation differently, introducing the longitudinal and transverse relaxation times T_1 and T_2. Despite having two parameters at hand N. Bloembergen first used Eqn. 2.11 [29], with the assumption

$$\frac{1}{T_2} = \frac{1}{2T_1} + \frac{1}{T_2^*}. \tag{2.12}$$

to interpret FMR spectra. The introduction of two relaxation times allows to distinguish between energetical or spin-lattice relaxation (T_1) and spin-spin relaxation (T_2),

where energy is conserved and phase conservation is probed [27]. Since the precessional term in equation 2.11 includes only the external static magnetic field $\mathbf{H}_0$, no excitation is expected at $\mathbf{H}_0 = 0$. In contrast, this is experimentally observed. The instantaneous magnetic field of a ferromagnet is sufficient to quantize the system, allowing FMR at zero external field $\mathbf{H}_0$. Codrington, Olds and Torrey modified Bloch's equation in a way, that the equilibrium position is not defined by $\mathbf{H}_0$, instead it is determined by the instantaneous magnetic field [30]:

$$\frac{\mathrm{d}\mathbf{M}}{\mathrm{d}t} = -\gamma\mu_0[\mathbf{M}\times\mathbf{H}_{\mathrm{eff}}] - \frac{1}{T_2}(\mathbf{M} - \frac{(\mathbf{M}\cdot\mathbf{H}_{\mathrm{eff}})\mathbf{H}_{\mathrm{eff}}}{{\mathbf{H}_{\mathrm{eff}}}^2}) + \frac{1}{T_1}(\chi_0\mathbf{H}_{\mathrm{eff}} - \frac{(\mathbf{M}\cdot\mathbf{H}_{\mathrm{eff}})\mathbf{H}_{\mathrm{eff}}}{{\mathbf{H}_{\mathrm{eff}}}^2}), \quad (2.13)$$

with the magnetic susceptibility $\chi_0 = {}^{M_0}/_{H_0}$. This equation leaves the length of magnetization $\mathbf{M}$ not constant during the excitation. In the case of equal relaxation times, $T_1 = T_2 = \tau$, Eqn. 2.13 reduces to

$$\frac{\mathrm{d}\mathbf{M}}{\mathrm{d}t} = -\gamma\mu_0[\mathbf{M}\times\mathbf{H}_{\mathrm{eff}}] - \frac{\mathbf{M}}{\tau} + \frac{\chi_0\mathbf{H}_{\mathrm{eff}}}{\tau}, \quad (2.14)$$

and is known as the Bloch-Bloembergen (BB) equation [3]. The last two terms on the right side of (2.14) are responsible for damping. Effectively the two terms only contain the dynamic parts of $\mathbf{M}$ and $\mathbf{H}_{\mathrm{eff}}$, while the static parts cancel out over the relation $\chi_0 = {}^{M_0}/_{H_0}$. (2.13) and (2.14) are alternatives to the LLG equation (2.10), when there is need to express the relaxation directly by relaxation times T_1, T_2 and not by the Gilbert damping parameter α.

2.3. Magnetic Damping Mechanisms in Metals

There are several mechanisms contributing to the magnetic damping in metals, phenomenologically described by the Gilbert damping parameter α (cf. Sec. 2.2). There are two main categories, intrinsic and extrinsic damping. Intrinsic effects are indirectly dependent on the sample material via phonons and thermally excited spin waves. They perturb the intrinsic effects such as inter- and intralayer exchange coupling, dipole-dipole interaction and magnetic anisotropies. In general, all relaxation processes involving electron scattering on phonons and thermally excited spin waves are called intrinsic, because they are an integral part of the system [31]. Extrinsic effects involve structural defects, the shape of the sample or the measurement geometry, i.e. avoidable contributions by proper sample preparation [31].

Intrinsic Damping

One intrinsic damping reason are by an alternating magnetic field induced currents. These so called eddy currents create a magnetic field by themselves, influencing the magnetization precession during FMR. The magnetic damping by eddy currents is proportional to the square of the sample thickness, their contribution can be neglected for ultra thin metallic films, which is the case for the metallic samples under investigation in this thesis [31].
The direct interaction of spin waves with phonons also leads to a contribution to the intrinsic damping, which is known as Phonon drag. The effect is notable if the excited elastic wave establishes a resonant mode across the sample thickness at, or near, the FMR field. For a sample thickness smaller than half of the wavelength of the elastic wave, the phonon drag is negligible [31].
The observed damping originates mainly from spin-orbit relaxations. It is described by the interaction between the spin density of the itinerant electrons and the spins of the localized electrons. When performing a FMR experiment the localized spins are brought into precession, i.e. spin waves are excited. The created spin waves are scattered coherently at the itinerant electrons, via the exchange interaction between the itinerant and localized electrons. During the process electron-hole pairs are created. The total angular momentum during the exchange interaction is conserved, including an appropriate spin-flip of the scattered electron. The coherent scattering does not lead to magnetic damping, since there is no energy dissipation from the spin system. The damping is caused by a disruption of the coherent scattering. Other excitations, e.g. thermally excited phonons or spin waves, scatter incoherently with the created spin-flipped electron-hole pairs, by spin-orbit interaction. On this way the excited spin system dissipates energy via incoherent scattering and thus relaxing back into equilibrium [31]. This damping mechanism depends on the initial energy of the spin wave and thus on the RF radiation frequency. There is a direct proportionality between damping rate and excitation frequency, which is characteristic for Gilbert damping [3], [31].

Extrinsic Damping

Extrinsic damping is the scattering of the spin waves, excited by FMR, at inhomogeneous magnetic properties. Such properties include inhomogeneous anisotropies at

the surface or the bulk of a sample or magnetic defects. The scattering process can be seen analogous to electron or phonon scattering. If the periodicity of the magnetic lattice, seen by the spin waves, is changed due to magnetic defects, the spin waves are scattered. During this process energy is dissipated to the lattice, leading to an increase in damping.
Two magnon scattering also contributes to the magnetic damping, albeit it is no direct damping process, but a mode conversion. The excited spin waves, consisting of a uniform mode with wave vectors $\mathbf{q} \sim 0$, are scattered into non uniform modes with $\mathbf{q} \neq 0$. Therefore the magnetic excitation does not relax, the energy is shifted into other modes. These will equilibrate by means of intrinsic damping effects. The mode conversion leads to a de-phasing of the uniform mode, reducing the FMR signal. The reason for two magnon scattering is a degeneracy of the uniform FMR mode for an in-plane magnetized thin film with inhomogeneous anisotropies. The dispersion relation $\omega(\mathbf{q})$ for the in-plane spin waves has an initial negative slope, followed by a minimum [31], [32]. For one given frequency, and hence energy, there will be two possible wave vectors, one with $\mathbf{q} \sim 0$ and one with $\mathbf{q} \neq 0$. If the magnetization is tilted in the out of plane direction, the degeneracy reduces, to a complete lift of the degeneracy for a perpendicular magnetization.

2.4. Magnetic Free Energy

As established in Sec. 2.2, for a successful description of a FMR experiment an expression for the resonance condition is required. Using the free energy F of the magnetic system this can be accomplished. The derivation shall be outlined in this section, a full derivation can be found in Ref. [3]. The static effective magnetic field inside the ferromagnetic sample $\mathbf{H}_{\text{eff}}$ is given by the derivative of the free energy [33], [3]:

$$\mathbf{H}_{\text{eff}} = -\frac{1}{\mu_0}\frac{\partial F}{\partial \mathbf{M}} = -\frac{1}{\mu_0}\left(\frac{\partial F}{\partial M}\hat{\mathbf{e}}_M + \frac{1}{M\sin\Theta}\frac{\partial F}{\partial \Phi}\hat{\mathbf{e}}_\Phi + \frac{1}{M}\frac{\partial F}{\partial \Theta}\hat{\mathbf{e}}_\Theta\right). \tag{2.15}$$

Spherical coordinates were used to express Eqn. 2.15, with $\hat{\mathbf{e}}_M$, $\hat{\mathbf{e}}_\Phi$ and $\hat{\mathbf{e}}_\Theta$ representing the unit vectors. Φ and Θ are the azimuthal and polar angle of the magnetization vector $\mathbf{M}$, as defined in Fig. 2.4. The magnetic field $\mathbf{H}_{\text{eff}}$ consists in its simplest form of the external applied static magnetic field $\mathbf{H}_0$, but may be superimposed by

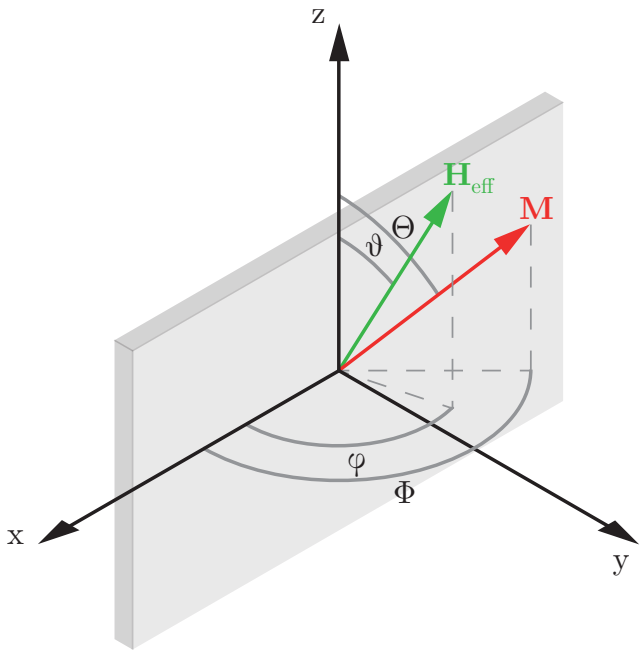

Figure 2.4.: Coordinate system and outlining of the orientation of the sample and a general direction of its magnetization **M** relative to the magnetic field $\mathbf{H}_{\text{eff}}$.

internal demagnetization or anisotropy fields. $\mathbf{H}_{\text{int}}$ dictates the equilibrium position of the magnetization **M**. If the magnetization is in equilibrium, the free energy F is minimal. This is satisfied, when the azimuthal and polar components of Eqn. 2.15 are zero, resulting in an equilibrium orientation of the magnetization in $\hat{\mathbf{e}}_M$ direction. The equilibrium position is perturbed by the alternating magnetic field $\mathbf{h}_1$. The perturbation is assumed to be small, since $\mathbf{h}_1$ is much weaker than the static internal magnetic field $\mathbf{H}_{\text{int}}$. That allows a expansion of the angular derivatives of Eqn. 2.15, and such are related with the equations of motions for the azimuthal and polar angle, obtained from the LLG equation in spherical coordinates. The result is a set of differential equations, whose periodic solution ω yields an expression for the resonance condition [3]:

$$\omega^2 = \omega_{\text{res}}^2 + i\omega\Delta\omega, \tag{2.16}$$

with the resonance frequency or dispersion relation

$$\omega_{\text{res}}^2 = \frac{\gamma^2(1+\alpha^2)}{M_S^2 \sin^2\Theta_0}\left(\left.\frac{\partial^2 F}{\partial\Phi^2}\right|_{\Phi_0}\left.\frac{\partial^2 F}{\partial\Theta^2}\right|_{\Theta_0} - \left(\left.\frac{\partial^2 F}{\partial\Theta\partial\Phi}\right|_{\Theta_0\Phi_0}\right)^2\right), \tag{2.17}$$

and the absorption line width

$$\Delta\omega = \left(\frac{\mathrm{d}\omega}{\mathrm{d}H_{\mathrm{int}}}\right)\Delta H = \frac{\gamma\alpha}{M}\left(\left.\frac{\partial^2 F}{\partial\Theta^2}\right|_{\Theta_0} + \frac{1}{\sin^2\Theta_0}\left.\frac{\partial^2 F}{\partial\Phi^2}\right|_{\Phi_0}\right). \tag{2.18}$$

Θ_0 and Φ_0 are the angles of the equilibrium position of $\mathbf{M}$. The equations 2.17 and 2.18 are general expressions, not specifying the free energy F. The free energy F can be written as a sum of energies, each considering another part of the magnetic system [3]:

$$\begin{aligned} F &= F_{\mathrm{Zeeman}} + F_{\mathrm{demagnetization}} + F_{\mathrm{anisotropy}} = \\ &= -\mu_0\mathbf{M}\mathbf{H}_0 + \frac{1}{2}\mu_0\mathbf{M}\hat{\mathbf{N}}\mathbf{M} + K_{\mathrm{uni}}\left(\frac{\mathbf{M}}{M_{\mathrm{S}}}\mathbf{u}\right)^2. \end{aligned} \tag{2.19}$$

F_{Zeeman} is the Zeeman energy of the external applied field $\mathbf{H}_0$. The demagnetization energy $F_{\mathrm{demagnetization}}$ represents the dipole-dipole interaction of $\mathbf{H}_0$ with the magnetization and is also called the form anisotropy. $F_{\mathrm{anisotropy}}$ contains the magnetocrystaline and surface anisotropy energies, which are caused by the spin-orbit interaction [34]. Equation 2.19 gives specific expressions for the free energy terms, using the coordinate system depicted in Fig. 2.4. For the anisotropy contribution $F_{\mathrm{anisotropy}}$ an uniaxial crystal anisotropy is chosen called F_{uniaxial}. With the uniaxial anisotropy constant K_{uni} and its uniaxial anisotropy axis $\mathbf{u}$ along the x-direction [21]. F_{uniaxial} is maximal, when the magnetization points along this axis, i.e. the energetically most unfavorable direction for the magnetization to point. The magnetic film is extended in the x-z-plane, resulting in a demagnetization tensor $\hat{\mathbf{N}}$ consisting only of one non zero element, $N_{\mathrm{yy}} = 1$. Therefore, $F_{\mathrm{demagnetization}}$ has its maximum, when the magnetization is aligned perpendicular to the film surface, which is called the out-of-plane (oop) direction and is minimal for the magnetization lying in the film plane, the so-called in-plane (ip) direction. The modularity of the free energy F makes the Eqn. 2.17 and 2.18 adaptable for different contributions to the magnetic system. The impact of the mentioned energies contributing to the free energy F on the resonance frequency ω_{res} are shown in Fig. 2.5. The calculations were carried out for a thin ferromagnetic film, infinitely expanded in the x-z-plane (cf. Fig. 2.4). With a saturation magnetization $\mu_0 M_{\mathrm{S}}$ of 1 T, a g-factor of 2, the Gilbert damping parameter α was chosen to 0.01 and an uniaxial anisotropy constant K_{uni} of 100 mT was chosen.
Figure 2.5 (b) shows clearly, that the form anisotropy present in the sample alters the

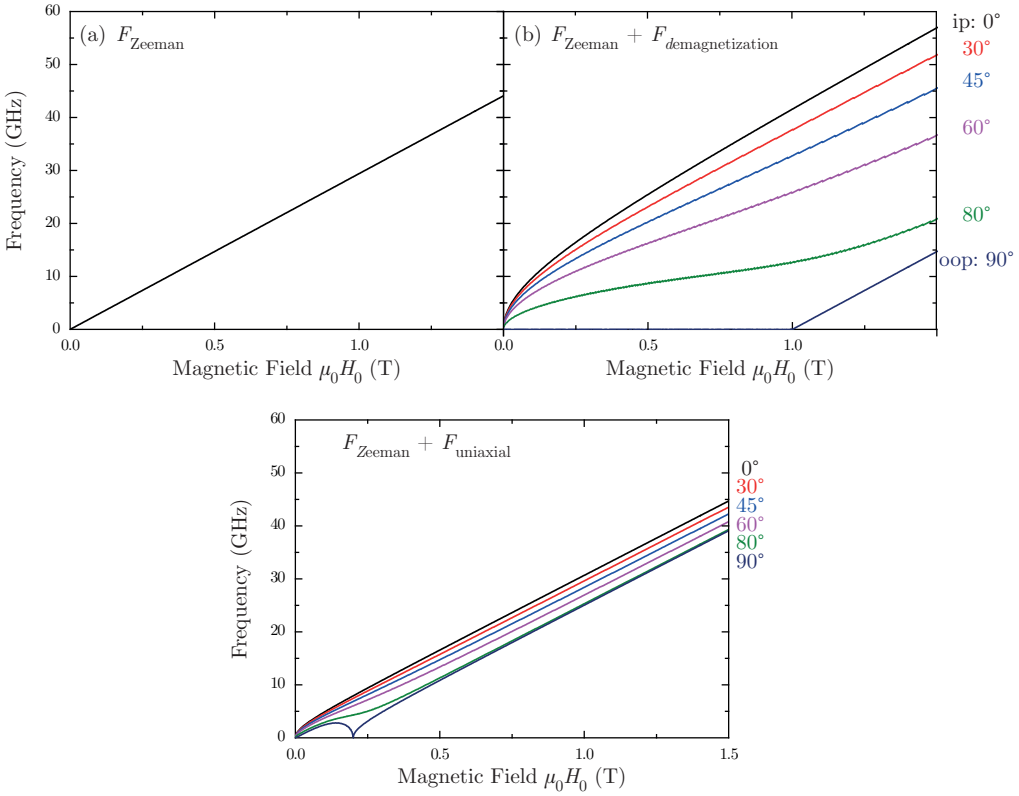

Figure 2.5.: Calculated resonance frequency as a function of the magnetic field and orientation from (2.17), for a thin film in the x-z-plane. (a) shows the dispersion considering only the Zeeman term of the free energy F.(b) the demagnetization energy introduces an angle dependence of the dispersion. The angles represent the direction of the static magnetic field $\mathbf{H}_0$, relative to the film surface. (c) considering the Zeeman term and an uniaxial anisotropy, with its uniaxial anisotropy axis $\mathbf{u}$ pointing along the x-direction. The angle is defined between $\mathbf{u}$ and the static magnetic field $\mathbf{H}_0$, both oriented ip.

dependence of the resonance frequency as a function of the magnetic field significantly. While for an ip configuration the external magnetic field $\mathbf{H}_0$ is "supported" by the internal demagnetization field, resulting in a higher resonance frequency than observed for the Zeeman term. In the oop configuration no resonance is observed until the external magnetic field exceeds the saturation magnetization. Above this threshold the slope for the Zeeman energy is recovered and can be used to determine the g-factor of the material system.

Figure 2.5 (c) adds an in-plane uniaxial anisotropy to the magnetic thin film, along the x-direction ($\mathbf{u} \parallel \hat{\mathbf{x}}$). The anisotropy creates a magnetic field, aligning the magneti-

zation along the magnetic easy axis, the axis perpendicular to the uniaxial anisotropy axis **u**. When a static magnetic field $\mathbf{H}_0$ is applied ip, perpendicular to **u**, it is enhanced by the anisotropy field and this results in a higher resonance frequency, compared to the resonance frequency obtained with only considering the Zeeman term. When the magnetic field $\mathbf{H}_0$ is applied parallel to **u**, the direction of the magnetization is first only defined by the anisotropy field. As $\mathbf{H}_0$ increases, the magnetization is slightly canted out of the magnetic easy axis. Due to the large angle between $\mathbf{H}_0$ and **M** the resonance frequency increases slower, compared with the pure Zeeman dispersion. At a certain magnetic field strength, it becomes favorable for the magnetization to align itself in the direction of $\mathbf{H}_0$. From there on the anisotropy field effectively works against the external field. The resonance frequency reduces until the external field H_0 compensates the anisotropy field. Increasing H_0 further, the resonance frequency rises, with the same slope as in the perpendicular alignment.

2.5. FMR Line Shape

Analyzing the observed line shape and width of FMR yields information about the system under investigation. This task can be approached from two sides: (i) the external magnetic field as constant and the excitation frequency is varied and (ii) the microwave frequency is kept constant and the external magnetic field is altered. Both approaches provide the resonance frequency or field through the position of the absorption dip. From (2.18) the line widths $\Delta\omega$ or ΔH, which are given by the full width at half maximum (FWHM) of the absorption dip, allow to extract the Gilbert damping parameter when plotted against the external constant parameter. To establish a relationship between the line width and damping parameter α, the LLG equation 2.10 is solved [3], [34]:

$$\Delta\omega = \left(\frac{\mathrm{d}\omega}{\mathrm{d}H_{\mathrm{int}}}\right)\Delta H \tag{2.20}$$

$$\mu_0\Delta H(\omega) = \mu_0\Delta H(0) + 2\alpha\frac{\omega}{\gamma}. \tag{2.21}$$

The Gilbert damping parameter α is determined by the slope of (2.21). The constant offset $\Delta H(0)$ is not accounted for in the derivation of $\Delta H(\omega)$ and is added afterwards. Its origin arises solely from extrinsic damping effects. In general, α can be composed

of both intrinsic and extrinsic damping, e.g. due to two magnon scattering.
A theoretical expression of the measured FMR line shape, including the line width, is needed. Such an expression can be obtained from the scalar magnetic susceptibility χ. A derivation shall be given now.
It is assumed, that the alternating field $\mathbf{h}_1$ acts as a small time dependent perturbation on the equilibrium magnetization $\mathbf{M}_0$, resulting in a small displacement. Magnetic field and magnetization are separated in static and time dependent components:

$$\mathbf{H}_{\text{eff}} = \mathbf{H}_0 + \mathbf{h}_1(t) = \begin{pmatrix} H_0 \\ h_{\text{y}}(t) \\ h_{\text{z}}(t) \end{pmatrix} \; ; \; \mathbf{M}_{\text{eff}} = \mathbf{M}_0 + \mathbf{m}(t) = \begin{pmatrix} M_{\text{S}} \\ m_{\text{y}}(t) \\ m_{\text{z}}(t) \end{pmatrix}. \tag{2.22}$$

These fields are inserted into the LLG equation (2.10):

$$\begin{aligned} \frac{\mathrm{d}\mathbf{m}(t)}{\mathrm{d}t} = & - \gamma\mu_0 \underbrace{(1+\alpha^2)}_{\approx 1}[\underbrace{\mathbf{M}_0 \times \mathbf{H}_0}_{=0;\ \mathbf{M}_0 \| \mathbf{H}_0} + \mathbf{M}_0 \times \mathbf{h}_1(t) + \mathbf{H}_0 \times \mathbf{m}(t) + \underbrace{\mathbf{m}(t) \times \mathbf{h}_1(t)}_{\approx 0}] \\ & - \frac{\alpha}{M_{\text{S}}}[\mathbf{M}_0 \times \frac{\mathrm{d}\mathbf{m}(t)}{\mathrm{d}t} + \underbrace{\mathbf{m}(t) \times \frac{\mathrm{d}\mathbf{m}(t)}{\mathrm{d}t}}_{\approx 0}]. \end{aligned} \tag{2.23}$$

By assuming, that the sample is homogeneously magnetized by the static magnetic field $\mathbf{H}_0$ and neglecting any anisotropies, $\mathbf{M}_0$ will lie parallel to $\mathbf{H}_0$. This causes the first cross product in the first term on the right side of (2.23) to vanish. The last cross products of the two terms on the right side may be neglected, because they are of second-order in small quantities, compared to the static field components [35]. Since the Gilbert damping parameter is small [36], the squared α is also dropped. Considering a circular polarized driving RF field [22],

$$\mathbf{h}_1 = \mathbf{h}_{\pm} e^{-i\omega t} = h_0(\mathbf{e}_1 \pm \mathbf{e}_2) e^{i\mathbf{kr} - i\omega t}, \tag{2.24}$$

with the amplitude h_0, the polarization vectors $\mathbf{e}_1$ and $\mathbf{e}_2$, the wave vector $\mathbf{k}$ and the position vector $\mathbf{r}$. The $\pm$ denotes left or right circular polarization, respectively. It is assumed that the dynamic part of the magnetization follows the excitation field $\mathbf{h}_1$, having the same time dependency:

$$\mathbf{m} = \mathbf{m}_{\pm} e^{-i\omega t} = m_0(\mathbf{e}_1 \pm \mathbf{e}_2) e^{i\mathbf{kr} - i\omega t}, \tag{2.25}$$

with the amplitude m_0. The expressions (2.24) and (2.25) are inserted into (2.23) and after rearranging:

$$\underbrace{\begin{pmatrix} h_{\mathrm{y}}(t) \\ h_{\mathrm{z}}(t) \end{pmatrix}}_{\mathbf{h}_1} = \underbrace{\frac{1}{\omega_{\mathrm{M}}} \begin{pmatrix} -\omega_{\mathrm{H}} + i\alpha\omega & i\omega \\ -i\omega & -\omega_{\mathrm{H}} + i\alpha\omega \end{pmatrix}}_{\hat{\chi}^{-1}} \underbrace{\begin{pmatrix} m_{\mathrm{y}}(t) \\ m_{\mathrm{z}}(t) \end{pmatrix}}_{\mathbf{m}}, \tag{2.26}$$

with $\omega_{\mathrm{M}} = \gamma\mu_0 M_{\mathrm{S}}$ and $\omega_{\mathrm{H}} = \gamma\mu_0 H_0$.
The problem has the form:

$$\text{“}\mathbf{h}_1 = \hat{\chi}^{-1}\mathbf{m}\text{”}. \tag{2.27}$$

Multiplying (2.27) from left with the inverse of $(\hat{\chi}^{-1})^{-1} = \hat{\chi}$, one obtains the linear response function,

$$\mathbf{m} = \hat{\chi}\mathbf{h}_1, \tag{2.28}$$

and identifying $\hat{\chi}^{-1}$ as the inverse of the Polder susceptibility tensor $\hat{\chi}$ [35].

$$\hat{\chi} = \frac{\omega_{\mathrm{M}}}{\Delta} \begin{pmatrix} -\omega_{\mathrm{H}} + i\alpha\omega & -i\omega \\ i\omega & -\omega_{\mathrm{H}} + i\alpha\omega \end{pmatrix}, \tag{2.29}$$

$$\text{with} \quad \Delta \;=\; \mathrm{Det}(\hat{\chi}^{-1}) = (\omega_{\mathrm{H}} - i\alpha\omega)^2 - \omega^2$$

To gain an expression for the scalar susceptibility from the Polder tensor, the linear response function (2.28) is considered an eigenvalue problem [35]:

$$\begin{aligned} \mathbf{m} &= \hat{\chi}\mathbf{h}_1 \\ &= \hat{\chi}h_1\mathbf{C} \\ &= \Lambda h_1\mathbf{C} \\ \mathbf{m} &= \chi h_1\mathbf{C} = \chi\mathbf{h}_1, \end{aligned} \tag{2.30}$$

with the eigenvector $\mathbf{C}$ and the eigenvalue Λ, representing the scalar susceptibility χ. Solving the eigenvalue problem (2.30), yields a complex expression of χ, which depends on the angular frequency ω, while the magnetic field strength H_0 is held constant. Separating the complex function in its real and imaginary parts yields:

$$\mathrm{Re}[\chi] = \chi'(\omega) = \omega_\mathrm{M} \frac{\omega_\mathrm{H} - \omega}{(\omega_\mathrm{H} - \omega)^2 + \alpha^2\omega^2}, \tag{2.31}$$

$$\mathrm{Im}[\chi] = \chi''(\omega) = \omega_\mathrm{M} \frac{\alpha\omega}{(\omega_\mathrm{H} - \omega)^2 + \alpha^2\omega^2}. \tag{2.32}$$

The real part describes the dispersion and imaginary part the absorption of FMR. It shall be noted, that for an absorption experiment the resonance will not result in a peak, but in a resonance dip. Therefore χ'' needs to be $(1 - \chi'')$ to describe the experiment correctly.
With Eqn. 2.20 a relation between the line width $\Delta\omega$ and the Gilbert damping parameter α can be established, given that there is a explicit dispersion relation $\omega_\mathrm{res}(H_0)$ (cf. Sec. 2.4). Expressing $\omega_\mathrm{res}(H_0)$ explicitly as a function of H_0 results in:

$$\mathrm{Re}[\chi] = \chi'(H_0) = \mu_0 M_\mathrm{S} \frac{\mu_0 H_0 - \frac{\omega}{\gamma}}{(\mu_0 H_0 - \frac{\omega}{\gamma})^2 + (\mu_0 \frac{\Delta H}{2})^2} = \mu_0 M_\mathrm{S} \frac{B_0 - B_\mathrm{res}}{(B_\mathrm{res} - B_0)^2 + (\frac{\Delta B}{2})^2}, \tag{2.33}$$

$$\mathrm{Im}[\chi] = \chi''(H_0) = \mu_0 M_\mathrm{S} \frac{\mu_0 \frac{\Delta H}{2}}{(\frac{\omega}{\gamma} - \mu_0 H_0)^2 + (\mu_0 \frac{\Delta H}{2})^2} = \mu_0 M_\mathrm{S} \frac{\frac{\Delta B}{2}}{(B_\mathrm{res} - B_0)^2 + (\frac{\Delta B}{2})^2}. \tag{2.34}$$

These two equations are plotted in Fig. 2.6, using a saturation magnetization $\mu_0 M_\mathrm{S}$ of 1 T, a resonance field B_res of 250 mT and a line width ΔB of 25 mT.

2.6. Superconducting Microwave Resonator

A resonator circuit is characterized by its frequency dependent impedance Z, consisting of the resistance R, the capacitance C and the inductance L of the circuit. For a superconducting resonator the resistance is zero. The resonators used in the experiments in Chapter 6 are half-wave transmission resonators. They consist of a transmission line with the length of a half wave of frequency ω_0, the resonance frequency. Capacitors with capacitance C define the coupling to the feed line. The transmission line has the impedance Z_line. A schematic of a half-wave resonator is shown in Fig. 2.7.
When the resonator is in resonance signals may pass it, which results in a transmission peak. The resonance frequency for a superconducting resonator is approximately given

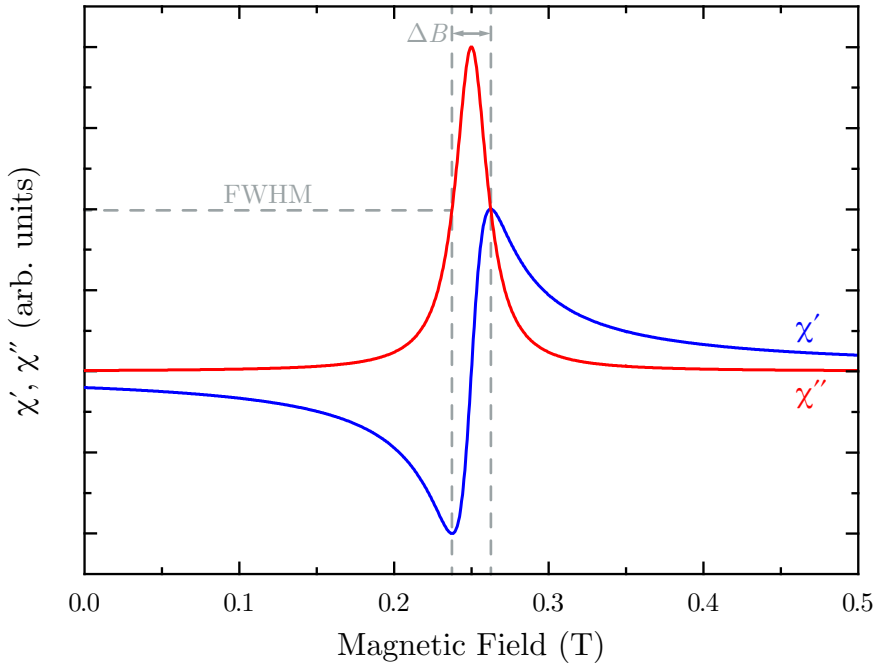

Figure 2.6.: Plotted dispersion χ' and absorption χ'' with Eqn. 2.33 and 2.34, respectively.

by:

$$\omega_0 \approx \frac{1}{\sqrt{LC}}. \tag{2.35}$$

The capacitance C is determined by the two coupling capacitors and the induction L can be estimated by the impedance Z_{line}. The impedance of a superconductor is defined as:

$$Z_{\text{line}} = R_{\text{line}} + i\omega L_{\text{line}}, \tag{2.36}$$

with the inductance of the superconducting transmission line L_{line} and the resistance R_{line}. The resistance is caused by a small fraction of electrons, which are not in the superconducting state. For temperatures T much lower than the critical temperature

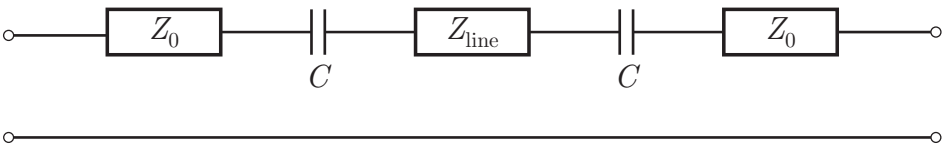

Figure 2.7.: Lumped element circuit diagram of a half wave transmission resonator. The resonator, with impedance Z_{line}, is coupled by two capacitors to the circuitry with a characteristic impedance Z_0.

T_c of the superconductor, $R_{\text{line}} \ll \omega L_{\text{line}}$, therefore $Z_{\text{line}} \approx i\omega L_{\text{line}}$ [37]. The impedance of a Type-II superconductor is given by:

$$Z_{\text{line}} = \sqrt{\frac{i\omega\mu_0}{\sigma}}. \tag{2.37}$$

σ is the complex conductivity of a superconductor and can be calculated from the Mattis-Bardeen equations [38].
Another important parameter describing a resonator is the quality factor Q (Q-factor). It is a dimensionless quantity indicating how effectively a resonator can store energy. The higher the quality factor, the longer is the lifetime of a photon inside the resonator. For a half wave resonator at n-th resonance frequency ω_n [37],

$$Q = \frac{n\pi}{4Z_0 Z_{\text{line}}(\omega_n C)^2}. \tag{2.38}$$

The Q-factor also connects the resonance frequency ω_0 with the FWHM line width $\Delta\omega$ of the transmission peak [37].

$$Q = \frac{\omega_0}{\Delta\omega}. \tag{2.39}$$

The finale parameters of a superconducting microwave resonator are given by its geometry. The resonators used in this thesis are described in Sec. 3.4.2.

Haaaaaave you met ...

Barney Stinson

Chapter 3.

Experimental Methods

Most experiments performed during this thesis were conducted at low temperatures (4 K $\geq T \geq$ 50 mK). The two different types of cryostats used to reach these temperatures will be described in this section. Furthermore, the microwave components, used in the ferromagnetic experiments, will be discussed, like the vector network analyzer (VNA) or microwave guiding geometries, such as coplanar waveguides (CPW) or microwave resonators. Finally this section will deal with the microwave coaxial cables used in the different measurement setups.

3.1. Dilution Refrigerator

Dilution refrigerators are a type of cryostat allowing to generate temperatures in the millikelvin range, with a minimum temperature of about 1.5 mK [4].

3.1.1. Physical Principle

The operation of dilution refrigerators cryostats is based on a mixture of the two stable helium isotopes, helium-3 (^{3}He) and helium-4 (^{4}He). These isotopes differ not only in their masses, but also in their spin character. ^{3}He is a fermion with a spin of $S_{^3\mathrm{He}} = 1/2$, while ^{4}He is a boson with a spin of $S_{^4\mathrm{He}} = 0$. Therefore, they obey completely different statistics. A mixture of these two isotopes exhibits additional phases at low temperatures, in addition to the phases they would have on their own. Figure 3.1 shows the phase diagram of a liquid ^{3}He/^{4}He mixture in dependence on the ^{3}He concentration x_3.
The phase diagram shows three different regions. Above 2.17 K the two liquids exist in their normal fluid state. Along the so-called lambda line the temperature reduces with

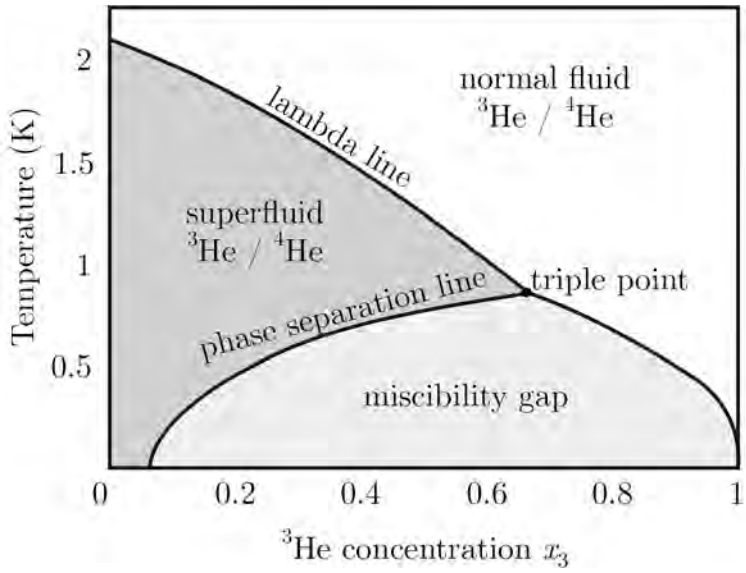

Figure 3.1.: $T - x_3$-phase diagram of a liquid mixture of ^{3}He/^{4}He. Three different phases, separated by lines of equilibrium which meet at the triple point, are indicated by gray shading. The light gray area is the miscibility gap where the two different helium isotopes are separated [39].

increasing ^{3}He concentration x_3 . Below the lambda line the ^{4}He part of the mixture becomes superfluid. At 0.87 K and a ^{3}He concentration of 67 % [40] a third phase emerges and extends with a dome shape down to 0 K. This phase is the miscibility gap where the two liquids separate and form two phases, a ^{3}He rich and a ^{4}He rich one. However, the phase separation is not complete. There is still a portion of ^{3}He diluted in ^{4}He even down to 0 K. The reason for this lies in the different binding energies of the two atoms with one another and with each other [4]. The binding energy of a single ^{3}He atom in pure ^{3}He is given by $\varepsilon_{3,\mathrm{c}} = \mu_{3,\mathrm{c}}/N_\mathrm{A}$ [4], where $\mu_{3,\mathrm{c}}$ and N_A are the chemical potential of pure liquid ^{3}He and the Avogadro constant, respectively. The other binding energy of interest is the one of a single ^{3}He atom in pure ^{4}He, given by $\varepsilon_{3,\mathrm{d}(x_3\to 0)} = \mu_{3,\mathrm{d}(x_3\to 0)}/N_\mathrm{A}$, with $\mu_{3,\mathrm{d}}$ as the chemical potential of pure liquid ^{4}He. Because of the smaller mass of ^{3}He, it exhibits greater zero point fluctuations and thus takes up a greater volume than ^{4}He, such that one finds, $|\varepsilon_{3,\mathrm{d}(x_3\to 0)}| > |\varepsilon_{3,\mathrm{c}}|$. In a simple picture, a single ^{3}He atom can be bonded with much more ^{4}He atoms than with atoms of its own kind, resulting in a greater binding energy of ^{3}He in ^{4}He. However, due to the fact that ^{3}He is a fermion, it has to obey the Pauli principle and therefore each additional ^{3}He atom has to occupy a different energy state. Thus the

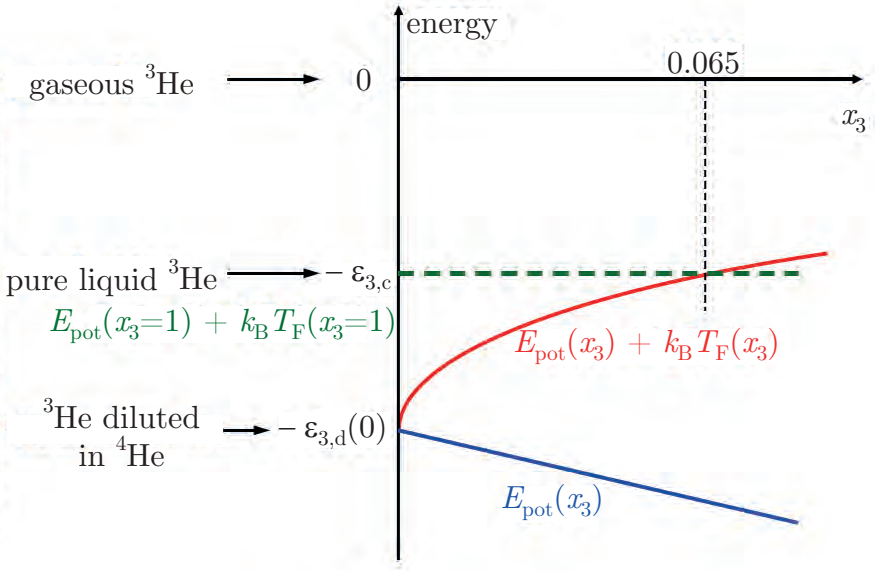

Figure 3.2.: Binding energy of liquid ^{3}He diluted in ^{4}He (blue line), binding energy of liquid ^{3}He diluted in ^{4}He plus the Fermi energy of ^{3}He in ^{4}He (red line) and the total energy of pure liquid ^{3}He (dashed green line). All energies are plotted relative to the total energy of gaseous ^{3}He [4].

gain in binding energy is exceeded by the Fermi energy at some concentration x_3, as shown in Fig. 3.2.

The diluted ^{3}He forms a degenerate Fermi liquid with a superfluid ^{4}He background [41], [42]. Although the Fermi energy of the diluted ^{3}He is reduced, because of the greater effective mass in the solvent, it is increasing with the concentration x_3 as $k_{\mathrm{B}}T_{\mathrm{F}} \propto x_3^{\frac{2}{3}}$ [4]. At a concentration $x_3 = 6.5$ % the energies of the pure and diluted liquids are equal and from there on with increasing x_3 it is more favorable for the ^{3}He to form a pure liquid separated from the ^{4}He. But a concentration of 6.5 % still remains diluted in the ^{4}He. With this phase separation, cooling can now be achieved when a ^{3}He atom crosses the boundary from the concentrated to the diluted phase of ^{3}He. But there is only a reduction in temperature if the heat capacities C_{V} of the two phases are different, and if the concentrated ^{3}He phase has a greater heat capacity than the diluted phase [43]. This difference becomes clear when one looks at the internal energies U which correspond to the binding energies shown in Fig. 3.2. Internal energy and heat capacity are connected by the thermodynamic relation $\frac{\Delta U}{\Delta T} = C_{\mathrm{V}}$ [44]. Figure 3.3 compares the two internal energies in dependency of temperature T. At their transition the free energies F of the two phases must be

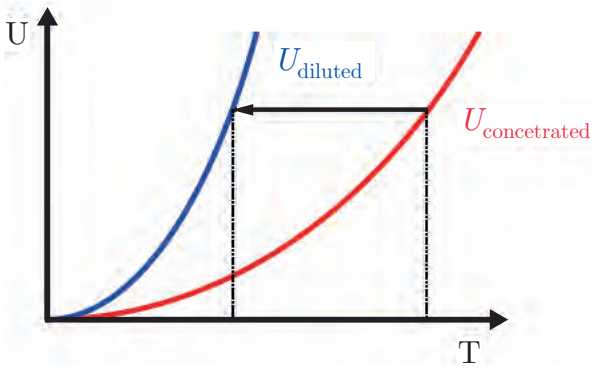

Figure 3.3.: Internal energies U of ^{3}He diluted in ^{4}He (blue line) and concentrated ^{3}He (red line) with respect to temperature T [4].

equal. So the condition $F_{\text{diluted}} \approx U_{\text{diluted}} = U_{\text{concentrated}} \approx F_{\text{concentrated}}$ must be fulfilled [4]. Therefore an atom that crosses the boundary from the concentrated to the diluted phase has to absorb heat and this goes along with an reduction in temperature at the phase boundary.

The phase separation of ^{3}He/^{4}He has a simple analogue in classical thermodynamics, namely the phase separation of a fluid and a gas [43]. In this case the concentrated ^{3}He phase is the fluid (quasi-liquid) and the diluted ^{3}He phase is the gas (quasi-gas) with the difference that the quasi-fluid is located above the quasi-gas, because the liquid ^{4}He is heavier than the liquid ^{3}He. The quasi-gas behaves approximately like an ideal gas. Its pressure at a certain concentration x_3 can be described via the osmotic pressure P_{osm} with the van't Hoff equation $P_{\text{osm}}V = x_3RT$ [43], V is the gas volume and R is the ideal gas constant. The osmotic pressure is analogous to the vapor pressure over a liquid. Therefore the cooling in a dilution refrigerator can be seen as cooling through evaporation. If the osmotic pressure is reduced in the quasi-gas there will be a "evaporation" of ^{3}He from the quasi-liquid into the quasi-gas, as illustrated in Fig. 3.4 [4].

3.1.2. Operation Principle of a Dilution Refrigerator

In Fig. 3.5 a schematic overview of a dilution refrigerator can be seen. Inside the mixing chamber (MC) the phase separation of the helium mixture takes place. For the transition of ^{3}He from the quasi-liquid into the quasi-gas the osmotic pressure needs to be reduced. This is done in the so-called still, which is connected with the quasi-gas phase inside the MC. Here ^{3}He is evaporated from the liquid ^{4}He. During

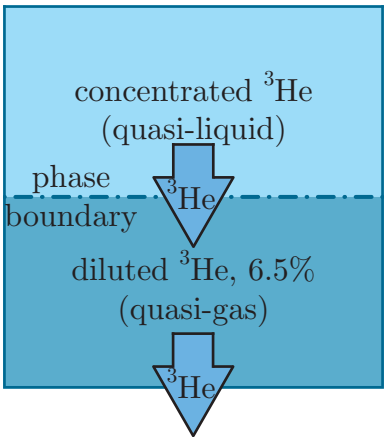

Figure 3.4.: Diagram of concentrated and diluted ^{3}He phases and the flow of ^{3}He if it is removed from the diluted phase [4].

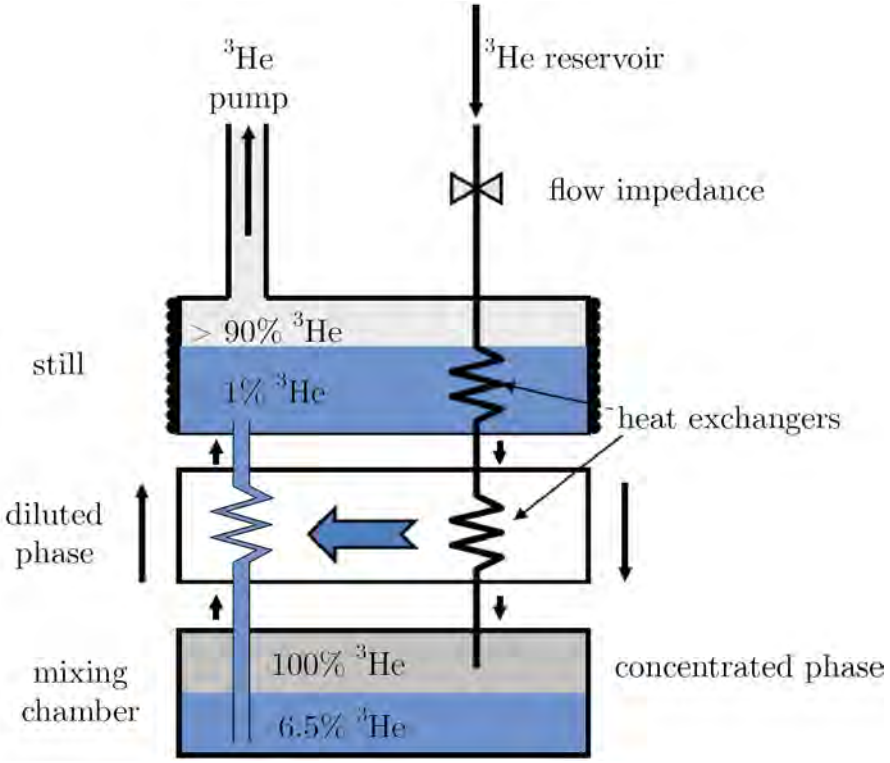

Figure 3.5.: Schematic of a dilution refrigerator, showing the mixing chamber (MC) with the phase separated ^{3}He/^{4}He mixture and the still. The flow direction is from the ^{3}He reservoir into the MC from there into the still and in a cycle via a pump back into the MC. The heat exchanger on the way down to the MC precools the mixture [4].

this process the concentration of ^{3}He in the liquid phase $x_{3\ \mathrm{still}}$ is smaller than the concentration of ^{3}He in the diluted phase inside the MC, $x_{3\ \mathrm{MC}} = 6.5\ \%$. This has to be seen in relation to the still temperature T_{still} and the MC temperature T_{MC}. On this way it is possible that the concentration $x_{3\ \mathrm{still}}$ is smaller than 6.5 %. While the concentration $x_{3\ \mathrm{still}}$ is very small in the liquid phase the concentration of ^{3}He in the gas phase is over 90 %, meaning mostly ^{3}He is evaporated inside the still. Thereby, an osmotic pressure gradient between the MC and the still is created [43]. With the connection of a vacuum pump to the still the evaporated gas can be pumped down and cyclic brought back into the MC over a condenser. With this a continuous cooling can be achieved down to a minimum temperature of around 1.5 mK [4].

3.2. Magnet Flow Cryostat

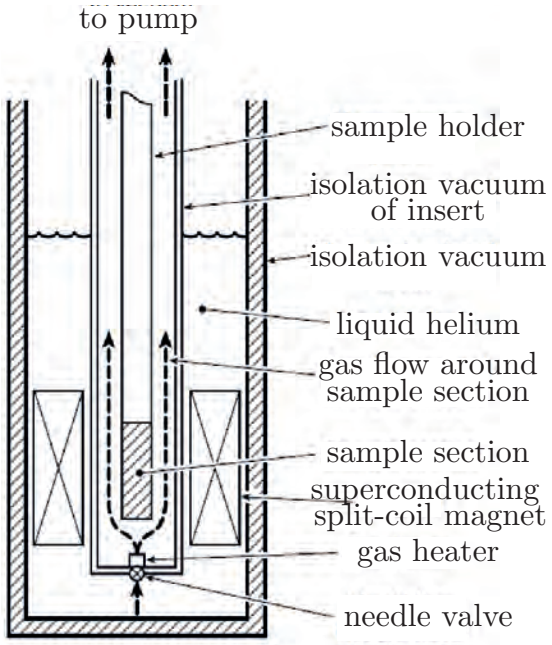

Figure 3.6.: Schematic of a magnet flow cryostat. Inside the ^{4}He bath, a superconducting magnet allows to generate a static magnetic field at the sample location [45].

This type of cryostat uses a cold gas flow of helium-4 for cooling, with the ^{4}He originating from a liquid ^{4}He bath. A schematic overview is shown in Fig. 3.6 [45]. From a liquid ^{4}He bath, which also acts as a thermal isolation shield, the ^{4}He is transported through a capillary into the variable temperature insert (VTI). The exit

of the capillary is located at the bottom of the VTI, and the sample resides just above of it. A vacuum pump is connected with the top of the VTI. The pump draws the ^{4}He from the bath via a capillary into and up the VTI. On the way up, the sample is cooled by the passing gas flow. The flow of ^{4}He is controlled by a needle valve located at the beginning of the capillary inside the ^{4}He bath, such that the cooling rate can be adjusted. At the exit of the capillary a heater is mounted to warm up the passing ^{4}He. The samples temperature can be adjusted in a temperature range, spanning from more than 300 K continuously down to a minimum of around 1.3 K. Temperatures below 4.2 K are achieved by the pumping. It reduces the vapor pressure $p(T)$ of the liquid ^{4}He bath, which is given by [40]

$$p(T) = p_0 \mathrm{e}^{-\frac{\Delta H_{\mathrm{vap}}}{RT}}, \tag{3.1}$$

with the atmospheric pressure p_0 and the latent heat ΔH_{vap} of evaporation. Reducing the vapor pressure leads to a reduction in temperature. The minimum temperature is limited by the pumping speed and thermal losses to the outside of cryostat [40]. This cryostat type features also a pair of superconducting Helmholtz coils, residing in the liquid ^{4}He bath. They can provide a homogeneous magnetic field at the samples location.

3.3. Vector Network Analyzer

All ferromagnetic resonance measurements, in the course of this thesis, were conducted with a vector network analyzer (VNA). It features a microwave source, combined with a microwave detector.

3.3.1. Operation Principle

Figure 3.7 shows a block diagram of the important elements of a two port VNA. The center piece is a broadband microwave source (signal generator) which produces a wave V_{inc} at a frequency f. Depending on the positions of the switches S1 and S2 the wave travels in the direction of port 1 or 2 or even in both directions at the same time. Either way both paths are built up symmetrically. The choice of switch position determines what will be measured, this will be discussed in more detail in Sec. 3.3.2. In the case of Fig. 3.7 the switch S1 is closed so that the wave travels over a bias

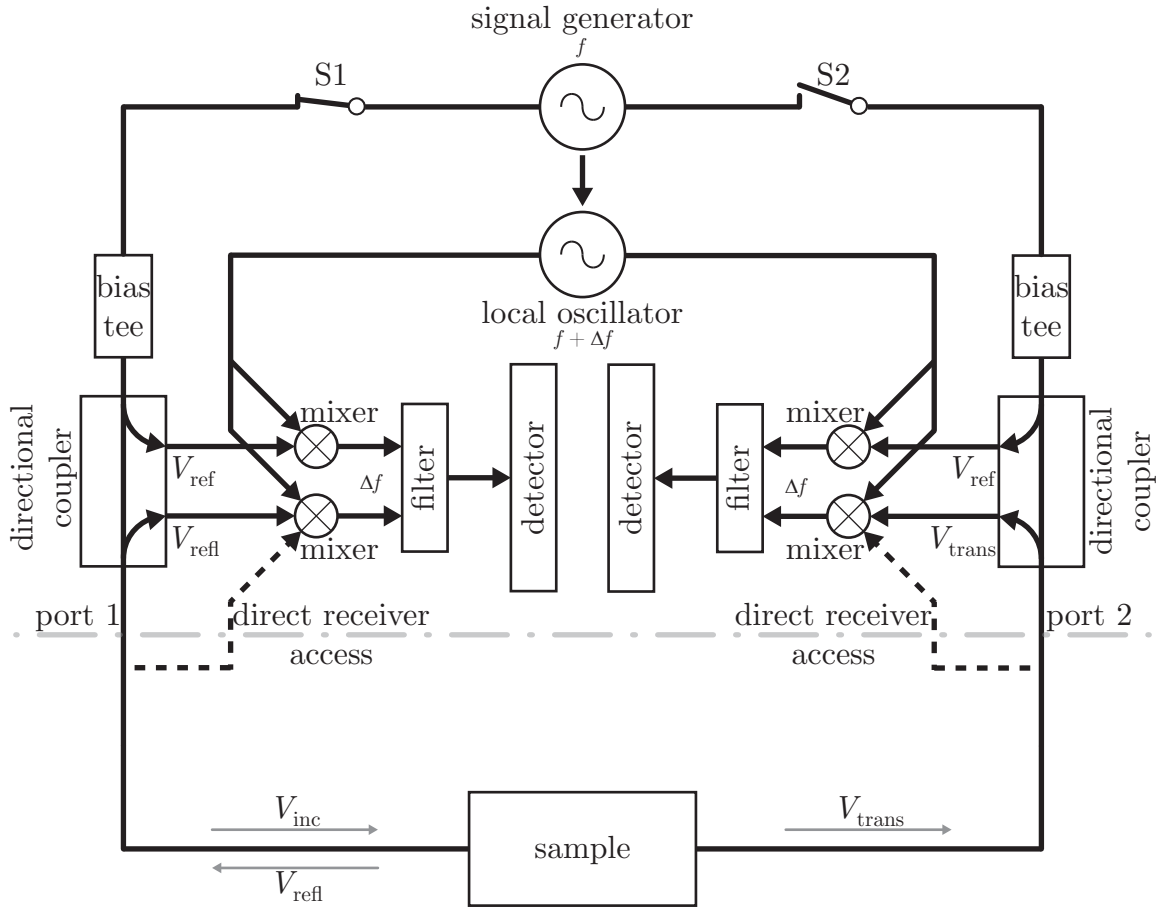

Figure 3.7.: Block diagram of a two port VNA

tee and a directional coupler out of port 1. With the bias tee the RF voltage signal can be superimposed with a DC voltage offset. This is required for some active RF elements to adjust their working point, but was not necessary during the course of the thesis. A directional coupler splits up the incoming wave depending on its propagation direction. It splits up the signal V_{inc} to provide a reference V_{ref} and couples ideally not in the other side arm which is reserved for waves traveling in the opposite direction. A directional coupler is not an ideal device and thus there is always a power loss upon passing the coupler. After the bias tee and the directional coupler the wave V_{inc} exits port 1 and reaches the sample via coaxial cables. Here, a portion of the wave is absorbed, another reflected (V_{ref}) or transmitted (V_{trans}). V_{ref} propagates back to port 1 and V_{trans} to port 2. The voltage and power measurement, of electromagnetic waves in the gigahertz range, is rather difficult and imprecise [33], [46]. By using

heterodyne mixing the incoming signals are down-converted from the gigahertz range into the megahertz range, where the signal detection is more straightforward. The incoming wave is mixed with a wave generated by a local oscillator, which is coupled to the signal generator. The frequency of the second wave is detuned by a frequency Δf relative to the frequency f. The mixing results in a wave with equivalent voltage amplitude and phase, but only with a frequency of Δf. Before detection, the down-converted wave passes a filter, optimized for the frequency range of Δf, suppressing all other contributions with different frequency. With this a high measurement dynamic range is achieved, allowing to detect signals with high precession.
Some experiments, conducted in this thesis, are performed with ultra low microwave powers, where signals in the picowatt regime need to be detected (Cha. 4). These power levels are at the edge of the VNAs measurement dynamic range. The VNA features an alternative input port to further increase the dynamic range, the direct receiver access. This port is directly connected to the measurement electronic, by-passing the directional coupler. Thus, the dynamic range is further increased, such making it possible to detected even ultra low power signals. Accessing the measurement electronics directly, imposes a risk of damage to the electronics, if too much microwave power or DC signals are applied. Therefore, the direct receiver access is only used for low microwave power measurements[33], [47], [46].

3.3.2. Scattering Parameters

This section discusses the parameters measured by the VNA Usually electrical circuits are described in terms of voltages, currents and impedances or admittances. For high frequency networks, i.e. any kind of electrical circuit with a number of input/output ports, this conventional approach often is clumsy. One therefore rather uses scattering parameters (S-parameters). These, in general complex valued, parameters are a direct way to measure incident, reflected and transmitted waves [48]. Written in matrix notation the S-parameters form a quadratic scattering matrix, which provides a complete description of a network. The number of ports gives the dimensionality of the scattering matrix. The possible S-parameters of a two port network are shown in Fig. 3.8 [33].

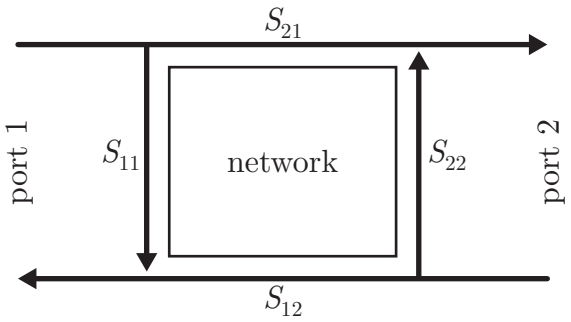

Figure 3.8.: Block diagram illustrating the possible scattering parameters for a two port network.

The specific scattering matrix for this network is defined as

$$\hat{S} = \begin{pmatrix} S_{11} & S_{12} \\ S_{21} & S_{22} \end{pmatrix}.$$

In particular the elements of $\hat{S}$ are given by

$$S_{ij} = \left.\frac{V_i}{V_j}\right|_{V_k=0;\ k\neq j} \quad ;\ i,\ j,\ k\ =\ 1,2.$$

This is read as follows: S_{ij} is obtained by driving port j with an incident wave of voltage V_j and measuring the voltage V_i the incoming wave at port i, whilst all ports apart from the j-th are terminated in matched loads. Therefore, S_{ii} represents the reflection from the networks i-th port while simultaneously driving port i, and S_{ij} denotes the transmission from the driven port j to port i [48].
During the experiments conducted in this thesis, the transmission S_{21} had been measured. The VNA detects these voltages, in addition to their phases, relative to the incident or reference voltage V_{ref} as $S_{21} = {}^{V_{\text{trans}}}/_{V_{\text{ref}}}$ [33]. A typically FMR spectrum at a defined VNA frequency is shown in Fig. 3.9. The simultaneously measured real and imaginary parts of S_{21} are plotted against the static magnetic field $\mu_0\mathbf{H}_0$ at a VNA frequency $f = 18$ GHz. This particular measurement shows FMR at a 50 nm thick cobalt film and a temperature of 50 mK. The data had been phase corrected and a linear background was subtracted. For detailed information about data processing and the measurements with this cobalt thin film, cf. Chapter 4.

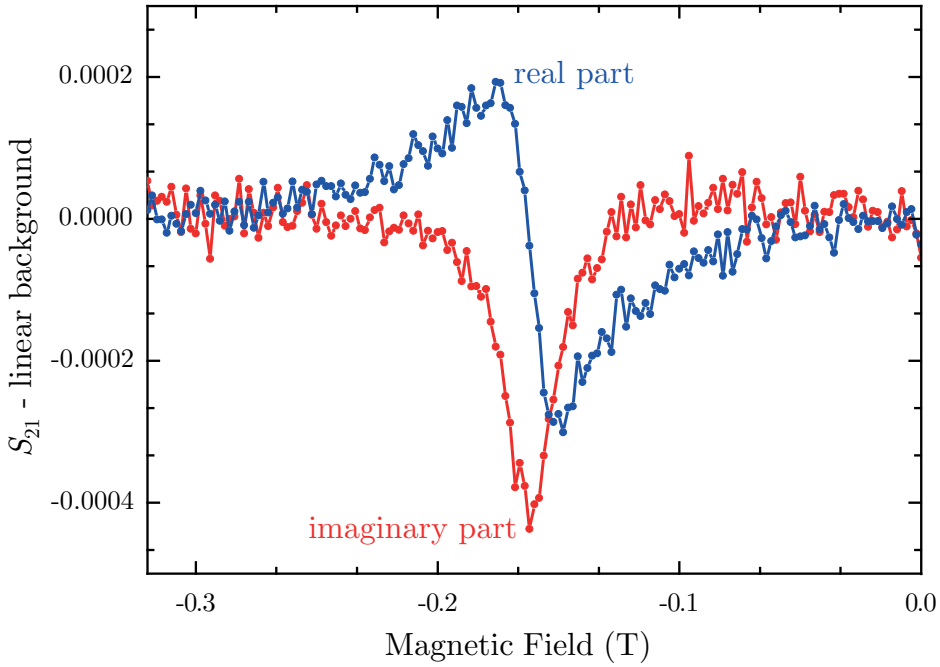

Figure 3.9.: Real and imaginary part of S_{21} in dependency of the static magnetic field at 18 GHz. The spectrum shows a ferromagnetic resonance of a 50 nm thick cobalt film at 50 mK (cf. Cha. 4).

3.3.3. Relating S-Parameters and Susceptibility

For the excitation of FMR, microwave power is absorbed. The FMR signal is measured by the transmission S_{21}. Therefore, S_{21} has to represent the magnetic answer of the excited magnetic system. If Fig. 3.9 is compared with the theoretical curves of the real and imaginary parts of the magnetic susceptibility, cf. Fig. 2.6, one sees that their trends are comparable. That the absorbed microwave power and the susceptibility are indeed proportional is now demonstrated.
Based on Poynting's theorem for electromagnetic fields with a harmonic time dependency, given by [22]

$$-\frac{1}{2}\oint_S (\mathbf{e}_1 \times \mathbf{h}_1^*) d\mathbf{S} = \frac{1}{2}\int_V (i\omega \mathbf{b}_1 \cdot \mathbf{h}_1^* + i\omega \mathbf{e}_1 \cdot \mathbf{d}_1^* + \mathbf{e}_1 \cdot \mathbf{j}^*) dV. \tag{3.2}$$

Here, $\mathbf{e}_1$ and $\mathbf{h}_1$ are the electric and the magnetic field components of the microwave with angular frequency ω, $\mathbf{d}_1$, $\mathbf{b}_1$ are its electric displacement field and its magnetic flux density and $\mathbf{j}$ is the current density. The $*$ denotes the conjugated form. The integration is performed over the volume V, containing a ferromagnetic sample, and

is enclosed by the surface S. The surface integral on the left side of (3.2) is performed over the Poynting vector, representing the energy flow of the system in consideration [22]. When there is no dissipation, the net energy flow out and into the system is zero. During FMR, power is absorbed by the ferromagnetic sample, resulting in a non zero energy flow. The power absorption can be interpreted by the real part of the right hand side of (3.2) [49]. Furthermore, if only the sample volume V_S is taken in consideration for the integral, the absorbed power by the ferromagnetic sample is

$$\begin{aligned} P_\mathrm{abs} &= \frac{1}{2}\mathrm{Re}\left[\int_{V_\mathrm{S}} i\omega \mathbf{b}_1 \cdot \mathbf{h}_1^*\right] \\ &= \frac{1}{2}\mathrm{Re}\left[\int_{V_\mathrm{S}} i\omega \hat{\mu}\mathbf{h}_1 \cdot \mathbf{h}_1^*\right] \\ &= \frac{1}{2}\mathrm{Re}\left[\int_{V_\mathrm{S}} i\omega \mu_0(\hat{\mathbf{I}} + \hat{\chi})\mathbf{h}_1 \cdot \mathbf{h}_1^*\right], \end{aligned} \tag{3.3}$$

where $\hat{\mu}$ is the Polder permeability tensor and $\hat{\chi}$ is the Polder susceptibility tensor. The eigenvalues of $\hat{\chi}$ yield the real- and imaginary-part of the scalar magnetic susceptibility (cf. Sec. 2.5). Since the transmission S_{21} is direct proportional to the absorbed microwave power, the measured VNA FMR signal corresponds to the magnetic susceptibility of the system under investigation.

3.4. Sample Box and Sample Holder

Excitation of FMR requires an alternating magnetic field $\mathbf{h}_1$ to drive magnetization dynamics. To provide the field $\mathbf{h}_1$ at the samples location, the microwave needs to be appropriately guided. This can be achieved using a coplanar waveguide (CPW) or microwave resonator which act as a sample holder and in addition provide the appropriate alternating magnetic field profile.

3.4.1. Coplanar Waveguide

A CPW is basically a coaxial cable with its conductors projected on a two dimensional plane (cf. Fig. 3.10). The whole CPW structure is patterned onto an insulating substrate. Between two conducting ground planes runs the center conductor, separated from the ground planes by two gaps. The CPWs used in this thesis are fabricated on a high resistivity silicon substrate ($\rho > 3000\ \Omega$cm) with a thickness of $t_\mathrm{S} = 525\ \mu$m.

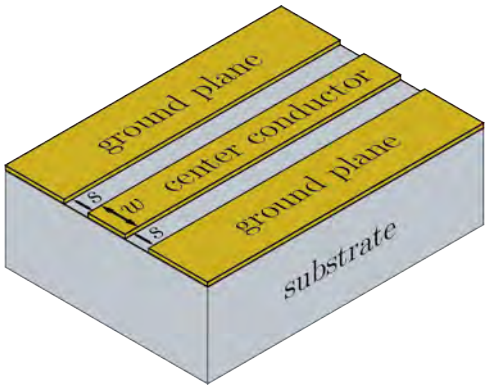

Figure 3.10.: Drawing of a CPW with its ground planes on either side of the center conductor separated by a gap fabricated on an insulating substrate.

The CPW pattern is transferred onto the substrate using optical lithography and lift off. The center conductor and the ground planes consist of a 7 nm thick chromium adhesion layer, a $t = 100$ nm or $t = 150$ nm thick layer of gold, deposited via sputtering. The difference between the 100 and 150 nm thick gold layer is only an increase in robustness of the gold layer. The total dimension of the CPWs are 6×10 mm^2 with the center conductor running parallel to the long side.
Since the CPW is part of the microwave transmission line it needs to be impedance matched to the rest of the line. Otherwise the microwave reflection will increase at the interface of the coaxial cable and the CPW. The characteristic impedance Z_0 of the coaxial cables is 50 Ω, and the CPW should have the same impedance. It is given by [33]

$$Z_0 = \frac{1}{2c\sqrt{\varepsilon_{\mathrm{r,eff}}}C_{\mathrm{air}}} = \frac{22.97\pi}{\sqrt{\varepsilon_{\mathrm{r,eff}}}}\frac{K'}{K}.$$

Here c is the speed of light, $\varepsilon_{\mathrm{r,eff}}$ is the effective dielectric constant for a dielectric/air interface, C_{air} is the capacitance of air and K and K' are the complete elliptic integrals of the first kind, and its complement, respectively [22]. These integrals are functions of the ratio $w/(w+2s)$, where w is the width of the center conductor and s the width of the gap. Thus, for an impedance matched CPW, the ratio $w/(w+2s)$ has to be chosen appropriately. The widths can be varied as long as the ratio is not changed [33]. The CPWs used in this thesis have a center conductor width $w = 20$ μm and a gap width $s = 12$ μm.
The alternating magnetic field $\mathbf{h}_1$ in a CPW geometry will be distributed as seen in

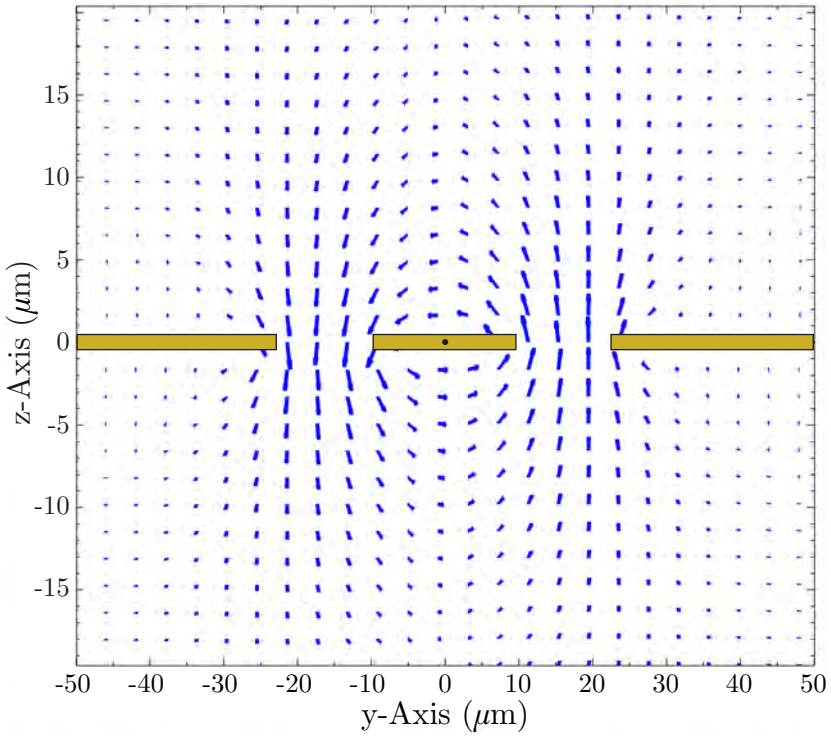

Figure 3.11.: Cross section of a CPW with the magnetic field $\mathbf{h}_1$ distribution for a current flow in x-direction. The field profile was calculated for a microwave with a frequency $f = 10$ GHz, having a voltage amplitude of 1 V [50].

Fig. 3.11 [50]. The maximum strength of the field $h_{1,\max}$ above the center conductor can be calculated with Maxwell's equation [33].

$$I = \oint_A \mathbf{j} \cdot \mathrm{d}\mathbf{A} = \oint_{C_A} \nabla \times \mathbf{j} \cdot \mathrm{d}\mathbf{l} = \oint_{C_A} \mathbf{h}_1 \mathbf{j} \cdot \mathrm{d}\mathbf{l} = 2wh_{1,\max} + \mathcal{O}(t),$$

with the current density $\mathbf{j}$ and the area A enclosed by the path C_A. If the width of the center conductor is much greater than its thickness, $t/w \ll 1$, the path integral approximately yields only $2wh_{1,\max}$ as a result [33]. With the thin film CPWs used here, this approximation holds and as an example one gets a maximum magnetic field of $\mu_0 h_{1,\max} = 4.44$ μT for an incident microwave power of 1 μW.

3.4.2. Superconducting Coplanar Microwave Resonator

Microwave resonators open up another interesting way of performing FMR experiments, cf. Chapter 6. Not only do they provide the alternating magnetic field $\mathbf{h}_1$, they also procure a defined photon cavity with a high quality factor Q. With a microwave

resonator an interaction between photons and spin waves, excited by ferromagnetic resonance, can be established.

In the course of this thesis, superconducting microwave resonators made from niobium (Nb) were used. Nb is an elemental superconductor and has the highest critical temperature of them, $T_C = 9.25$ K. Furthermore, it is also a type-II superconductor [51]. The Nb resonators were fabricated on identical substrates as the CPW structures, a $6 \times 10 \times 0.525$ mm^3 high resistivity silicon substrate. At first a layer of Nb was sputtered on the substrate, with a layer thicknesses of either 100 nm, 200 nm or 300 nm. On top of the Nb, a photo resist layer was then applied and patterned onto the resonator structure, using optical lithography. With reactive ion etching (RIE), the Nb not covered by photo resist was removed. Finally the Nb was stripped from the photo resist and the resonator was finished. The resonator design used in this thesis are depicted in Fig. 3.12. A characterization of the resonators with varying thicknesses, is given in Sec. 6.1.

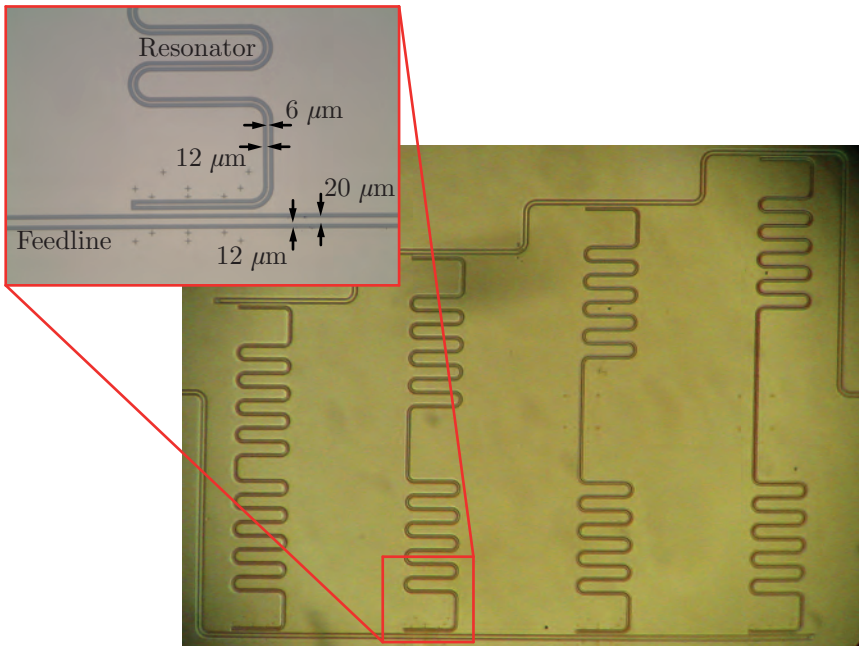

Figure 3.12.: Picture of a Nb microwave resonator. The marked area zooms in on one of the resonators coupling capacity. The dimensions are given in the picture.

3.4.3. Sample Box

To connect coaxial cables to a CPW or microwave resonator structure, they are mounted into a sample box, fabricated for these kinds of structures (cf. Fig. 3.13). The box is made of oxygen-free high thermal conductivity (OFHC) copper [52] and

Figure 3.13.: Sample box with gold CPW, connected via flange mounted SMA female connectors with stripline. For measurements, the box is covered with a top cover.

is in addition plated with gold to prevent oxidization. The RF chips reside in a deepening matched to its dimension. On the short ends of the box, flange mount female SubMiniature version A (SMA) connectors are attached [53]. The outer conductor of the SMA connector is connected with the box and the inner conductor ends as a stripline in the inside of the box. The stripline is connected to the center conductor of the sample holder with silver glue. The ground planes and the sample box are connected the same way.

3.5. Microwave Cabling

A rather important, but rarely discussed, part of a high frequency experiment are the coaxial cables guiding the microwave signal to the desired location. They will be in the focus in this section. In this thesis, one has to differentiate between two areas were coaxial cables are installed, inside and outside of a cryostat. Inside, the coaxial cables have a fixed place and there is no need of flexibility, so they can be hard-wired. Outside of the cryostat, there is a need of flexibility, e.g. for rapid integration of additional microwave components into the circuit. Thus, inside a cryostat semi rigid (SR) coaxial cables find application and on the outside of a cryostat, flexible coaxial cables are used.

SR coaxial cables provide the least attenuation per unit length and the best high frequency shielding. They can be fabricated in an optimal geometry for microwave transport. Because center and outer conductor are both solid the distance between them can almost be held constant over the length of the cable. This results in propagation properties with a very low tolerance, giving almost no reflection. The excellent shielding is achieved through the solid outer conductor. This provides a continuous shield for the center conductor with no gaps like it is in the case of braided flexible cables [54]. Three different types of SR coaxial cables are used in the used cryostats. At room temperature, cables made out of copper are used, at cryogenic temperatures stainless steel cables found application, and finally at temperatures below 4 K, superconducting niobium coaxial cables were in use.

	attenuation per meter (dB/m)			
cable	at 2 GHz	at 5 GHz	at 10 GHz	at 18 GHz
SR copper (RT)	–	1.476	2.215	3.291
SR stainless steel (RT)	0.328	0.656	0.919	1.345
SR SC niobium (4.5 K)	0.21	0.22	0.25	–
flexible UFA147B	0.820	1.213	1.640	2.329
flexible True Blue	–	0.59	0.85	1.16
flexible UFA210B	0.623	0.820	1.082	1.608
dB Miser	0.326	0.493	0.763	1.053

Table 3.1.: Overview of different coaxial cables [54], [55], [56], [57], [58].

Flexible coaxial cables don't feature the same attenuations or shielding properties as SR cables do, but instead provide a great freedom of wiring. A measurement setup can be altered quickly and easily to meet the desired requirements. The flexibility comes from a non-solid outer conductor which consists of a metal braiding. This does not allow the same precision in fabrication as SR cables do, thus increasing the attenuation. Furthermore, a braiding does not continuously shield the center conductor, but can be improved by adding an additional armor. The simplest form is an aluminum foil wrapped around the outer conductor. This not only improves the shielding, in addition grants the cable a certain robustness. There is a great variety of flexible coaxial cables, greatly differing in quality. Table 3.1 shows the different coaxial cables (and their typical attenuations), used during the conducted measurements.

Lab suit up!

Barney Stinson

Chapter 4.

Millikelvin FMR

One major aspect of this thesis is the experimental demonstration of ferromagnetic resonance at millikelvin temperatures. Therefore, an existing dilution refrigerator equipped with RF wiring was used.
This Chapter gives an overview to the experimental details including RF circuitry, sample preparation, the RF measurement setup and in particular the data processing to extract the resonance conditions and the absorption line width.

4.1. Millikelvin FMR Setup

A schematic overview of the dilution refrigerator employed for measuring FMR is shown in Fig. 4.1. All experiments presented in this thesis are frequency resolved microwave transmission experiments. A vector network analyzer (Rohde & Schwarz ZVA24) emits microwave of frequency f_{MW} with a power of P_{MW} and detects amplitude and phase of the transmitted microwave. The latter is related to the first by the complex S parameter (cf. Sec. 3.3.2). The output power of the VNA is given in the Decibel (dB) scala and is related with the linear power P_{MW} via the relation:

$$P_{\mathrm{dB}} = 10 \log_{10} \left(\frac{P_{\mathrm{MW}}}{P_0} \right), \tag{4.1}$$

with P_0 as a reference power. The output power of the VNA is referenced to 1 mW and is with this given in dBm.
In this thesis, experiments are displayed with power levels down to the femto-watt regime. Therefore, additional attenuators (Aeroflex) are fitted into the circuitry at the output of the VNA, to increase its internal minimal output power of -44 dBm.

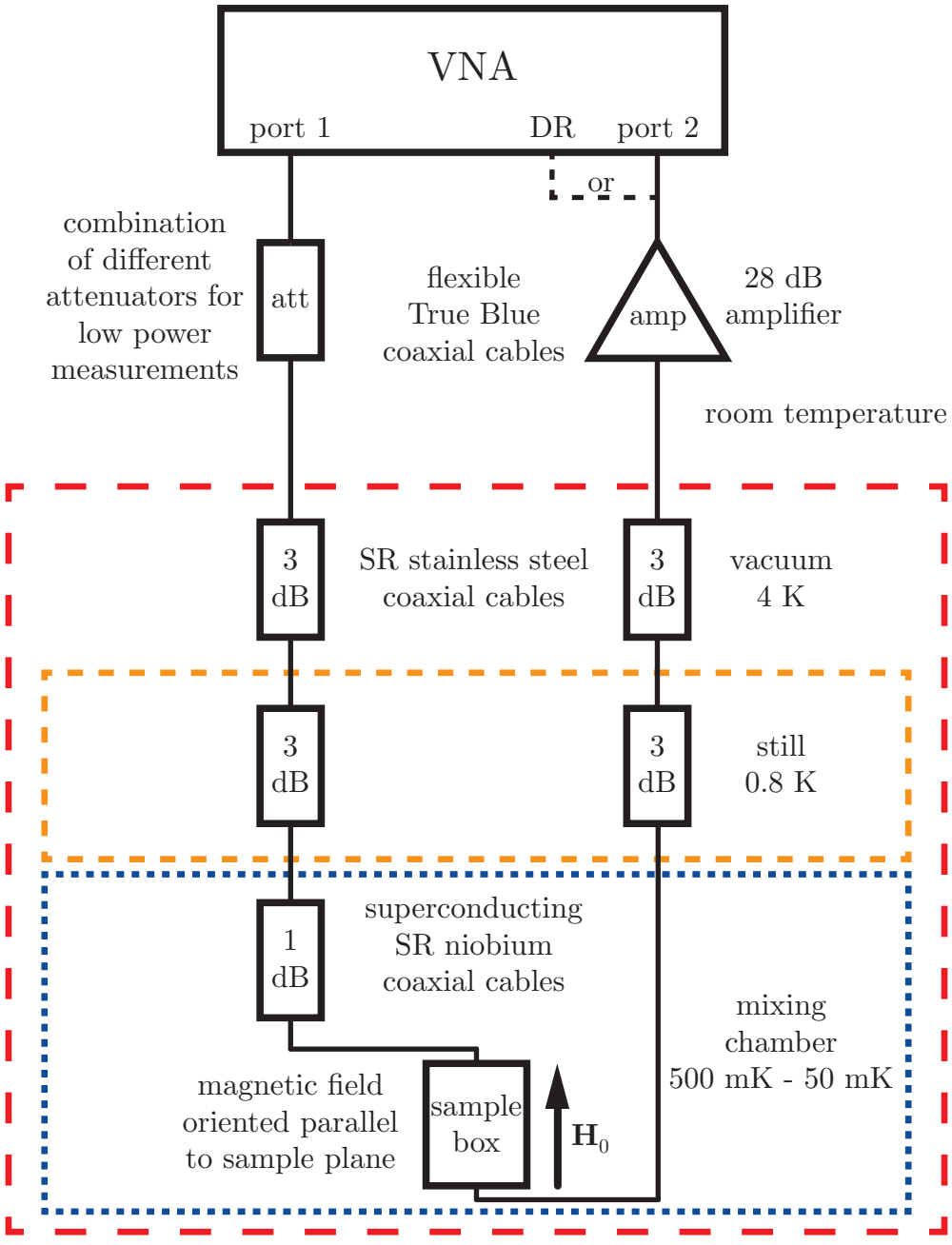

Figure 4.1.: Overview of the microwave wiring of the millikelvin FMR setup, showing the various microwave components used. At the bottom the sample box is located with the orientation of the static magnetic field $\mathbf{H}_0$. The colored boxes define the different temperature stages.

The VNA is connected with the RF ports of the dilution refrigerator by Teledyne Reynolds TrueBlue flexible coaxial cables. Inside the fridge SR stainless steel coaxial cables are fed through a vacuum port of the dilution fridge to the 4 K flange (cf. Fig. 4.1 and 4.2). Here, the cables are thermally anchored using a 3 dB attenuator. The attenuator is a T-shaped resistor network, connecting the inner and outer conductor with a shunt resistor. Hereby, thermal conductance between inner and outer conductor is established, because the thermal conductance of the insulating dielectric, made of Teflon, is significantly lower. Between the 4 K flange and the still, superconducting SR Nb - Nb/Co coaxial cables are used to reduce microwave attenuation while at the same time improve thermal isolation between the temperature stages. At the still-level again a 3 dB attenuator is mounted to anchor the inner and outer conductor thermally, followed by a superconducting coaxial cable to the sample box. Here, a 1 dB attenuator is mounted directly in front of the sample box to provide thermal equilibration between inner and outer conductor inside the sample box. The signal from the output port of the sample box is directed to room temperature in a similar fashion. In front of the VNA input port, the signal is either directly connected to the input port or to the direct receiver access (cf. Sec. 3.3.1). For ultra low power experiments a room temperature

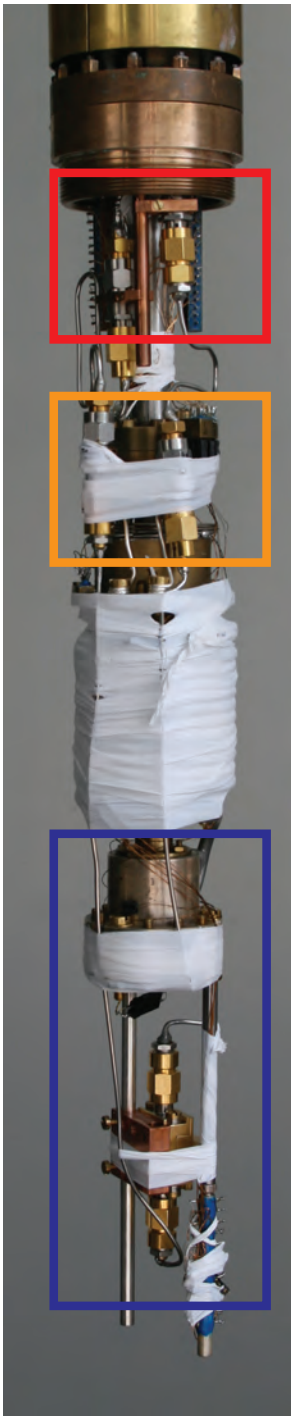

Figure 4.2.: Picture of the dilution refrigerator, with the different temperature-stages marked.

amplifier (Kuhne KU LNA BB 2533 A) is used.
Figure 4.2 shows the dilution refrigerator, with all the RF installations visible. During operation, a vacuum cap is screwed on and the inside of the system is evacuated for thermal isolation. The system is then immerged in liquid ^{4}He provided by a Dewar equipped with a superconducting solenoid (-9 to $+9$ T) at the location of the sample. This specific dilution refrigerator can be cooled to a stable temperature of 50 mK at the mixing chamber. Thermal coupling of the sample box is realized by a silver rod. The temperature is measured resistively by a ruthenium oxide, calibrated thin film resistor. With a resistive heater, mounted at the mixing chamber, the temperature can be varied in a range of 50 mK to 500 mK. A cooling power of 17 μW at 100 mK is available and imposes limitation on the incident microwave power. Furthermore, the magnetic field $\mathbf{H}_0$ needs to be ramped slowly, to prevent eddy currents from excessively heating the mixing chamber.

4.2. Sample Preparation

Initial experiments at millikelvin temperatures concentrated on the well known material, Cobalt. Cobalt is a transition metal with the atomic number 27. Below its Curie temperature T_C of 1388 K, it is ferromagnetic. It has a magnetic moment of 1.6 - 1.7 Bohr magnetons μ_B per atom with a total saturation magnetization $\mu_0 M_\mathrm{S}$ of 1.466 T and the g-factor is 2.15 [59]. The Gilbert damping parameter α is 0.019 [36], which is for Cobalt temperature independent and such making it most suitable for testing the FMR setup.
A schematic of the Cobalt sample is shown in Fig. 4.3. Cobalt is deposited as a 50 nm thick thin-film on a 3 by 3 mm^2 silicon substrate ($\rho > 3000$ Ωcm). The Cobalt thin-film is placed onto a CPW (Sec. 3.4.1), which is already mounted and connected inside a sample box. It is fixed after placement with respect to the CPW by rubber cement.

4.3. Initial Experiments and Data Processing

First, data acquired at a temperature of 4.2 K will be presented. Here, the dilution refrigerator is inserted in the Dewar, filled with liquid He^4. The sample is only cooled by the liquid helium-4 and not through operating the dilution refrigerator, and thus

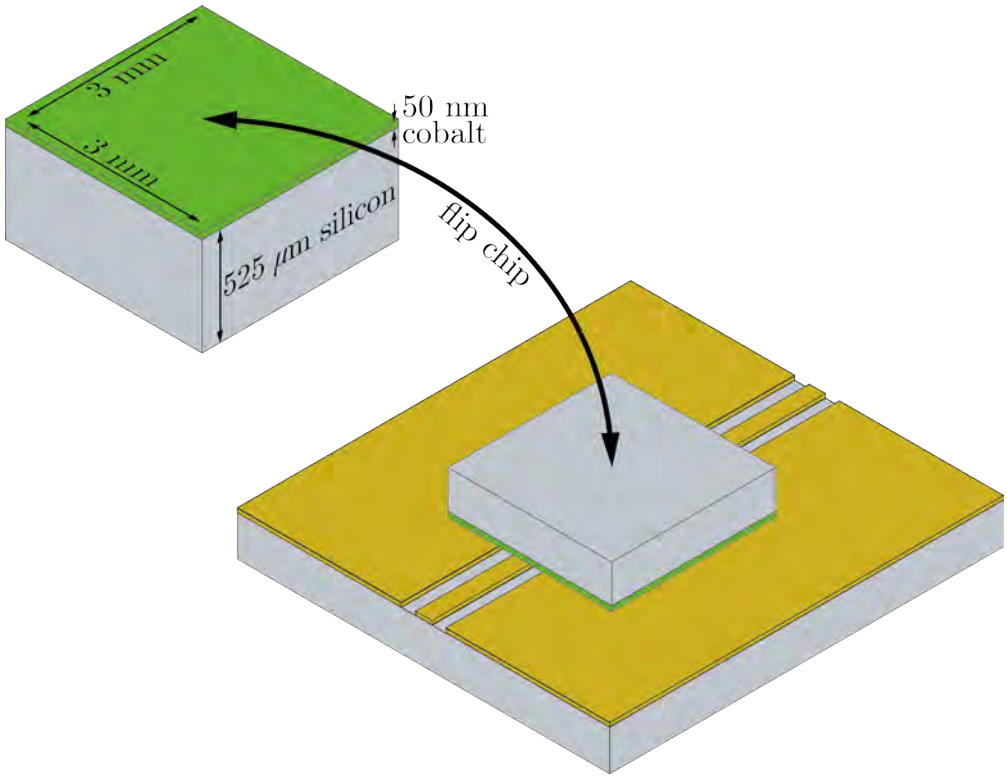

Figure 4.3.: Depicted sample build-up and its schematic placement on the CPW, via the flip-chip method.

the temperature is stable at 4.2 K. Measurements were performed by applying a constant static magnetic field H_0 and simultaneously feeding a microwave signal, with varying frequency, from the VNA to the sample. The microwave frequency f is swept from 10 MHz to 24 GHz in 12 MHz steps, with an IF bandwidth of 100 Hz [60], resulting in 2000 frequency points per sweep. During every frequency sweep, the real- and imaginary-part of the transmitted microwave signal is measured by the VNA. The frequency sweep is performed for different magnetic fields H_0. H_0 ranges from -0.5 T to +0.5 T, in 2 mT steps, resulting in 500 magnetic field points. For this measurement the incident microwave power was -20 dBm had been chosen, which was attenuated to approximately -30 dBm at the sample, due to the attenuators and finite losses of the coaxial cables.The data is saved in matrix form, with its columns representing the frequency points and its rows the magnetic field points, resulting in a 500 by 2000 matrix, for the real- and imaginary-part each.
The data processing is done with *MATLAB*. At first the magnitude $|S_{21}|$ of the trans-

mission is calculated, from the real- and imaginary-parts:

$$|S_{21}| = \sqrt{(S_{21\ \mathrm{real}})^2 + (S_{21\ \mathrm{imag}})^2}. \tag{4.2}$$

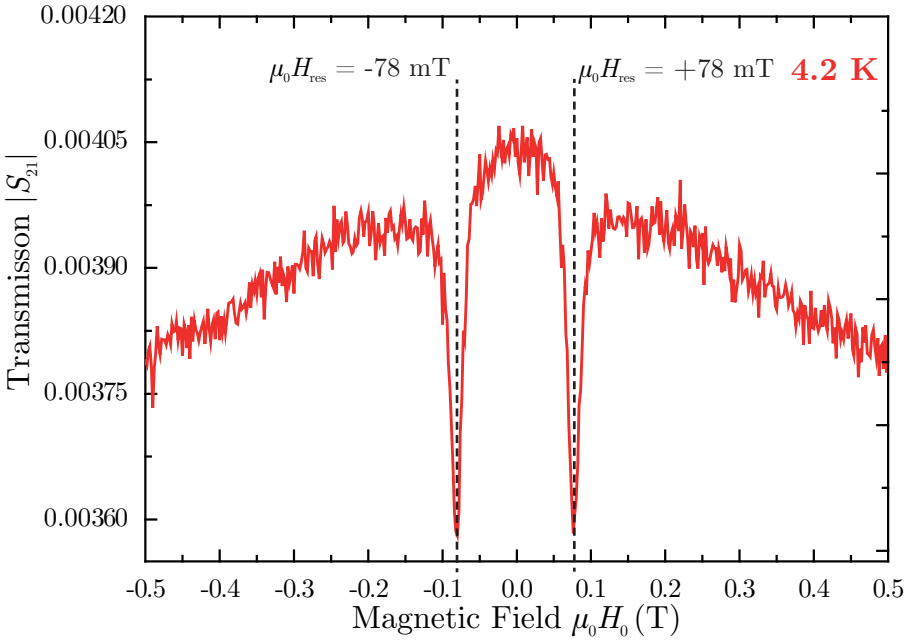

Figure 4.4.: Plot of the magnitude $|S_{21}|$ as a function of the magnetic field $\mu_0 H_0$ for a frequency $f = 13.258$ GHz. Two resonances, symmetrical at a resonance field $\mu_0 H_{\mathrm{res}} = \pm 78$ mT are visible.

The broadband measurement allows two ways to observe FMR in the detected signal. As discussed in Sec. 2.5, the resonance phenomenon FMR can be described as a function of frequency f for fixed external magnetic field $\mu_0 H_0$ or vice versa.
One way to discern the FMR signal, is to plot the magnitude $|S_{21}|$ for varying magnetic field at a fixed frequency. Figure 4.4 shows clearly two symmetric FMR dips, with no further data processing needed. The resonance fields $\mu_0 H_{\mathrm{res}}$ are ± 78 mT for a fixed frequency $f = 13.258$ GHz.
The second way is to plot the magnitude $|S_{21}|$ for varying frequency, with the magnetic field held constant. Figure 4.5 (a) shows for a fixed magnetic field $\mu_0 H_0 = 78$ mT the broadband frequency response. Starting from low frequencies with a high transmission of 0.024, the transmission rapidly decreases to a bare level of 0.006. This transmission range is significantly larger than the resonance effect to be observed and therefore the FMR resonance is not prominently identifiable [60]. To definitely observe the FMR

absorption dip, the frequency dependent part of the transmission is subtracted, in form of a reference broadband frequency response. For reference, a magnetic field is chosen, where no FMR is expected in the entire frequency range (here $\mu_0 H_0 = 498$ mT). Figure 4.5 (b) shows the reference corrected transmission at 78 mT. Here, the FMR can be identified at a resonance frequency f_{res} of 13.258 GHz. The spectrum contains, apart from the FMR dip, several other resonances, which where not removed by the subtraction of the reference transmission. These additional resonances are attributed to standing electromagnetic waves, where the inside of the sample box acts as a resonator cavity. These standing waves or box resonances show a small dependency

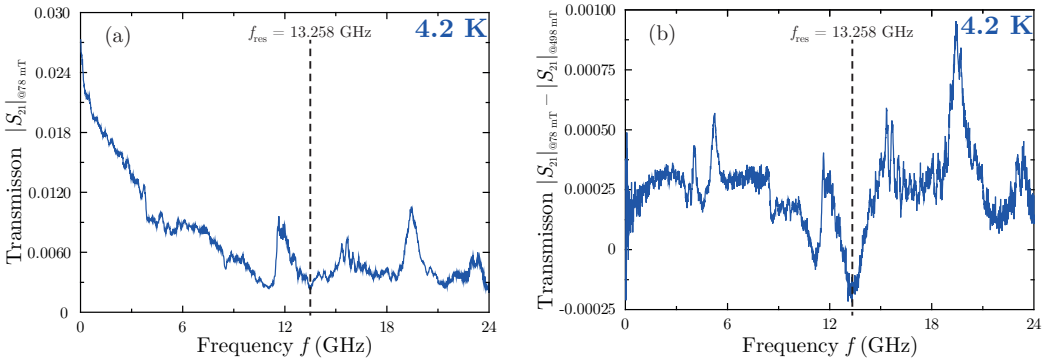

Figure 4.5.: (a) Plot of the magnitude $|S_{21}|$ with respect to frequency f for a magnetic field $\mu_0 H_0 = 78$ mT. The FMR can not be seen clearly. (b)Plot of the magnitude $|S_{21}|$ with respect to frequency f for a magnetic field $\mu_0 H_0 = 78$ mT, where a magnitude at $\mu_0 H_0$ of 498 mT has been subtracted. The FMR can be seen at a frequency f of 13,258 GHz.

in the magnetic field H_0. It is assumed, that the dependency is caused, due to a magnetoresistance effect of the sample boxes material. Thus, with varying magnetic field $\mu_0 H_0$ the propagation properties, for the electromagnetic waves, change and consequently the resonance conditions for standing waves. Therefore, the additional resonances, seen in the broadband frequency response, are not overlapping for two different magnetic fields and are not removed by the reference correction. These resonances are more effectively distinguished in the dispersion plots, which will be shown later.

To get a total overview of the dispersion of the FMR over frequency and magnetic field, the matrix of the magnitude $|S_{21}|$ can be displayed in a color plot, with the magnetic field values in x-axis, the frequency f in y-axis and the magnitude is encoded in a color scale. In the following called dispersion plot as depicted in Fig. 4.6, with low

transmission encoded in black and high transmission in white. Symmetrically about zero magnetic field a V-shaped line is is faintly visible, representing the FMR. The

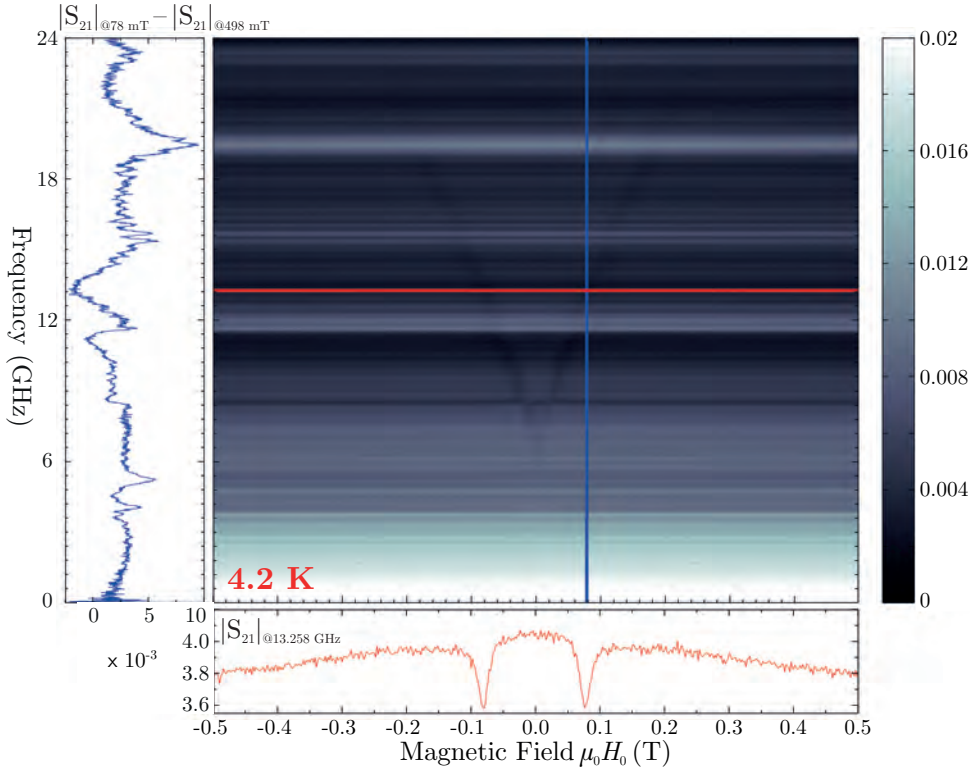

Figure 4.6.: Magnitude $|S_{21}|$ displayed in a color plot, with the magnetic field $\mu_0 H_0$ on the x-axis, the frequency f on the y-axis and the magnitude encoded in the color code. In the left plot is the magnitude with respect to the frequency displayed, with a subtracted reference transmission. This plot corresponds to the blue vertical line in the color plot. At the bottom the magnitude with respect to the magnetic field is plotted, which corresponds to the red horizontal line.

absence of a clear contrast is due to the same reasons as discussed for Fig. 4.5 (a) and (b). To increase the contrast a mean background is subtracted from the data. For each frequency the mean magnitude over the magnetic field is calculated and then subtracted:

$$\Delta|S_{21}|(f) = |S_{21}(H_{0\ m}, f)| - < |S_{21}(H_{0\ m}, f)| >, \tag{4.3}$$

with $< . >$ denoting the arithmetic mean. The dispersion plot from Fig. 4.6 with subtracted mean background is shown in Fig. 4.7. The dispersion of the FMR is clearly distinguishable from the background, making this the standard way of processing the following FMR data. One sees immediately under which conditions FMR

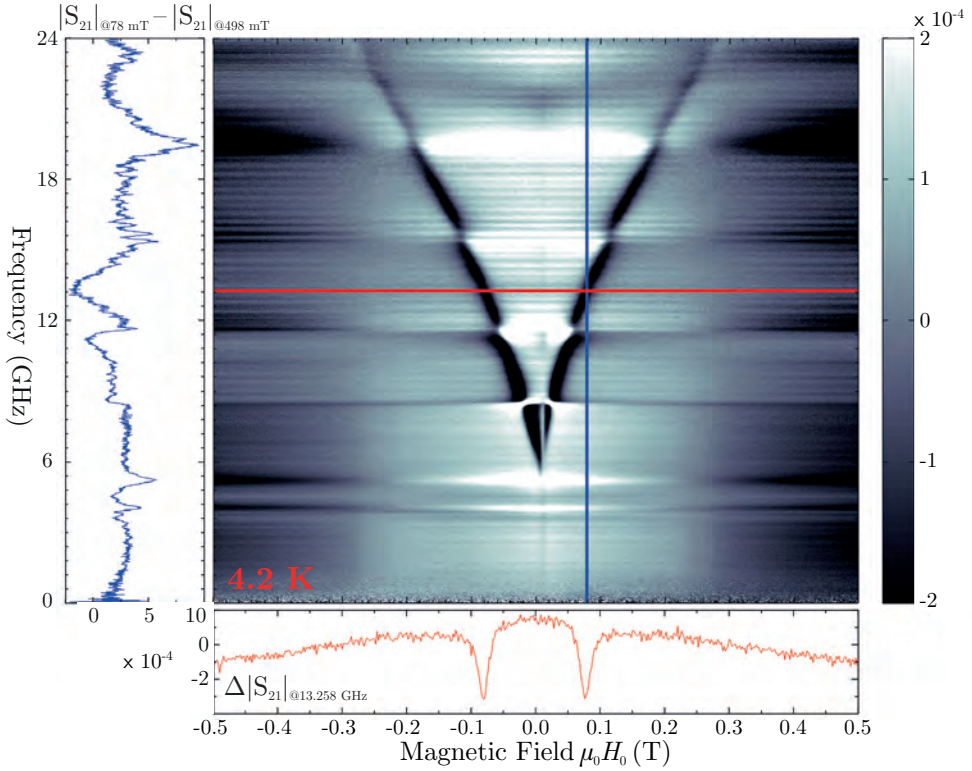

Figure 4.7.: Color plot of the magnitude $\Delta|S_{21}|$ with a mean background subtracted.

is achieved, showing where the reference transmission lies, for the magnitude plots like in Fig. 4.5 (b). From the color plot the origin of the disturbed magnitude plot in the frequency direction can be seen. During the frequency sweep there are several resonances distorting the FMR absorption dip. There are no such resonances during the magnetic field sweep, hence the much smoother spectrum of the magnitude in the magnetic field direction. Due to the even spectrum in the magnetic field direction, these will be used for the line width determination, needed for the Gilbert damping parameter calculation.

The abrupt reduction in transmission for $|\mu_0 H_0| > 250$ mT, results from reaching the critical magnetic field of the superconductor for the temperature of 4.2 K. At this point the coaxial cables resistance becomes finite, increasing the losses of the cable and additionally changing their characteristic impedance. The change in impedance increases the reflection of the microwave at the interface of the 50 Ω impedance matched stainless steel coaxial cables and the CPW with the niobium coaxial cables. A measurement with the same parameters, as in the 4.2 K measurement, was con-

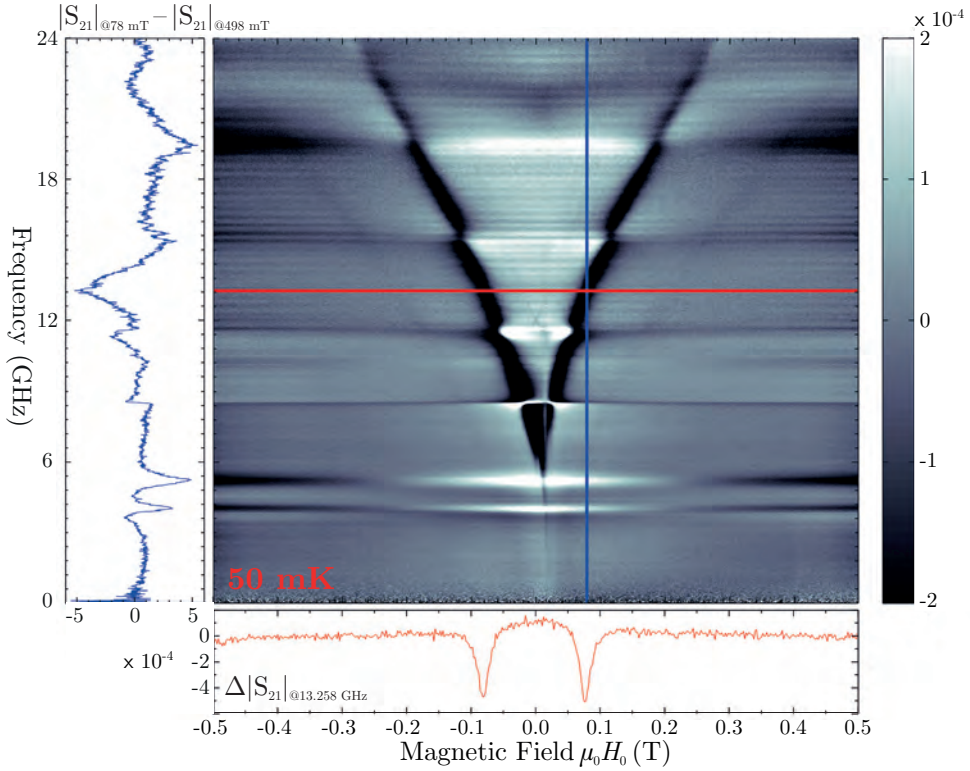

Figure 4.8.: Color plot of the mean background corrected magnitude $\Delta|S_{21}|$ for a temperature of 50 mK.

ducted at 50 mK and is plotted in Fig. 4.8. The 50 mK data shows a smoother background in comparison with the 4.2 K data. The superconductivity of the niobium coaxial cables is also maintained over the magnetic field range at this temperature. Additional features in the color plot, apart from the FMR dispersion, will be discussed in Sec. 4.7. To get a better view of the difference between the two measurements at different temperatures, the magnitudes $\Delta|S_{21}|$ with respect to the magnetic field $\mu_0 H_0$ at a frequency f of 13.258 GHz are compared in Fig. 4.9. The line shape of the two plots are the same, meaning that the conditions for FMR are not changing from 4.2 K to 50 mK. However, it can clearly be seen that the signal to noise ration is enhanced for the 50 mK measurement. Comparing the absorption dips, one obtains an improvement of the signal to noise ratio by a factor of around 1.4.
Demonstrated, that the millikelvin FMR setup is working, the next step is to compare the obtained data with theory and literature values.

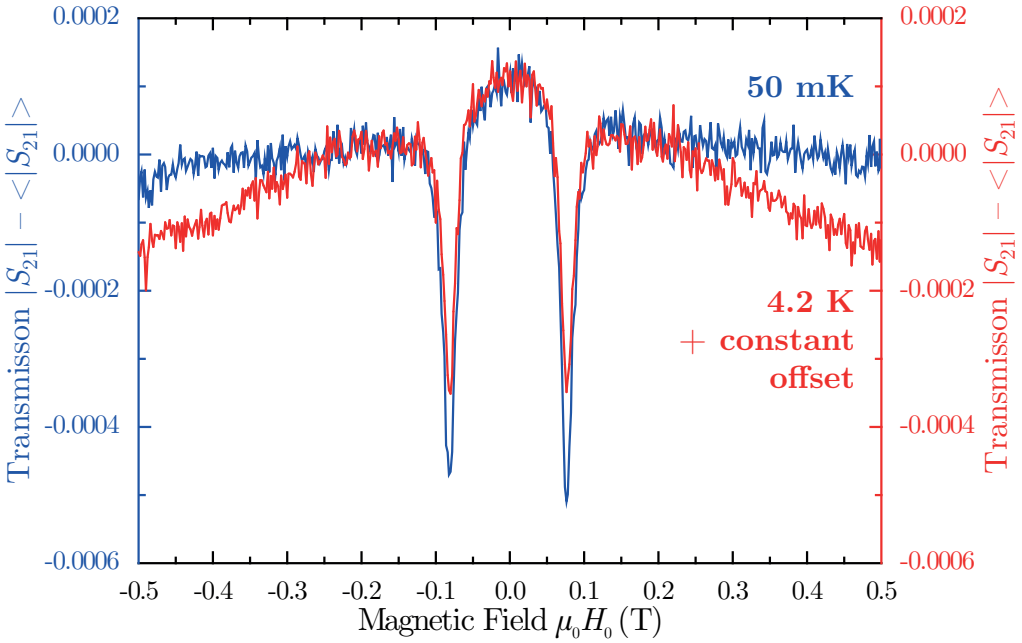

Figure 4.9.: Comparison of the 4.2 K with the 50 mK magnitudes $\Delta|S_{21}|$ over magnetic field $\mu_0 H_0$ at a frequency f of 13.258 GHz. The 4.2 K plot has been shifted by a constant offset of -0.3562×10^{-4}, so the resonance dips of both measurements are at the same height.

4.4. Comparison to Theory

The dispersion of the FMR can be calculated, by using a free energy approach, as introduced in Sec. 2.4. A free energy F of the form, given in Eqn. 2.19 was used, with a Zeeman term, a demagnetization term and an uniaxial anisotropy term. The coordinate system is defined as in Fig. 2.4, with the magnetic field $\mathbf{H}_{\text{eff}}$ aligned in the film plane. With Eqn. 2.17 the resonance frequency $\omega_{\text{res}} = 2\pi f_{\text{res}}$ is calculated. For the calculation a demagnetization field $\mu_0 M_{\text{S}}$ of 1.592 T, an uniaxial in-plane anisotropy field $\frac{K_{\text{uni}}}{M_{\text{S}}}$ of 15 mT, a g-factor of 2.15 and a Gilbert damping parameter α of 0.02 have been considered. In Fig. 4.10 the resulting theoretical curve is plotted as a red line on a dispersion plot, obtained for a 50 mK measurement with an effective microwave power at the sample of -30 dBm. The theory describes the experiment very well, apart from the distortions of the experimental dispersion. The for the calculation used parameters are comparable with corresponding literature values for Cobalt [61], [36], [62].

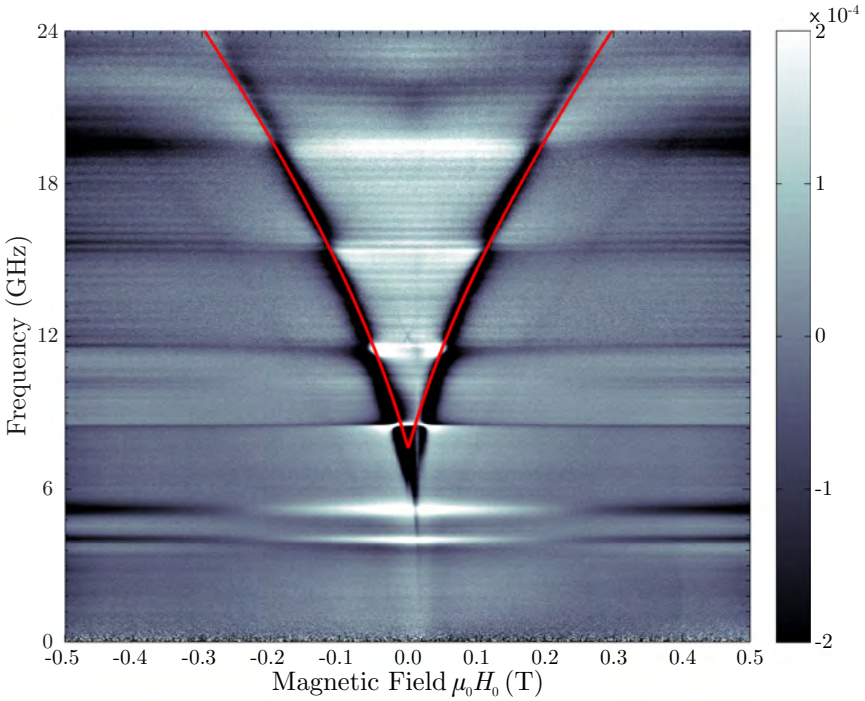

Figure 4.10.: Measured dispersion of the FMR at 50 mK, overlayed with a calculated dispersion (red curve).

4.5. Low Microwave Power Series

To test the limit of sensitivity of the millikelvin FMR setup, a series of measurements was conducted, where the incident microwave power is reduced step by step. The setup is expanded by an additional 50 dB attenuator at the output of the VNA and a 28 dB amplifier at the direct receiver access, which was used as the input port. The data plots had been corrected by the additional attenuation and amplification, so the different plots get comparable. To match the different measurements, the linear scaled magnitude $|S_{21}|$ is translated into a dB scale. The attenuation is simply added to the magnitude. To compensate for the effects of the broadband amplifier and the direct receiver, their transmission spectra were recorded. The dB scaled transmission was measured, with only including these components in the microwave circuit. The acquired magnitude spectra were subtracted from the FMR magnitude spectra, for every magnetic field point. Afterwards the scale of the magnitude is translated back and the "dB matched" data set is used to calculate the background corrected magnitude $\Delta|S_{21}|$. For frequencies higher than 20 GHz there is an increase in background noise in the dispersion plots in Fig. 4.11. This is caused by the amplifier,

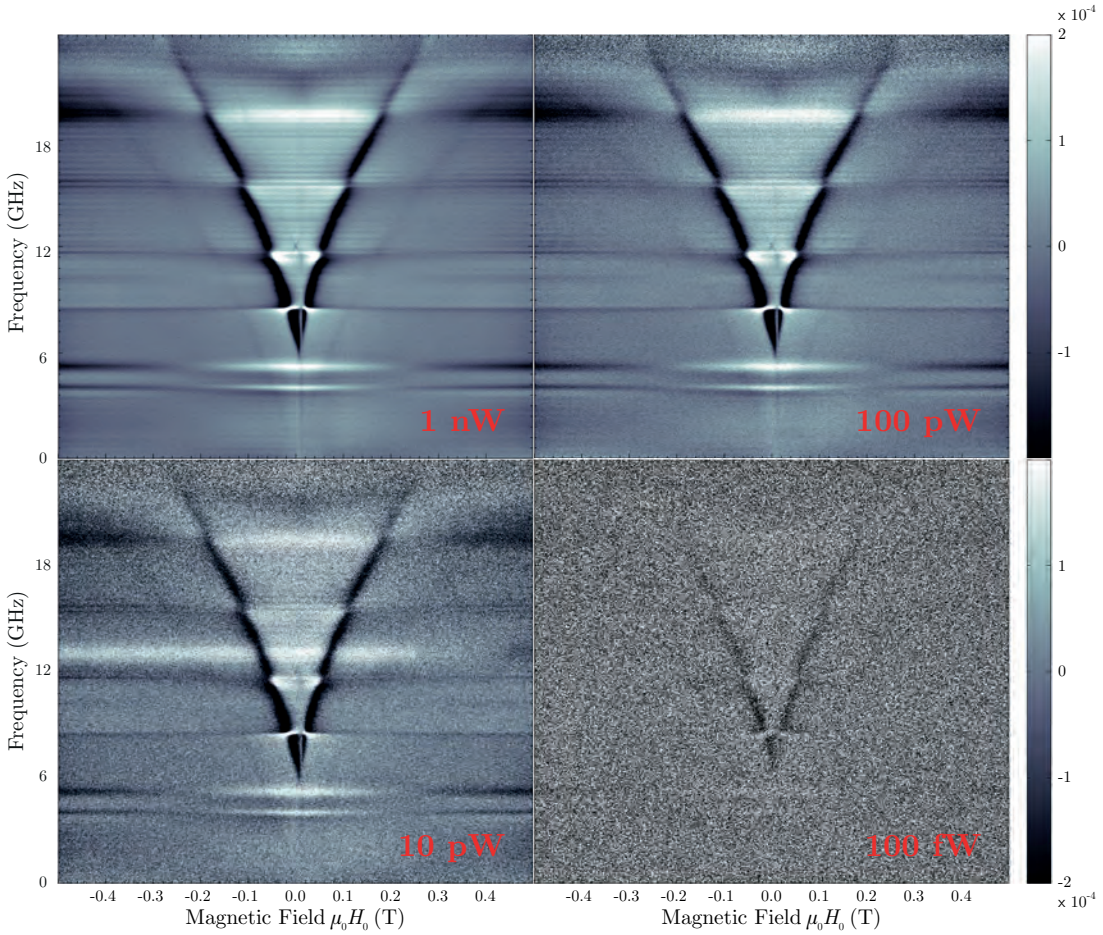

Figure 4.11.: A series of FMR measurements, conducted at different incident microwave power. The stated powers are the effective powers at the sample, taking the attenuation into account.

that is only specified for frequencies up to 20 GHz [63]. The series started with a VNA output power of 0 dBm, corresponding to a effective power at the sample of -60 dBm or 1 nW. The top left dispersion plot in Fig. 4.11 shows this measurement. The FMR line is clearly recognizable from the smooth background. For the next measurement the power output was set to -10 dBm, corresponding to an effective power of 100 pW. The background noise increases, but the FMR with its details are still distinguishable. At an effective power of 10 pW, features, apart from the FMR, get lost in the background, but the curve of the FMR stays concise. At last, with an effective power of 100 fW the spectrum is dominated by very strong background noise. The curve of the FMR is faintly recognizable, but with a signal to noise ratio of the order of one, the evaluation of the absorption dips is no longer possible.

The line width $\mu_0\Delta H$ of the absorption dips is connected with the Gilbert damping parameter α (Sec. 2.5). Measurements at different powers test for any dependency of the microwave power in the line shape. Figure 4.12 displays the dB matched magnitudes $\Delta|S_{21}|$, plotted against the magnetic field $\mu_0 H_0$ for a frequency f of 13.258 GHz, of the measurements conducted at 1 nW, 100 pW and 10 pW. The 100 fW measurement is not included, due to the high noise level. It can be seen, that the shape of the resonances is not changing with the incident microwave power.

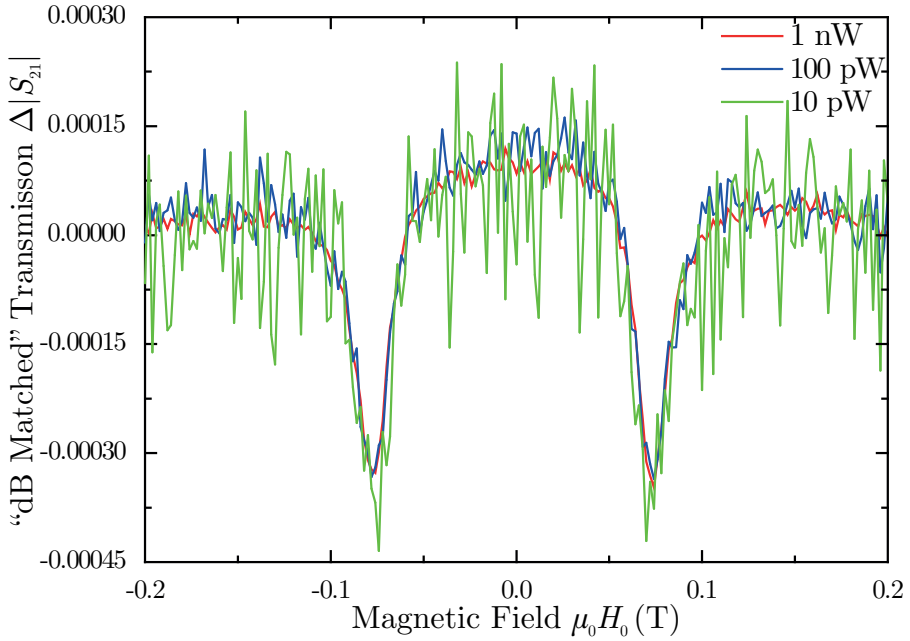

Figure 4.12.: Comparison of the magnitude $\Delta|S_{21}|$ with respect to the magnetic field $\mu_0 H_0$ for a frequency f of 13.258 GHz, at different incident microwave powers. The plots were normalized to compensate for amplification and attenuation.

4.6. Gilbert Damping Acquisition

To extract the Gilbert damping parameter α from the millikelvin data. Equation 2.21 states, that for Gilbert damping, the line width $\mu_0\Delta H$ is increasing linear with with frequency f. From the slope of the line α can be extracted. To determine the line width the absorption dips in the data set, cut along the magnetic field axis were fitted for a range of frequency points. Fitting the magnitude data has the advantage of one less fitting parameter compared to the fitting of the real- and imaginary-part data,

namely the phase. To obtain a suitable fit function the magnitude of Eqn. 2.33 and 2.34 is calculated.

$$y(\mu_0 H_0 = B_0) = \sqrt{\chi'(B_0)^2 + \chi''(B_0)^2} \rightarrow (-1) \cdot \frac{\mu_0 M_\mathrm{S}}{\sqrt{(B_\mathrm{res} - B_0)^2 + (\frac{\Delta B}{2})^2}} + y(0). \quad (4.4)$$

The function is additionally multiplied by a factor of (-1), so absorption curves can be described. A $y(0)$ is added to the function, to account for an offset due to background. Although, Eqn. 4.4 describes the data correctly, a Lorentzian function was used to fit the data, because of better computability:

$$y(B_0) = (-1) \cdot \mu_0 M_\mathrm{S} \frac{\frac{\Delta B'}{2}}{(B_\mathrm{res} - B_0)^2 + (\frac{\Delta B'}{2})^2} + y(0). \quad (4.5)$$

The resonance position B_res and the amplitude are the same as in Eqn. 4.4, but the line width ΔB and $\Delta B'$ differ by a factor of $\sqrt{3}/2$:

$$\mu_0 \Delta H = \Delta B = \frac{\sqrt{3}}{2} \Delta B'. \quad (4.6)$$

Keeping this in mind, the obtained parameters can be correctly translated.
To analyze the actual data with respect to the FMR line width the following procedure was used: First, the dispersion is calculated by using the simulation of Sec. 4.4. The theoretical values for the resonance field B_res are used as the center of the fit interval and as a starting parameter for the fit. On the defined interval a linear detrend is performed, to create an even baseline. For the fitting, cuts of the dispersion plot at fixed frequencies were chosen, where the the FMR dispersion line displays no distortions, like it is the case for the frequency range of 16 to 18 GHz and positive magnetic fields. The Lorentzian fit optimizes with the least square method, by reducing the squared error of the fitted function to the actual data. The error reduction is done by iteratively changing the fitting parameters, which are the given by the Lorentzian function: The offset $y(0)$, the amplitude $\mu_0 M_\mathrm{S}$, the resonance field B_res and the line width ΔB.
The fitting was done using *MATLAB*. For a measurement at 50 mK with an effective microwave power of 1 μW the resulting fitted line width is plotted against frequency in Fig. 4.13. To estimate the Gilbert damping parameter the curve was fitted with a

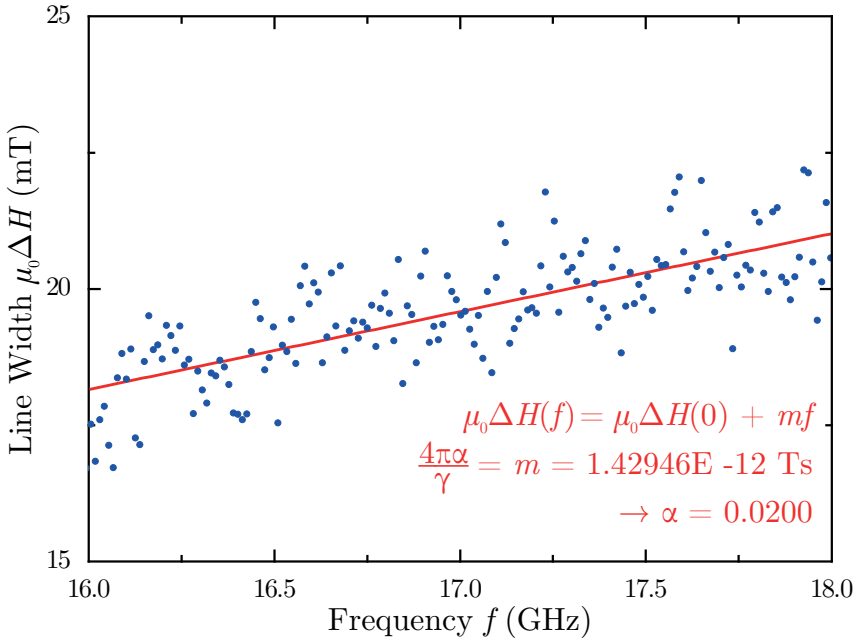

Figure 4.13.: Fitted line width $\mu_0\Delta H$ over frequency f. From a linear fit (red line) the Gilbert damping parameter α is extracted.

linear fit. The slope m of the line gives rise to the Gilbert damping parameter.

$$\begin{aligned} \mu_0\Delta H(f) &= \mu_0\Delta H(0) + mf \\ \text{with} \quad m &= 4\pi\frac{\alpha}{\gamma} \Longrightarrow \alpha = \frac{\gamma m}{4\pi}. \end{aligned}$$

The linear fit gives an α of 0.0200 $\pm$0.0013. The measured value is consistent with the damping parameter for Cobalt found in literature [23]. The presented experiments demonstrate, that the millikelvin FMR setup allows to measure broadband FMR in a quality sufficient to evaluate Gilbert damping at millikelvin temperatures.

4.7. Additional Features

The dispersion plots of the 50 mK measurements show apart from the FMR of Cobalt additional features. Figure 4.14 depicts a dispersion plot obtained with an effective microwave power at the sample of 1 nW. In the figure various are highlighted with different colors.
First the features marked with red arrows and a circle shall be discussed. The feature

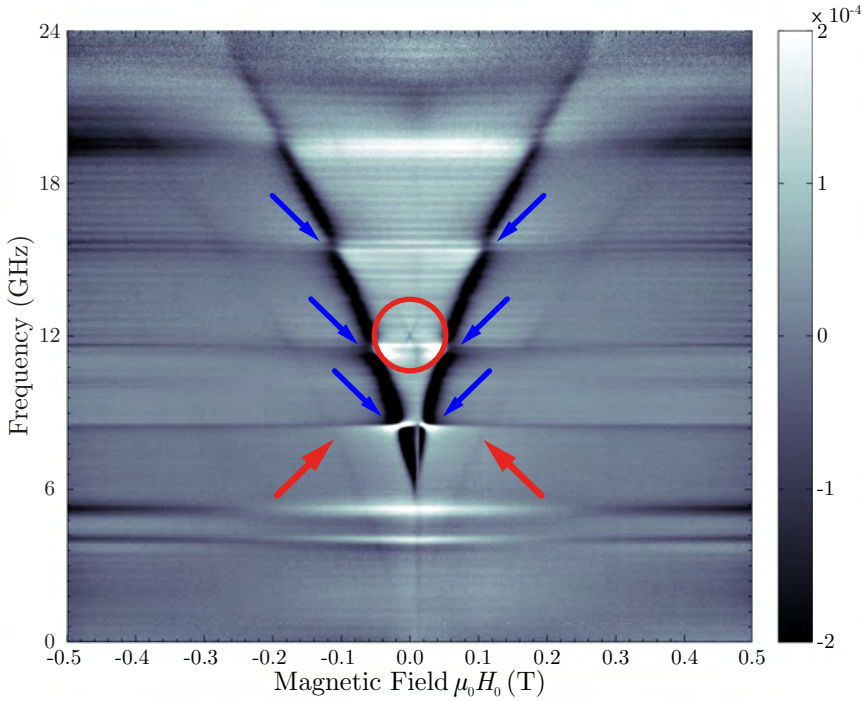

Figure 4.14.: Dispersion plot of a 50 mK measurement with an effective microwave power of 1 nW. Additional features are marked by blue and red arrows or a red circle.

indicated by the arrows consist of a V-shape, starting at zero magnetic field and frequency, looking much like a FMR dispersion. The second are crossed thin absorption lines, in the center of the plot. To rule out that these features are not caused by the Cobalt sample a reference measurement was conducted. The Cobalt sample was removed from the CPW. The reference measurement conducted at 50 mK and an effective microwave power of 100 pW at the CPW, is displayed in Fig. 4.15 together with the cobalt measurement from Fig. 4.14. To compare the plots, the reference measurement is placed once to the right of the Cobalt measurement and once to its bottom. First, only looking at the reference measurement, an increase in transmission is observed, compared to the Cobalt measurements. This is due to the fact that the unloaded CPW is matched to the characteristic impedance of the coaxial cables, which is not the case for a loaded CPW. The sample brought on the CPW changes the impedance and such decreasing the transmission. Furthermore, the additional box resonances are different from the ones seen in the Cobalt measurements. The absence of a sample changes the resonance condition for the standing electromagnetic

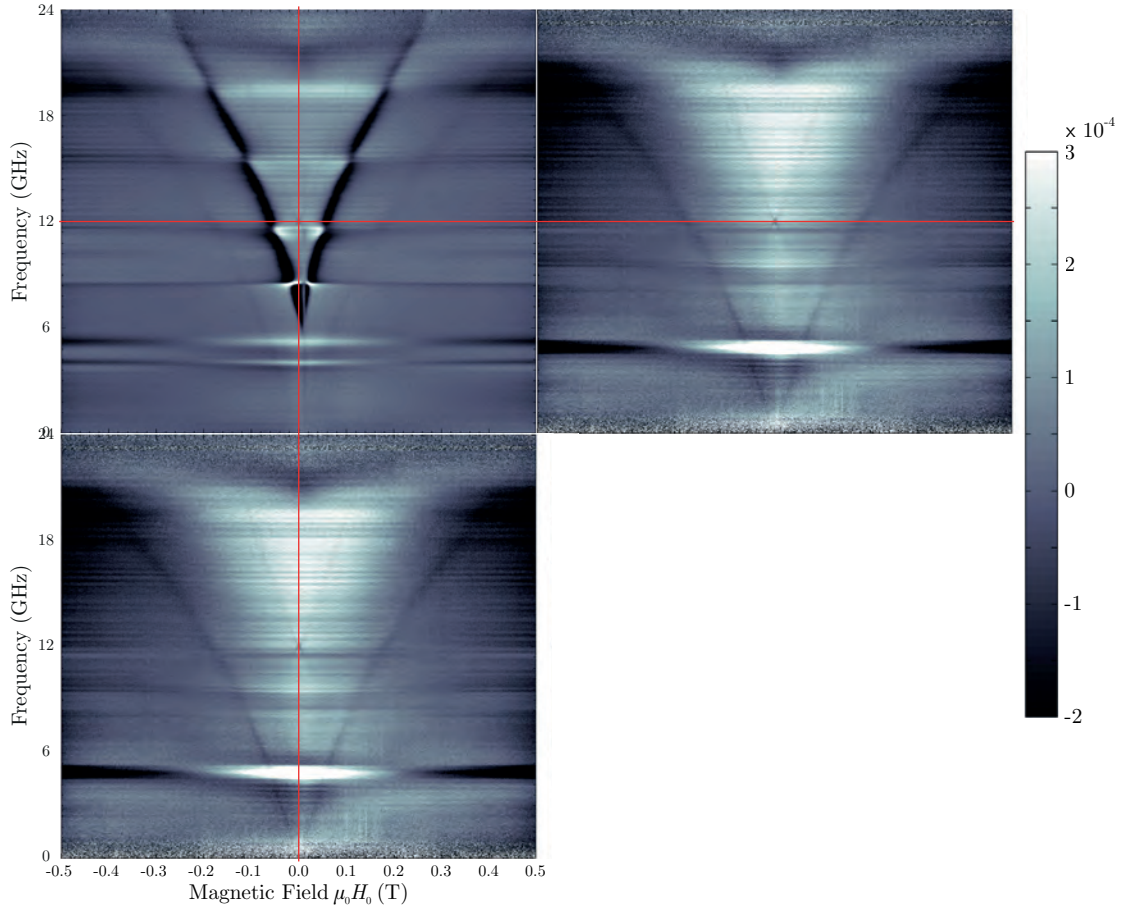

Figure 4.15.: Comparison of the Cobalt measurement (top left) with the measurement of the sample box with an unloaded CPW (top right and bottom left). The red lines serve as a guide for the eyes.

waves, thus altering the observed box resonances.

Comparing now the features, one sees, that the features are present in both dispersion plots and are positioned equally. Therefore, the origin of these features cannot be attributed to the Cobalt sample. It is assumed, that they are caused by the connectors, mounted on the sample box. The connectors contain some portion of nickel, which may be responsible for these features. Given that their origin is not the sample and because they are not interfering with the initial measurement of Cobalt, they are declared as a feature of the measurement setup, having nothing to do with intended FMR measurements.

The features marked blue, look much like avoided crossings of the FMR dispersion with some of the very prominent box resonances. Since the parameters of these box

resonances are not known, a definite identification of an anti-crossing is not possible. But the similarity to such an anti-crossing gave rise to the experiments performed in Chapter 6. There, a quantitatively analyzes of the coupling between spin waves and photons will be made.

Open your brain tank, bro, ´cause
here comes some premium
91-octane knowledge.

Barney Stinson

Chapter 5.

Temperature Dependence of Holmium Doped Permalloy

This Chapter is based on the publication "*Damping by Slow Relaxing Rare Earth Impurities in $Ni_{80}Fe_{20}$*" published by G. Woltersdorf *et al* [8]. Here, the dependency of the rare earth (RE) doping in $Ni_{80}Fe_{20}$ (Permalloy) thin films on the Gilbert damping parameter α was investigated. The original experiments have been performed in the temperature range from 350 K to 100 K for different RE dopants in Permalloy employing FMR spectroscopy within a frequency range of 0.5 - 35 GHz. The data was explained by the slow relaxing impurity model [64], [5], allowing to describe the temperature dependence of the FMR line width.
In this Chapter the temperature range is extended to the millikelvin range using the broadband approach discussed in Chapter 4. More importantly, an up-to-now undocumented shift of the FMR resonance position is observed and discussed.

5.1. $Ni_{80}Fe_{20}$:Ho_1

In order to be able to compare the published dataset with the ones extended to low temperatures, samples are provided by G. Woltersdorf. Permalloy is an alloy consisting of 80 % nickel and 20 % iron. It is known for its high permeability and features also a small coercivity and a near zero magnetostriction [9]. Permalloy has a typical saturation magnetization $\mu_0 M_S$ of 1.169 T and a Gilbert damping parameter α of 0.0064 at room temperature [9]. The investigated Permalloy is doped with one atomic percent of Holmium ($Ni_{80}Fe_{20}$:Ho_1). Holmium has the atomic number 67, is found in the lanthanide series, and it has a very high magnetic moment of 10.9 μ_B

[9].
The thin film sample was grown by dc magnetron co-sputtering from single element targets. On a glass substrate a seed layer of Tantalum (Ta) was deposited with a thickness of 1 nm. On top a 30 nm thick $Ni_{80}Fe_{20}$:Ho_1 film was sputtered and covered with a 3 nm thick Ta layer to prevent oxidation (cf. Fig. 5.1) [8]. The sample is mounted on a CPW as shown in Sec. 4.2.

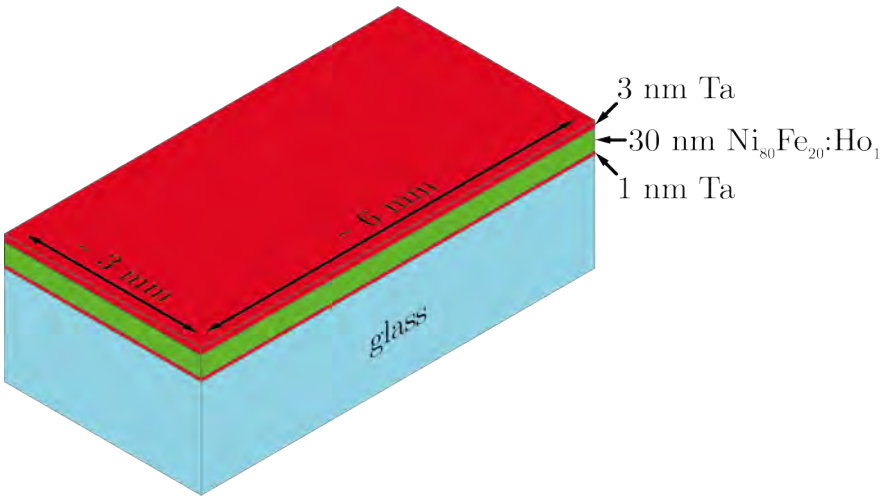

Figure 5.1.: Schematic layer structure of the $Ni_{80}Fe_{20}$ thin film doped with one atomic percent of Ho.

5.2. Magnet Flow Cryostat FMR Setup

Ferromagnetic resonance was measured as a function of the sample temperature from 300 K to 4 K in the flow cryostat setup discussed in Sec. 3.2. A schematic overview of the RF wiring is depicted in Fig. 5.2. For this dataset the VNA is connected with the sample holder via two 3 m long, flexible UFA147B coaxial cables. Short SR copper coaxial cables provide the feed through to the gas filled VTI. Close to the room temperature section the copper based cables are changed to stainless steel SR coaxial cables, to insulate the sample box from room temperature and lower the heat load. The limited space in the VTI only allows one connector of the sample box to be connected straight to the SR stainless steel coaxial cables. For the second connection the cable needs to be bent. In particular, this was realized by an additional short SR copper coaxial cable. A copper cable was used, because it allows for a smaller bending

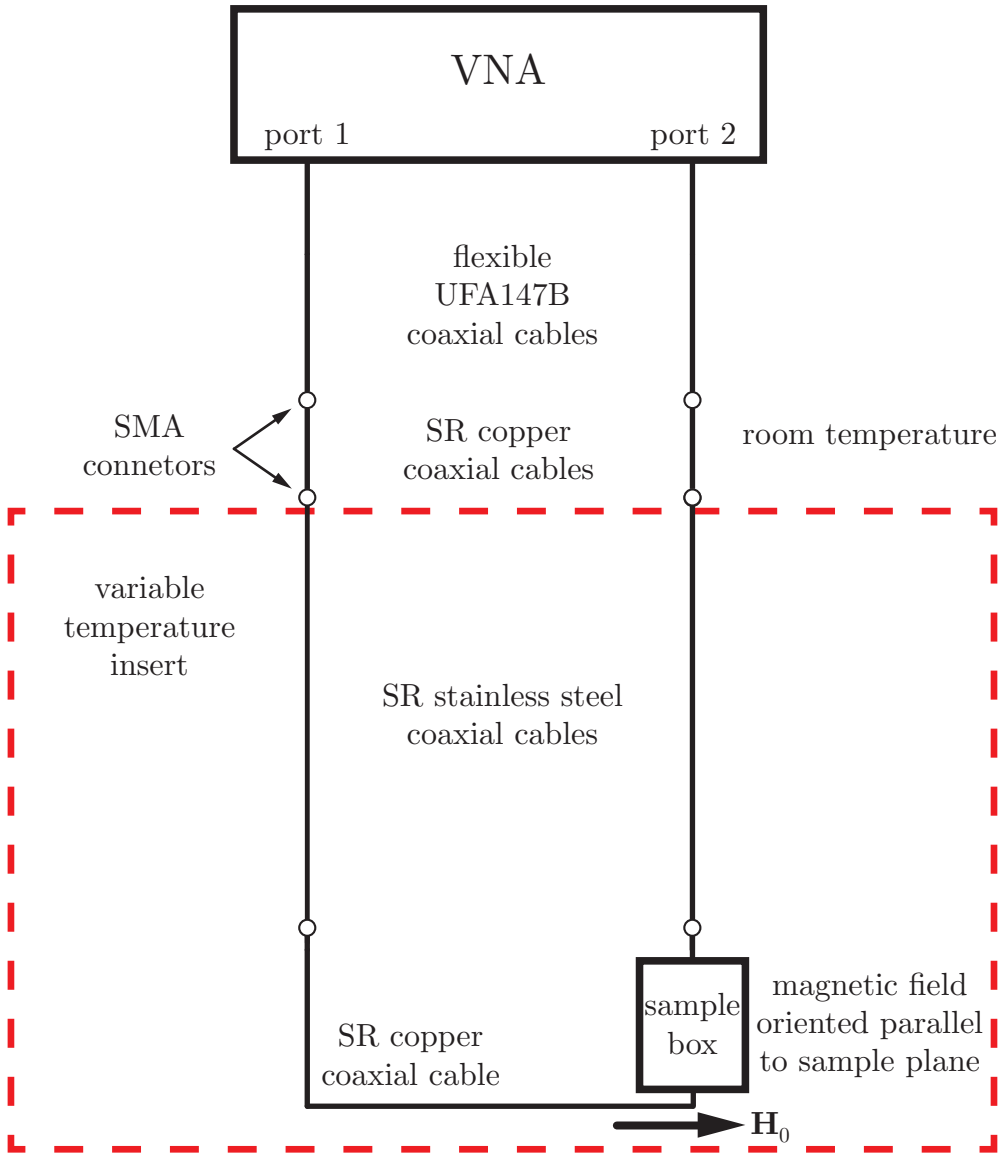

Figure 5.2.: Overview of the RF wiring of the magnet flow cryostat sample holder. The part of the wiring inside the VTI is marked by a red box.

radius than stainless steel cables [54]. The sample box is arranged in the center of two superconducting Helmholtz coils (−7 T to +7 T) and the magnetic field $\mathbf{H}_0$ is applied parallel to the sample plane. The temperature is measured with a calibrated Xernos resistor, which is attached to a copper block, located just above the sample box. Thermal connection between the copper block and the sample box is realized by the SR stainless steel coaxial cables. Via a resistive heater, attached to the same copper block, the temperature of the sample box can be adjusted and stabilized.

5.3. FMR Temperature Series

In the temperature range between 300 K and 4 K several spectra were acquired for the available frequency range of the VNA, resulting in 37 datasets. Figure 5.3 shows nine of them exemplarily with a constant background subtracted (cf. Sec. 4.3), while all of the spectra are shown in appendix A.
In this datasets the resonance can be traced in the frequency-magnetic field space. In the panels 300 K and 240 K the trace is V-shaped and starts at the origin of the graph (∼0 GHz, 0 mT). For better clarity, Fig. 5.4 shows the nine dispersion plots with the resonance dispersion traced by a red line.

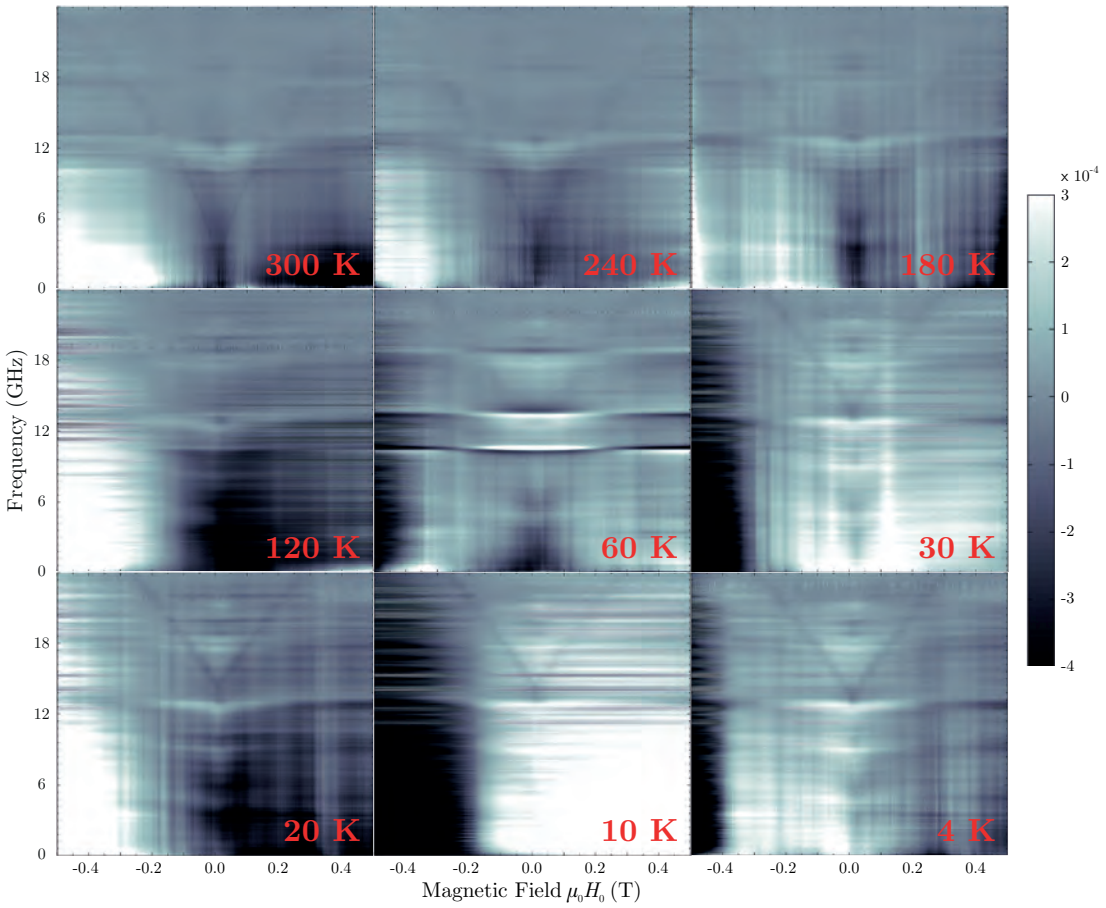

Figure 5.3.: Dispersion plots for a selection of temperatures. (settings: 10 MHz to 24 GHz, 12 MHz steps, microwave power 32 mW, IF bandwidth 100 Hz, −500 mT - +500 mT, 1 mT steps)

Beginning at 300 K, in the first three plots the V-shaped FMR dispersion is distinguishable, starting at zero frequency f, symmetrically around zero magnetic field

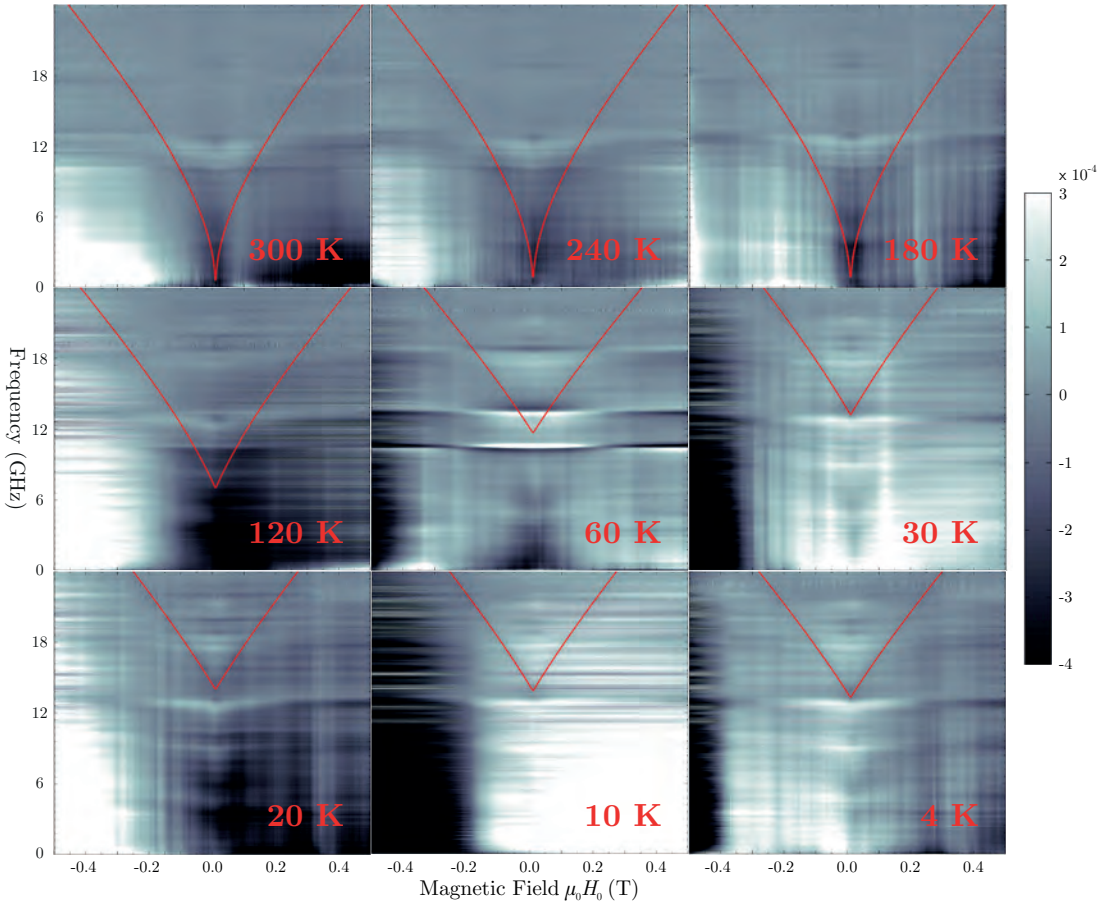

Figure 5.4.: Dispersion plots for a selection of temperatures, with traced FMR dispersion.

$\mu_0 H_0$. The FMR line becomes less defined below 180 K and reappears below 60 K, becoming once again sharply defined. More importantly, the dispersion is shifted to higher frequencies. This effect starts below 130 K and saturated at 20 K, where the the minimal resonance frequency f is approximately 14 GHz.

All measurements exhibit a magnetic field dependent background, which is attributed to temperature fluctuations in the range of 0.1 K, during the experiments. The cut plotted below Figure 5.5 (b) shows the magnitude $\Delta|S_{21}|$ as a function of the magnetic field for 17 GHz, demonstrating the non-linear form of the background. Therefore, the automated fitting procedure, as introduced in Sec. 4.6, was not applicable. In this case, data analysis was performed manually for selected frequencies.

Below 4 K, the millikelvin FMR setup, as introduced in Sec. 4.1, was used for the FMR measurements. To link the experiments performed in the flow cryostat to the measurements in the dilution refrigerator, a spectra at 4.2 K was recorded. Here,

identical experimental parameters were used, except the incident microwave power was reduced to 1 mW, resulting in an effective power on the sample of 100 μW. The dispersion plots of the dilution refrigerator and the flow cryostat measurements are shown in Fig. 5.5 (a) and (b), respectively. The horizontal red line indicates the

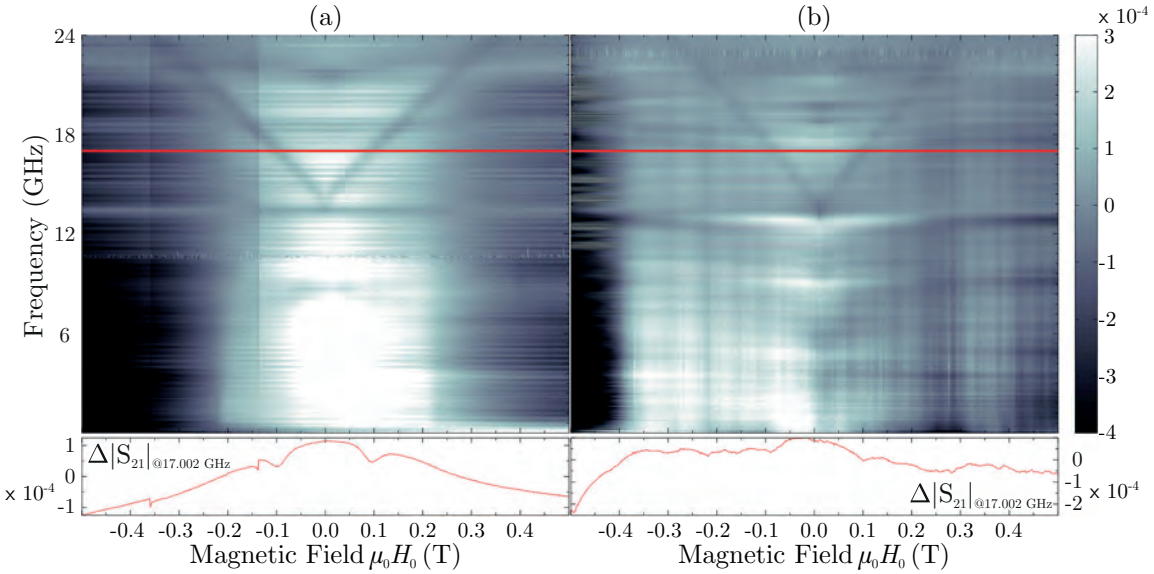

Figure 5.5.: Dispersion plots of the $Ni_{80}Fe_{20}$:Ho_1 sample, showing for both a cut along the magnetic field direction at a frequency of 17 GHz, indicated by the red line. (a) Measurement with the millikelvin FMR setup at 4.2 K with an effective microwave power at the sample of 100 μW. (b) Measurement with the magnet flow cryostat FMR setup at 4 K with a microwave power of 32 mW.

cut at a frequency $f = 17$ GHz, showed in the panels below. The direct comparison of the the two plots, reveals that the background for the millikelvin FMR setup is smoother. This is attributed to the attenuators present at 4 K and the still level as well as the temperature stability during the experiment (4.2 K He bath vs.gas flow) and the configuration of the magnetic field (solenoid for the dilution refrigerator vs. Helmholtz configuration for the flow cryostat).

Beside the reduction in transmission for $|\mu_0 H_0| > 250$ mT, described in Sec. 4.3, figure 5.5 (a) shows also a drop in the transmission within the magnetic field range of around -350 mT to -150 mT over the whole frequency range. This feature appears sporadically in the measurements with the dilution refrigerator at different magnetic fields and differing magnetic field ranges. They show no significance and cannot be reproduced. It is assumed that the VNA is responsible for these features, but their exact origin is unknown. They were not further investigated, as they do not interfere

with the FMR signal.

When comparing the FMR dispersion lines of both measurements a difference in the slope of the FMR resonance can be anticipated. This can be understood and interpreted as a difference in the magnetic field at the sample location. The reason for this can be two-fold: (i) the current-to-field conversion provided by the manufacturer for the specific magnet differs for the actual field or (ii) the sample is not positioned in the center of the field. In both cases, the field has to be independently determined. This is very tedious even at 4 K, because typical Hall probes are not precise enough ($\sim$ 1 %) [65]. One option is to use a well known spin matter like DPPH [18] and perform an electron spin resonance (ESR) experiment for reference. Please note, that the two slopes differ by 20 %, which can be well explained by both points.

An other feature, which is assumed to be an issue with the VNA, is a randomly

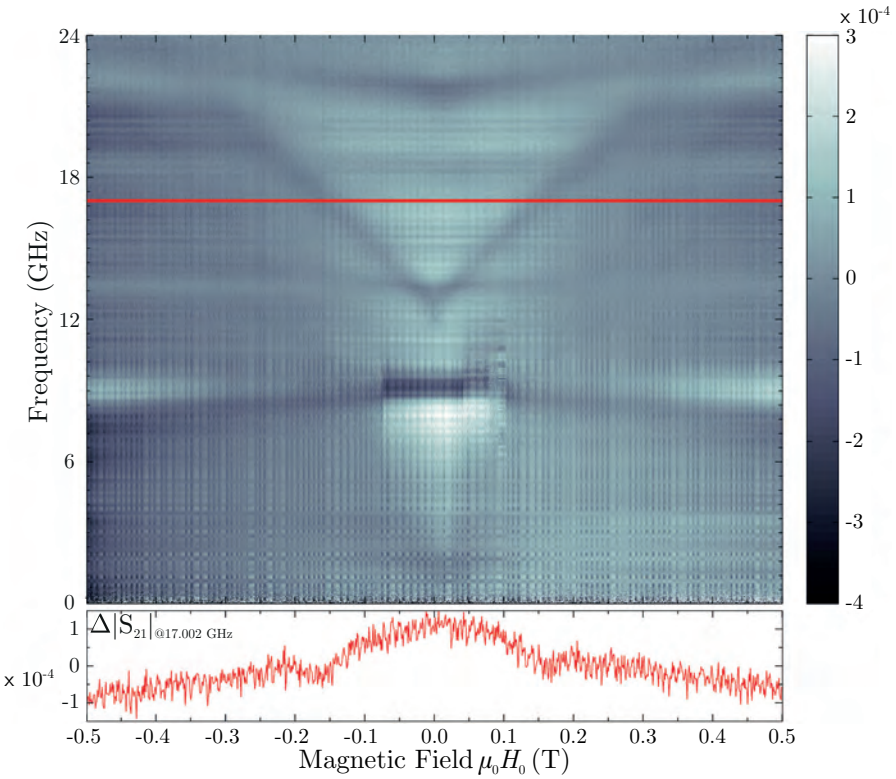

Figure 5.6.: FMR dispersion at about 1 K with an effective microwave power of 1 μW. The red line indicates the cut at a frequency f of 17 GHz, plotted below the dispersion plot. The temperature was not stable during the measurement.

jump or drop in the transmission for single magnetic field points. The feature is not reproducible and if it is present, it appears for a random frequency with varying

transmission jump heights. It can be seen in the dispersion plots shown in Fig. 5.5 (a) at a frequency of approximately 10.5 GHz and in Fig. 5.5 (b) for a frequency of approximately 22.5 GHz. In figure 5.7 this feature is very prominent at approximately 1.5 GHz. Cuts in the magnetic field direction exhibiting these "*glitches*" cannot be evaluated. This feature is only affecting a small portion of the measurement, it does not hamper the line width analysis.

Next, a measurement was conducted at approximately 1 K with an effective microwave power at the sample of 1 μW (cf. Fig. 5.6). At this temperature it is difficult to operate a dilution refrigerator with a constant cooling power. It is the temperature region, where the dilution process in the mixing chamber starts (cf. Sec. 3.1). The dilution refrigerator can be operated such, that the dilution process is not continuous, but periodic. Consequently, the temperature shows a periodicity, too. In the dispersion plot of Fig. 5.6 this is reflected by the vertical lines. The cut, also given

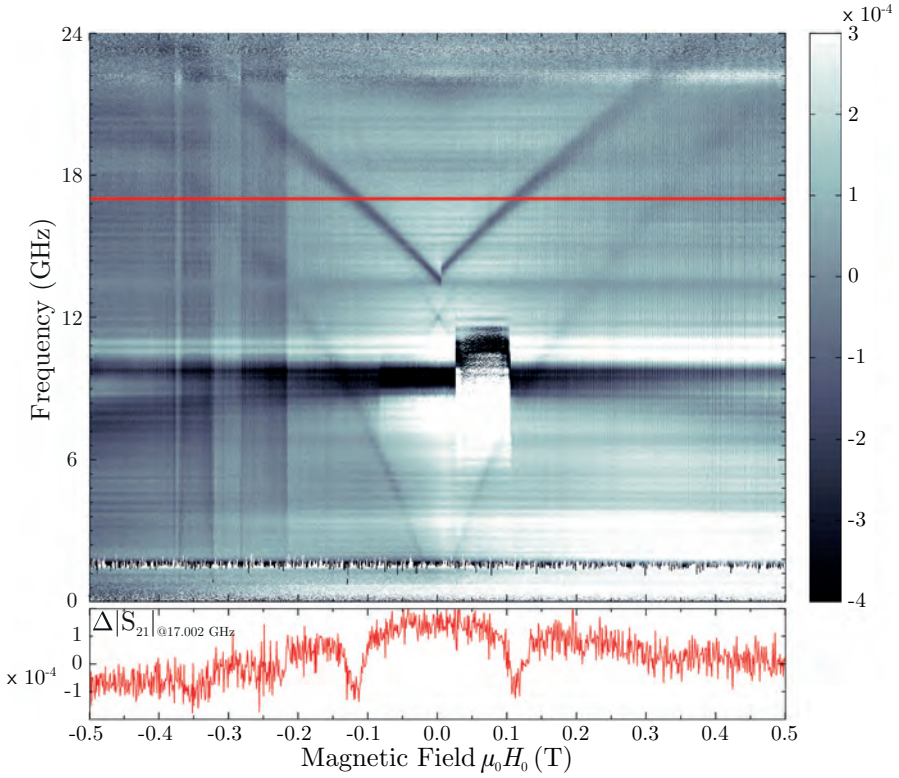

Figure 5.7.: Dispersion plot at 50 mK, an effective microwave power of 100 pW and with the magnetic field $\mu_0 H_0$ swept from -500 mT to $+500$ mT. The plot underneath shows a cut at a frequency f of 17 GHz, marked by a red line in the dispersion plot.

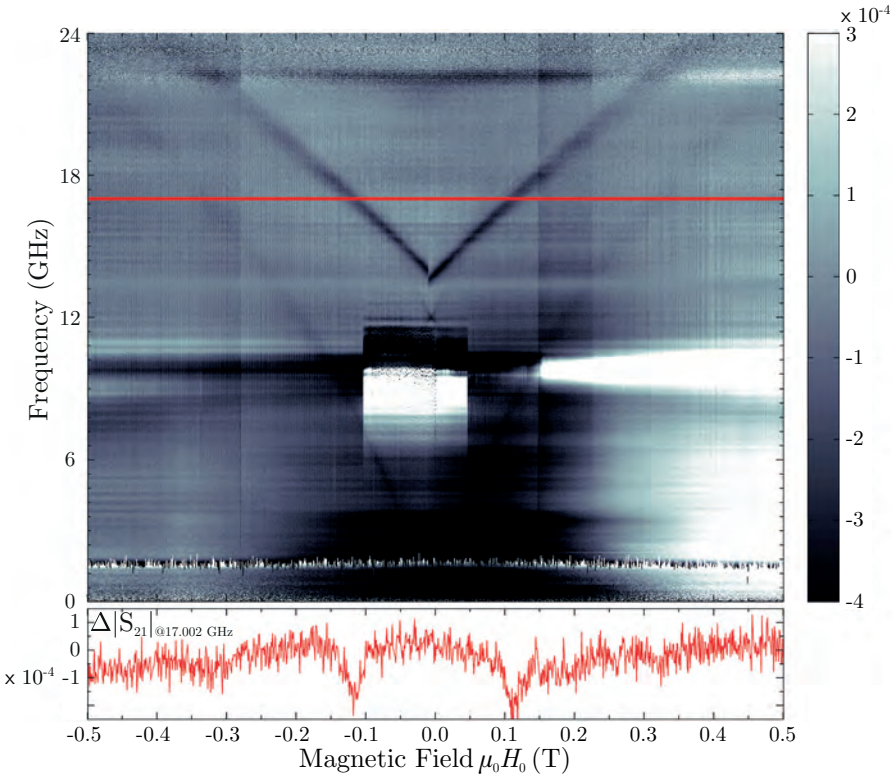

Figure 5.8.: Dispersion plot at 50 mK with an effective microwave power of 100 pW. The magnetic field $\mu_0 H_0$ is swept from +500 mT to −500 mT. Underneath the dispersion plot a cut at a frequency f of 17 GHz is shown.

in Fig. 5.6, at a frequency of 17 GHz has a high noise level, due to the temperature instability. A line width analysis may not be done, but one can still identify the FMR dispersion. It shows no significant change to the measurement at 4.2 K.

At 50 mK a measurement was conducted, utilizing additional 30 dB attenuator, a 28 dB broadband amplifier and the direct receiver access of the VNA (cf. Sec. 4.1). An effective microwave power of 100 pW was applied to the sample. The resulting dispersion plot with a beneath displayed cut along the magnetic field direction at a frequency of 17 GHz, is shown in Fig. 5.7. The plot displays features described in Cha. 4, in addition to two new features.

One is seen in the prominent absorption line, running horizontal between approximately 9 and 10 GHz. In the magnetic field range of about +25 mT to +100 mT the absorption line is shifted discontinuous by approximately 1 GHz to higher frequencies. This feature can be reproduced and shows a hysteretic behavior. Figure 5.8 displays the same measurement as Fig. 5.7, except that the magnetic field $\mu_0 H_0$ is swept from

+500 mT to −500 mT. The absorption line is located in the same frequency range, but the line shift is in a magnetic field range of about −100 mT to +50 mT. The origin of this absorption line and its shift, is unknown. Further investigations are required to discern its source. The sample box may be ruled out as the originator of this absorption line (cf. Sec. 4.7). It is assumed, that the absorption line is caused by the $Ni_{80}Fe_{20}$:Ho_1 sample, but the responsible effect is yet unknown. Since the feature not interferes with the FMR, its investigation shall be postponed at this point.
At low temperatures a hysteretic dependence of the ferromagnetic resonance becomes visible, manifesting in a discontinuity of the FMR at low field. At the magnetic field of 8 mT (Fig. 5.7) or −13 mT (Fig. 5.8), the resonance shifts abruptly by approximately 400 MHz, indicating the reorientation of the magnetization. This is corroborated by the literature value of the coercive field $\mu_0 H_0$ of 10 mT at room temperature [9].
This feature, although located at low fields, is not exactly symmetric about 0 mT, due to flux trapping in the superconducting magnet.

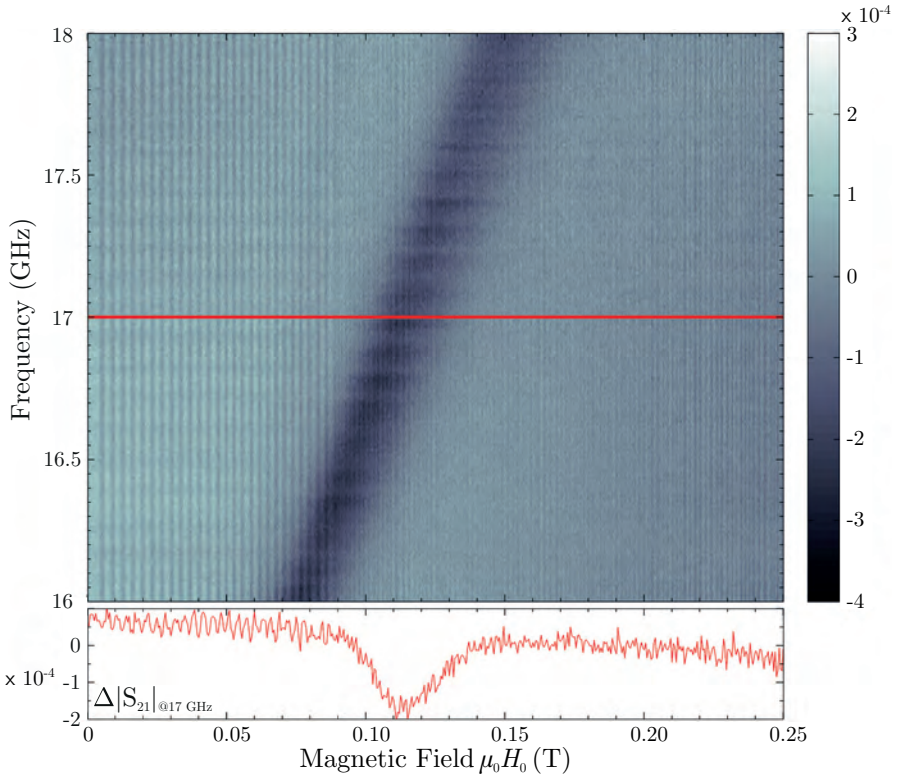

Figure 5.9.: Dispersion plot at 50 mK with a cut at a frequency f of 17 GHz (red line). The effective microwave power was 100 pW. The measured transmission was averaged ten times.

The data presented in Fig. 5.7 or 5.8 show only a poor signal to noise level, due to the low power used for its recording, preventing accidental heating of the doped Permalloy film. Therefore, for the line width analysis broadband magnetic field scans were recorded with appropriate averaging, as indicated in Fig. 5.9. As visible from the cut presented in the lower panel, this data quality is sufficient for an automated analysis, as outlined in Sec. 4.6.

5.4. Data Discussion

5.4.1. Temperature Dependent Line Width

Woltersdorf *et al* [8], reports measurements performed with different RE dopant and doping grades. The here investigated $Ni_{80}Fe_{20}$:Ho_1 was not reported in the publication, but instead on an identical sample, doped with two atomic percent of Holmium. Since, the Gilbert damping parameter α, and therefore the frequency dependent line width $\mu_0 \Delta H(f)$, exhibit a linear increase with increasing doping concentration (cf. Fig. 5.10), the two datasets can still be compared. From Fig. 5.10 an α-parameter of 0.017 can be extracted for Permalloy doped with one atomic percent of Ho, at

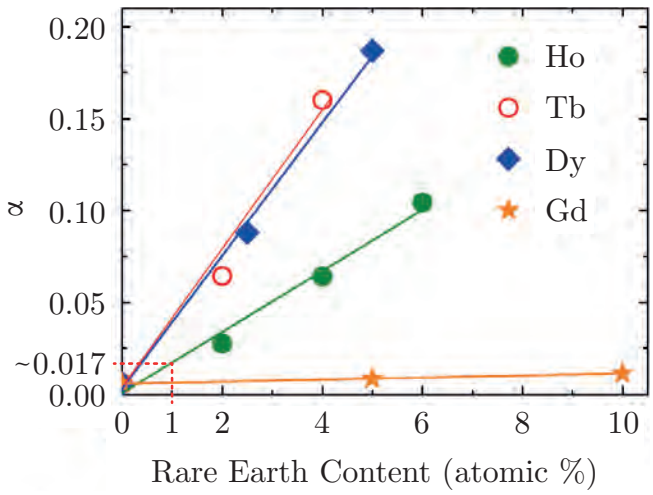

Figure 5.10.: Gilbert damping parameter α as a function of the RE concentration for different dopant. α for a Ho doping of one atomic percent, is marked by a red dashed line.

room temperature. This value lies well within the tolerance of $\alpha = 0.0182 \pm 0.0017$, determined from the flow cryostat experiment at 300 K.

The published line width data was obtained by using Lock-in detection, resulting in a differentiated absorption spectrum, which is a factor of $\sqrt{3}$ smaller than the line width determined in a VNA-FMR absorption spectrum [49]. The data measured in this Chapter are displayed in form of a ΔH_{PP} (lock-in peak-to-peak line width) for easy comparison

$$\Delta H_{\mathrm{PP}} = \frac{\Delta H}{\sqrt{3}}. \tag{5.1}$$

Figure 5.11 shows the temperature dependent line width $\mu_0 \Delta H_{\mathrm{PP}}$ for different RE dopant and doping concentrations in range of 350 K to 100 K. The data was obtained from FMR spectra at a frequency $f = 10$ GHz. For the discussion, the dataset of $Ni_{80}Fe_{20}$:Ho_2 (green dots) shall be of interest. The line width at room temperature and 100 K were marked by red dashed lines and their values were added to the plot. For room temperature $\mu_0 \Delta H_{\mathrm{PP}}$ was determined to 11 mT and for 100 K to 25 mT. By assuming a linear dependency of the line width as a function of the Ho concentration a $\mu_0 \Delta H_{\mathrm{PP}}$ of 5.5 mT (300 K) and 12.5 mT (100 K) is expected for $Ni_{80}Fe_{20}$:Ho_1,

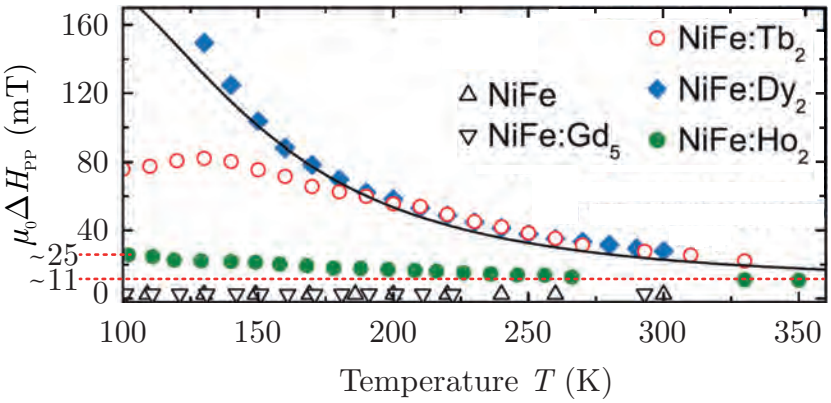

Figure 5.11.: The line width $\mu_0 \Delta H_{\mathrm{PP}}$ for various RE dopants in Permalloy as a function of temperature T. The measurements were carried out with a microwave frequency $f = 10$ GHz and the magnetic field was in the plane of the thin film. Note, that the data for the Dy dopant was multiplied by a factor of $4/5$ for better comparison. The two red dashed lines were added to mark the line width of $Ni_{80}Fe_{20}$:Ho_2 for 100 K and room temperature.

For comparison, Fig. 5.12 shows the line width data of $Ni_{80}Fe_{20}$:Ho_1 measured during the course of this thesis, in the temperature range of 300 K to 50 mK for various microwave frequencies. Starting around 12 mT at 300 K, the line width increases with decreasing temperature, reaching a maximum of approximately 41 mT at 100 K. For temperatures below 100 K, the line width decreases, until it saturates at 11 mT for

$T < 20$ K. Figure 5.13 zooms into the temperature range of 20 K to 50 mK showing, that the line width remains unchanged down to 50 mK, considering the increase at 6 K as an outlier.

Comparing both datasets, shows a distinct difference. The line width extracted from Fig. 5.11 is smaller, than the line width data displayed in Fig. 5.12. This can be

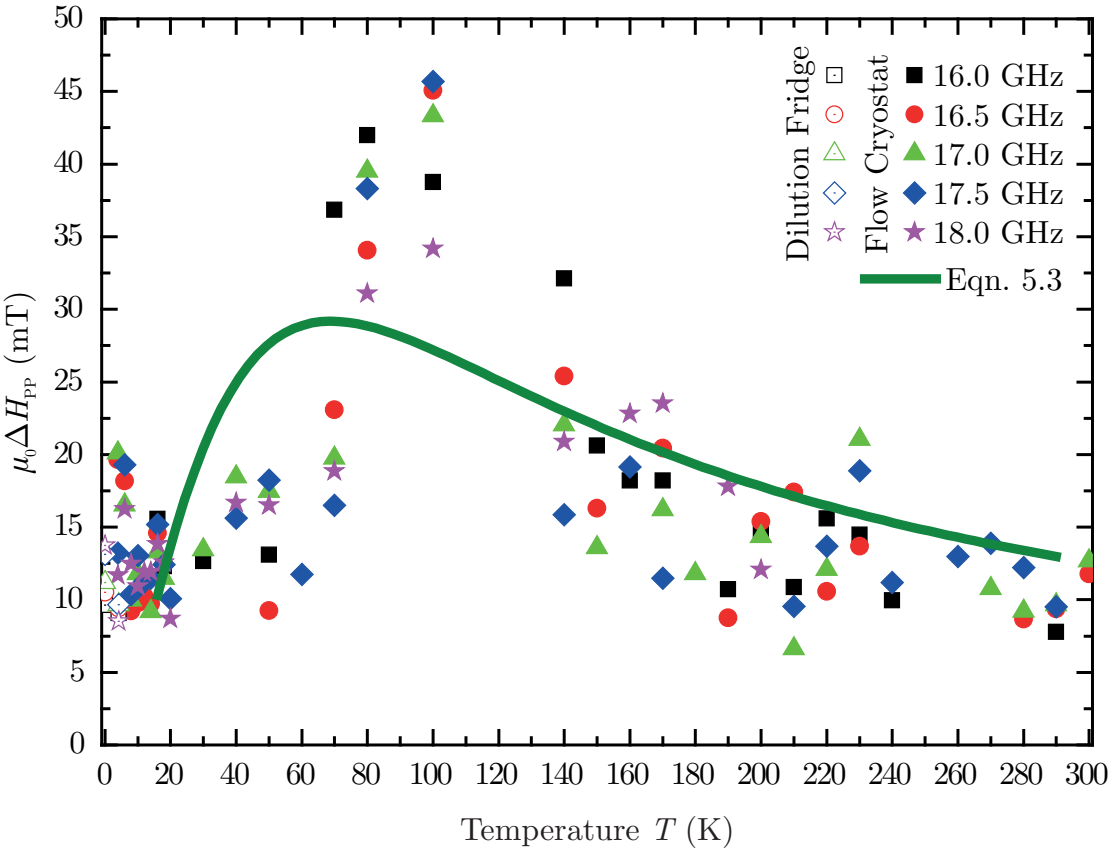

Figure 5.12.: The line width $\mu_0\Delta H_{PP}$ as a function of temperature T for $Ni_{80}Fe_{20}$:Ho_1, determined for different frequencies. Filled symbols represent data from the flow cryostat setup and the open symbols data from the millikelvin FMR setup.

attributed to the higher frequencies, used for the determination of the line width in this thesis. Please note, that this higher frequency was chosen, because the FMR shifts to higher frequencies at low temperatures (cf. Fig. 5.3).

The temperature dependency of the line width of the Holmium doped Permalloy can be understood by the slowly-relaxing-impurity mechanism [5]. In effect, this theory describes the relaxation process of Yittrium Iron garnet (YIG) with RE impurities, and most generally for ferromagnetic insulators. But the principles of this theory, can

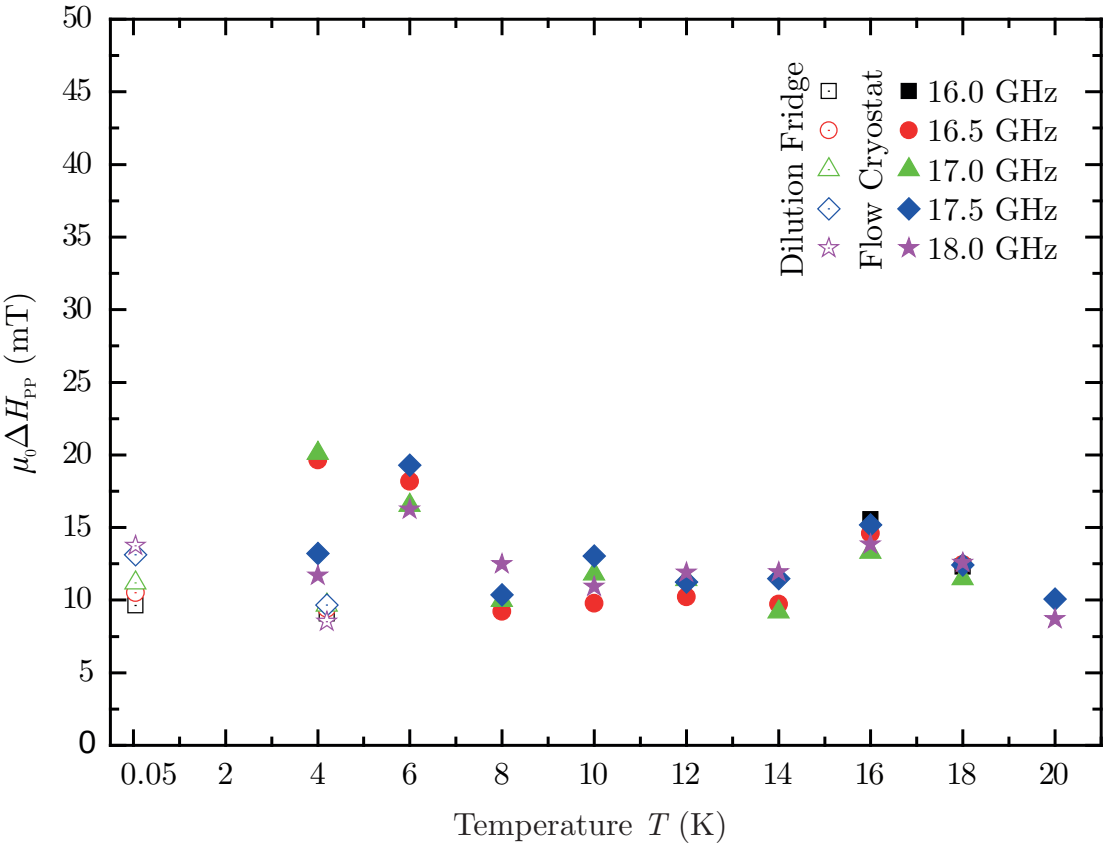

Figure 5.13.: Figure 5.12, only showing data in the temperature range of 50 mK to 20 K.

be transfered to the case of Permalloy.

This mechanism allows to transfer excitation energy, from FMR, directly to the lattice, instead of involving degenerate or thermal spin waves (cf. Sec. 2.3). For the case of YIG, the Fe^{3+} ions form a magnetic sublattices A, with spins $\mathbf{S}_A$. The magnetic ions are tightly intracoupled by exchange. By doping, single ions are replaced by a RE ion, with a spin $\mathbf{S}_{RE}$. The sublattice A is indirectly coupled to the phonon lattice by the exchange coupling between the RE ions and the sublattice A, and the coupling of the RE ions to the lattice. An indirect approach has a greater effect on the sublattice A, than the direct coupling between the Fe^{3+} ions and the lattice, because Fe^{3+} has no orbital angular momentum [66].

The RE spins $\mathbf{S}_{RE}$ are exchange coupled to only a few of the spins $\mathbf{S}_A$ of the sublattice A, in fact, the RE spins are coupled to the spin waves due to the strongly exchange coupled Fe^{3+} ions. Now, looking at the energy level of a RE spin, it exhibits a Zeeman split by the magnetization of the sublattices A. When the system is excited,

as in the case of FMR, the magnetization of A precesses with a frequency ω_{res}. The precessing magnetization, which causes the splitting of the energy levels of the RE spins, modulates this splitting at a frequency of ω_{res}. The modulation changes the thermal equilibrium population of the energy levels. For this two level system a relaxation time $1/\tau_{\mathrm{RE}}$ can be defined, as the time for reaching thermal equilibrium. To reach the modulation dependent thermal equilibrium, the energy levels change their populations, and by doing so, transferring energy to the lattice. The transfered energy originates from the excited spins $\mathbf{S}_A$ of the Fe^{3+} ions, thus accelerating the relaxation of the spins $\mathbf{S}_A$, leading to a line width broadening.
The line width $\mu_0\Delta H$ is related to the relaxation time can be described $1/\tau_{\mathrm{RE}}$ by [5]

$$\mu_0\Delta H \propto \frac{\omega_{\mathrm{res}}\tau_{\mathrm{RE}}}{1+(\omega_{\mathrm{res}}\tau_{\mathrm{RE}})^2}. \tag{5.2}$$

exhibiting a maximum at $\omega_{\mathrm{res}}\tau_{\mathrm{RE}} = 1$. Since the relaxation time $1/\tau_{\mathrm{RE}}$ increases with decreasing temperature [67], the line width shape can be understood. Taking a explicit temperature dependency and the modulation of the two energy levels of the RE spins, results in [8], [68]:

$$\mu_0\Delta H = A_{\mathrm{ex}}\frac{C_{\mathrm{RE}}}{6M_{\mathrm{S}}k_{\mathrm{B}}T}\frac{\omega_{\mathrm{res}}\tau_{\mathrm{RE}}(T)}{1+(\omega_{\mathrm{res}}\tau_{\mathrm{RE}}(T))^2}\mathrm{sech}\left(\frac{\delta}{2k_{\mathrm{B}}T}\right)^2, \tag{5.3}$$

with

$$\tau_{\mathrm{RE}}(T) = \frac{\tau_{\mathrm{RE}}(0)}{\coth(\delta/2k_{\mathrm{B}}T)}. \tag{5.4}$$

C_{RE} is the RE concentration, M_{S} is the saturation magnetization of the sublattice A and δ gives the energy level splitting of the RE ion. A_{ex} represents the anisotropic exchange between the sublattice A and the RE ion, caused by the precessing magnetization A. The sech-function introduces a strong temperature dependency, exhibited by the population of the modulated energy levels of the spins $\mathbf{S}_A$.
The green solid line in figure 5.12 shows the result obtained by (5.3), using a level splitting $\delta = 0.755$ meV, a zero temperature relaxation time of $\tau_{\mathrm{RE}}(0) = 151$ ps and an anisotropic exchange of $A_{\mathrm{ex}} = 2.03 \times 10^{-13}$ J^2/m^3. For temperatures above 140 K the experimental data are in good agreement with the theoretical model. The experimental data exhibit a greater increase in line width, with the maximum being 25 % larger than the theoretical. This may be attributed to additional line broadening effects, like eddy currents. Since this theory is supposed to describe the line broad-

ening for ferromagnetic insulators, effects like eddy currents are not accounted for. Furthermore, theory predicts a zero line width for zero temperature, which was not observed by the experiment. Here, the line width saturated for low temperatures on a value similar to the one obtained for 300 K. This leads to the assumption, that for low temperatures the relaxation is not governed by the RE impurities, but by Permalloy itself or other damping effects like eddy currents. For this further investigations need to be carried out, such as varying the RE concentration and RE element of the Permalloy, to further ascertain a dependency of the line width on the RE doping or change to an insulating ferromagnetic material system to expand the experimental data into the millikelvin regime for a further confirmation of the theory.

5.4.2. Temperature Dependent FMR Dispersion Shift

Apart from the expected temperature dependent change in the FMR absorption line width $\mu_0\Delta H$, the FMR dispersion is shifted to higher frequencies (cf. Fig. 5.3 and 5.4). To verify, whether this is an intrinsic effect of Permalloy or is caused by the rare earth dopant Holmium, pure Permalloy was measured for reference. This thin film sample was prepared in identical manner to the preversionaly examined, differing only in its thickness of 10 nm.
Again, the measurements are performed, using the magnet flow cryostat FMR setup, in the same manner as outlined in Sec. 5.2, replacing the flexible UFA147B by ultra low dampening UFA210B coaxial cables. The chosen temperatures were 300 K, 100 K and 4 K. Figure 5.14 shows the resulting dispersion plots for the pure Permalloy. It can be observed clearly, that there is no increase of the FMR frequency with decreasing temperature. Therefore, the shift of the dispersion line to higher frequencies is attributed to the presence of the Holmium atoms.
It shall be noted, that the transmission $\Delta|S_{21}|$ is higher by almost a factor of ten, than the transmission of the Ho doped Permalloy measurements. The increase in transmission can be attributed to the lower attenuation of the flexible UFA210B coaxial cables resulting in a higher power at the sample.
The theory of the slow relaxing impurity model also predicts a shift of the FMR, with the same temperature dependency as (5.3) and with a similar magnitude [68], [69]. Here, the shift is caused due to the temperature dependent repopulation of the RE energy levels. But, the in the experiments observed shift clearly is not reducing

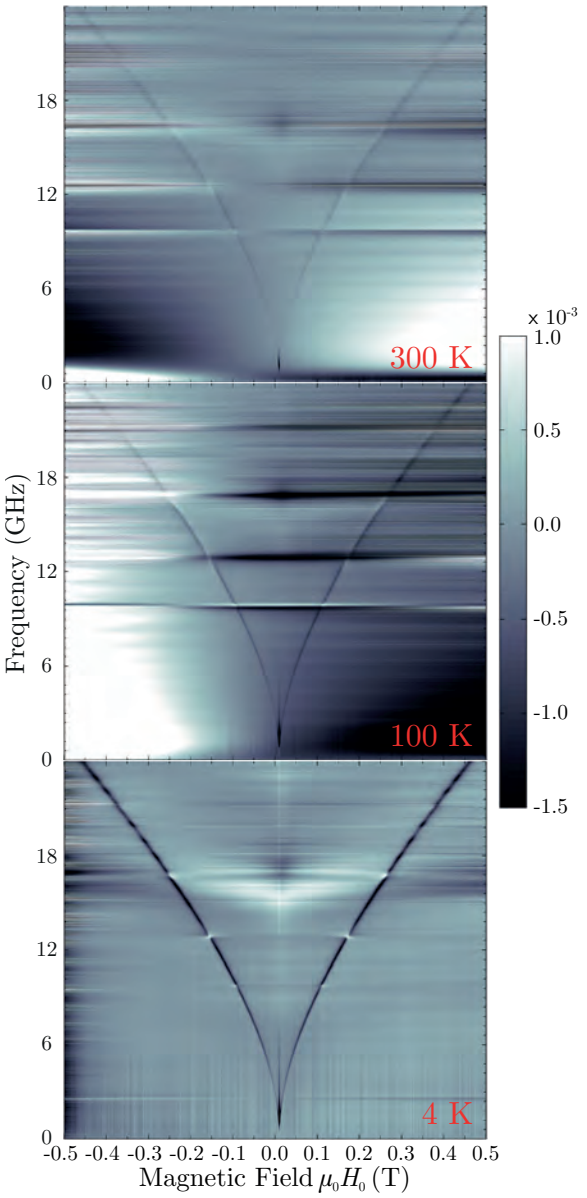

Figure 5.14.: Dispersion plots of a pure Permalloy thin film at temperatures of 300 K, 100 K and 4 K.

for low temperatures and its magnitude is much greater than the line width increase. Therefore, it is assumed, that the shift is dominated by another effect.

Looking at the temperature dependent magnetic moment of Holmium, the origin of the offset can be explained.

B. L. Rhodes et al measured the magnetic moment of Holmium, over a temperature range of 4.2 K to 300 K [70]. In Figure 5.15 the magnetic moment m of Holmium is plotted against temperature T. Three different curves are displayed, obtained at different constant applied magnetic fields.

For a temperature of about 133 K, the magnetic moment has a sharp maximum. This indicates a transition to an antiferromagnetic state and it is also the temperature range, where the FMR signal of the $Ni_{80}Fe_{20}$:Ho_1 becomes weaker. The antiferromagnetic ordering may be responsible for the weakening of the FMR signal, if one considers the very high effective magnetic moment of Ho of 10.9 μ_B [70]. The magnetic moment of Ho decreases for temperatures below the Néel temperature of 133 K. At a temperature of 115 K, the magnetic moment starts to rise again. Here, the magnetic moments undergoes a transition from an antiferromagnetic ordering over into a ferromagnetic ordering [70]. Simultaneously, around this temperature the FMR dispersion line begins to shift to higher frequencies (cf. A). The magnetic moment of Ho rises until it

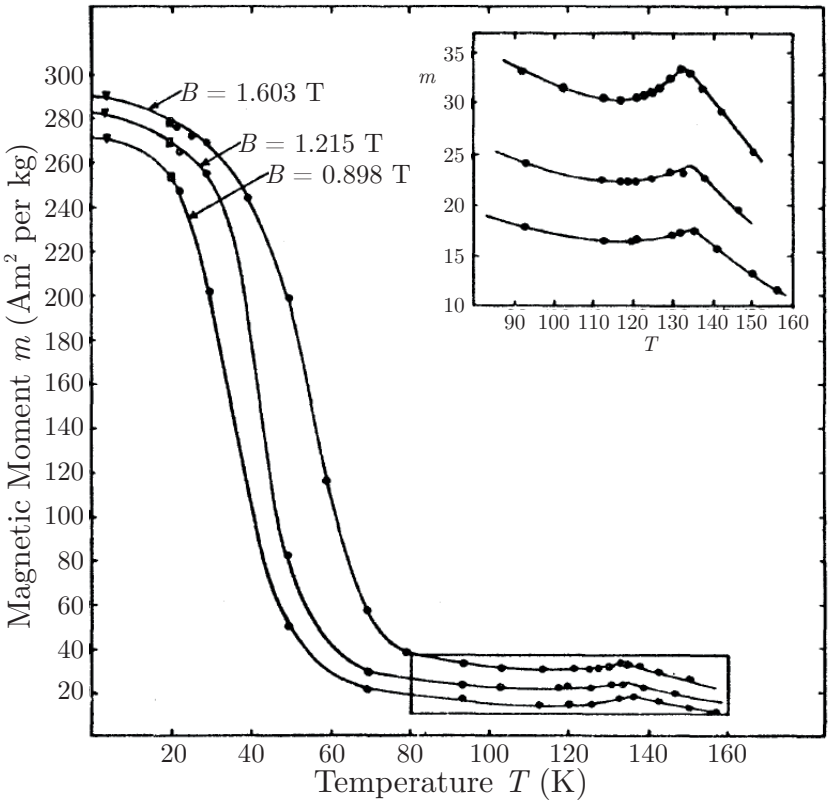

Figure 5.15.: Magnetic moment m of pure Holmium as a function of temperature T for three different constant applied magnetic fields. The inset shows a magnification of the framed area of the plot [70].

saturates at around 20 K [70], where the offset to the FMR dispersion also reaches its maximum. The temperature dependent course of the magnetic moment of Holmium fits the temperature dependent shift of the FMR dispersion of the $Ni_{80}Fe_{20}$:Ho_1 sample very well. As the magnetic moments of Ho begin to order ferromagnetically, they create an effective magnetization field, which introduces an offset M_{Ho} to the static magnetic field H_{eff}. From the FMR experiment performed on $Ni_{80}Fe_{20}$:Ho_1 at 50 mK (cf. Fig. 5.7) the offset field induced frequency shift is determined to $f_{\mathrm{Ho}} \approx 14$ GHz. The shift of the resonance condition can basically be described by

$$\omega'_{\mathrm{res}} = \omega_{\mathrm{res}}(H_{\mathrm{eff}} + M_{\mathrm{Ho}}) = \gamma\mu_0 H_{\mathrm{eff}} + \gamma\mu_0 M_{\mathrm{Ho}}. \tag{5.5}$$

ω_{res} is given by (2.17), when to the Zeeman term of (2.19) the magnetization of Ho M_{Ho} is introduced.

$$F_{\mathrm{Zeeman}} = \mu_0 M_{\mathrm{Py}}(H_0 + M_{\mathrm{Ho}}), \tag{5.6}$$

where M_{Py} is the magnetization of Permalloy.
To quantitatively estimate the effect attributed to the Ho dopants present in Permalloy the magnetization curve displayed in Fig. 5.15 is used. The sample volume V of the experiment of Ref. [70] is 10^{-8} m^3, where Ho has a density $\rho = 8795$ $^{\mathrm{kg}}/_{\mathrm{m}^3}$ [71], resulting in a mass $m_{\mathrm{sample}} = 8.795 \times 10^{-5}$ kg. Hereby, the magnetization of pure Ho can be calculated:

$$M_{\mathrm{Ho}} = \frac{m_{\mathrm{Ho}}}{V}\frac{m_{\mathrm{sample}}}{m} = \frac{280\mathrm{Am}^2}{10^{-8}\mathrm{m}^3}\frac{8.795 \times 10^{-5}\mathrm{kg}}{1\mathrm{kg}} = 2462.6\frac{\mathrm{kA}}{\mathrm{m}}.$$

In the case of the Ho doped Permalloy thin film discussed in this thesis the content of Ho is 1 at%. For a first estimate, it is assumed that the magnetization originating from the Ho dopants is completely decoupled from the magnetic properties of the Permalloy. Therefore, for the magnetic induction induced in the Permalloy only by the Ho dopants $\mu_0 M_{\mathrm{Ho}} \cdot 1\mathrm{at}\% = 31$ mT is obtained. With (5.5) this transfers to a frequency shift of 0.869 GHz.
Compared to the observed shift of 14 GHz this value is about a factor of 16 smaller than expected. Although the experimentally observed effect is underestimated, the overall effect of the increase in resonance frequency qualitatively accounts for the temperature dependent observation. The result shows, that the exchange between Permalloy and the Ho impurities need to be taken into account. Assuming, that the Ho dopants polarize their surroundings, thus effectively increasing its prior assumed independent magnetization, explaining the magnitude of the observed shift.

Plus, here's the mini cherry on top of the regular cherry on top of the sundae of awesomeness that is my (..) [diploma thesis, C.Z.].

Barney Stinson

Chapter 6.

Microwave Resonator Experiments

The observation of the interaction of unintentional box modes with the Cobalt specimen (cf. Sec. 4.7) triggered experiments towards strong coupling in microwave resonator-ferromagnet hybrid systems, presented in this Chapter. Here, superconducting (SC) microwave resonators provide a defined photonic cavity, in which a ferromagnetic sample was placed. If the ferromagnetic resonance and the microwave resonator are driven simultaneously, a coupling between cavity modes and FMR modes is observed.
Combining SC high quality microwave resonators with applied magnetic fields in the hundreds of millitesla range is contradictory and therefore the Chapter begins with a investigation of the influence of the magnetic field on the SC microwave resonator parameters. Section 6.2 presents and discusses the measurements of the interaction of Gallium (GA) doped Yttrium Iron Garnet (YIG) and the photon cavity.

6.1. Characterization of Superconducting Coplanar Microwave Resonators

For a quantitative description of the coupling between two resonances, their resonance frequencies and resonance line width have to be characterized, at best individually. A common set of parameters to characterize a resonator, are its resonance frequency and Q-factor (cf. Sec. 2.6). During the experiments, the SC resonators are exposed to a static magnetic field $\mu_0\mathbf{H}_0$, used to drive FMR. The superconductivity will be compromised by the magnetic field and therefore, the resonator properties are changed with varying magnetic field.
To get an impression, how a static magnetic field influences the microwave resonator

properties, measurements are conducted with different resonator designs. Additionally, different film thicknesses are tested (cf. setup in Sec. 3.4.2). The microwave resonator chips are mounted in a sample box, as described in Sec. 3.4.3. The characterization of the resonators is performed in the flow cryostat setup, introduced in Sec. 5.2. During these measurements the setup did not include a heater close to the sample box. Therefore, the temperature stated is not actively controlled and slightly differs for each measurement.
Figure 6.1 shows the layout of a multi-resonator structure, which has the advantage, that a magnetically loaded resonator can be compared with an unloaded resonator. In particular, Fig. 6.1 shows four resonators for transmission experiments with different lengths resulting in the resonance frequencies f_1, f_2, f_3 and f_4.

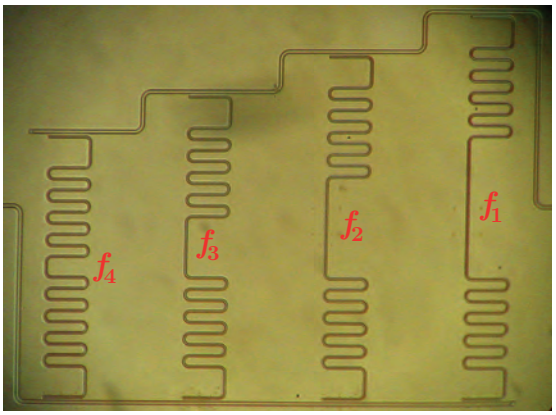

Figure 6.1.: Multi-resonator with each resonator denoted by its resonance frequency f_1, f_2, f_3 and f_4

The Nb thickness of the resonator structure is varied to optimize for high quality factors Q at the expected magnetic resonance field of the FMR. Figure 6.2 shows the dispersion plot of the magnitude $|S_{21}|$ for a 100 nm thick Nb film at a temperature of 2.6 K. Unfortunately, the resonator with the frequency f_3 was damaged, hence could not be characterized. To the left of the dispersion plot, a cut in the frequency direction at zero magnetic field is shown.
As the magnetic field increases, the resonance frequency is shifted to lower frequencies and the amplitude of the resonance is reduced, because the magnetic field reduces the RF conductivity of the superconductor, increasing the inductance L of the resonator, and thus reducing the resonance frequency (cf. Eqn. 2.35).
The resonances observed in the cuts along the frequency direction are fitted with

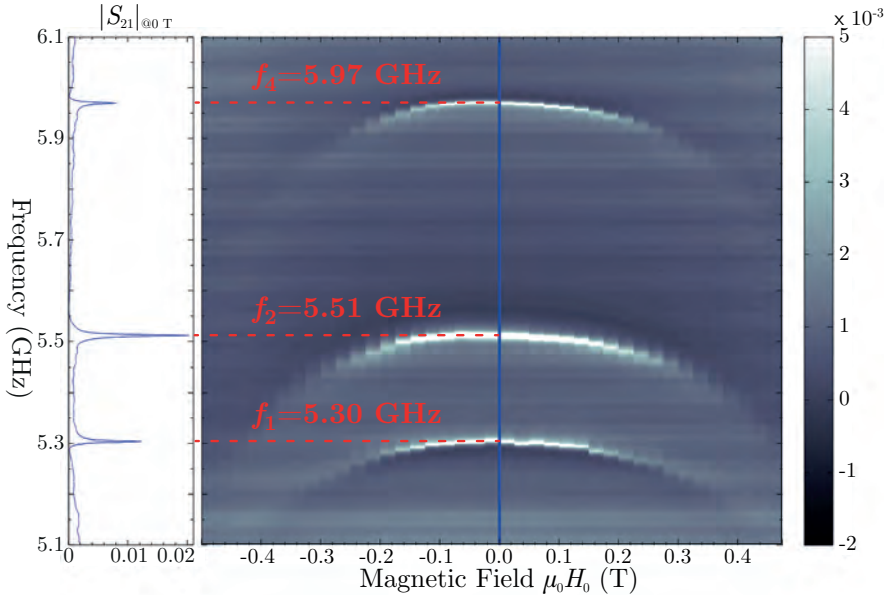

Figure 6.2.: Dispersion plot showing three resonances (f_1, f_2 and f_4) of the 100 nm thick Nb resonator structure at 2.6 K. The blue line indicates a cut in the frequency direction at zero magnetic field, plotted to the left. The dashed red line is a guide to the eye, connecting the resonance location of both plots. (experimental parameters: 5.1 GHz to 6.1 GHz, 100 kHz stepsize, microwave power 10 μW, IF bandwidth 100 Hz, -500 mT to $+475$ mT, 25 mT stepsize)

MATLAB for all magnetic field points with a Lorentzian function, resulting in the resonance frequencies and line width. Hereby, the Q-factor is obtained as a function of the magnetic field. Figure 6.3 shows the Q-factor extracted from the dataset, plotted in Fig. 6.2. Starting from Q-factors between 2000 and 3500 the Q-factor is significantly reduced for higher magnetic fields. Please note, that the Q-factor or line width relevant for the experiment has to be obtained at the magnetic field corresponding to the FMR condition, which is in case of Ga doped YIG $\pm$170 mT for 6 GHz. For the data shown in Fig. 6.2 the cavity line width ranges from 15 MHz to 30 MHz, at a magnetic field of $\pm$175 mT. As these values are in the first place not encouraging one has to take into account, that the experiment with Ga doped YIG is performed at millikelvin temperatures, improving these values, as can be seen in Fig. 6.8 and Fig. 6.10. Maxima in the Q-factor, observed for $\mu_0 H_0 \geq 300$ mT, were caused by a failure of the fit. At these fields the resonance amplitude is comparable to the background, making the fit unreliable.

The second multi-resonator chip had a Nb film thickness of 200 nm, resulting in the

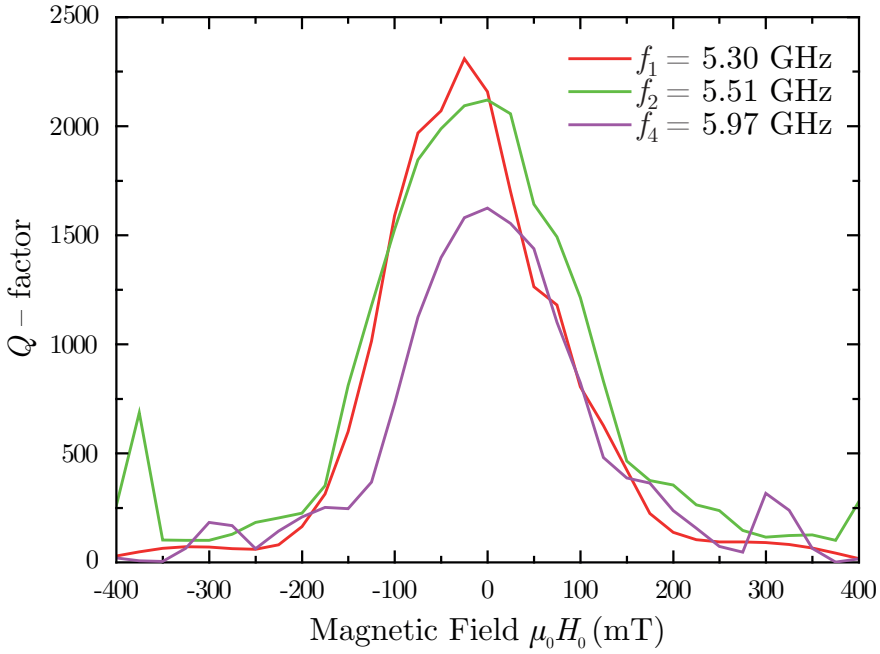

Figure 6.3.: Comparison of the resonators Q-factors, plotted for a magnetic field range of -400 mT to $+400$ mT.

dispersion plot shown in Fig. 6.4 and the magnetic field dependent Q-factor shown in Fig. 6.5 for a temperature of 2.3 K. Although at low magnetic fields the 200 nm thin Nb film performs better than the 100 nm thick film, the Q-factors at ± 175 mT are worse.

Finally a 300 nm thick Nb multi-resonator chip was investigated, showing the results in the figures 6.6 and 6.7. This resonator performs best of the three examined. It exhibits the highest Q-factors for low magnetic fields as well as at ± 175 mT, apart from the resonator with frequency f_4, which performs worse than the other three.

The characterization shows the best results for the multi-resonator chip with a Nb film thickness of 300 nm. It exhibits a high zero magnetic field quality factor as well as a good Q-factor for the magnetic fields needed for FMR at the resonators resonance frequencies. Although, the 300 nm thick resonator showed the best results, but for the strong coupling experiments the 100 nm thick resonator was used, because at this time only the 100 nm thick resonator was available.

The Q-factors differ significantly for the resonator thicknesses. A certain tolerance in the production process, and a varying quality of the used Niobium are responsible for the differing Q-factors.

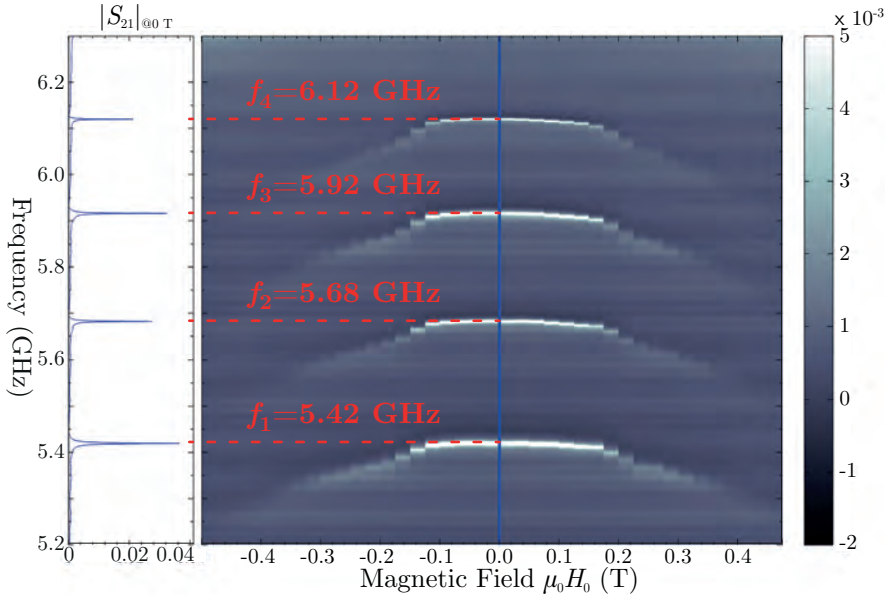

Figure 6.4.: Dispersion plot of the 200 nm thick Nb multi-resonator chip at 2.3 K. A cut at zero magnetic field is plotted to the left, indicated by the blue line. The dashed red line connects the resonances of both plots. (experimental parameters: 5.2 GHz to 6.3, 110 kHz stepsize, remaining are equal to 100 nm thick resonator)

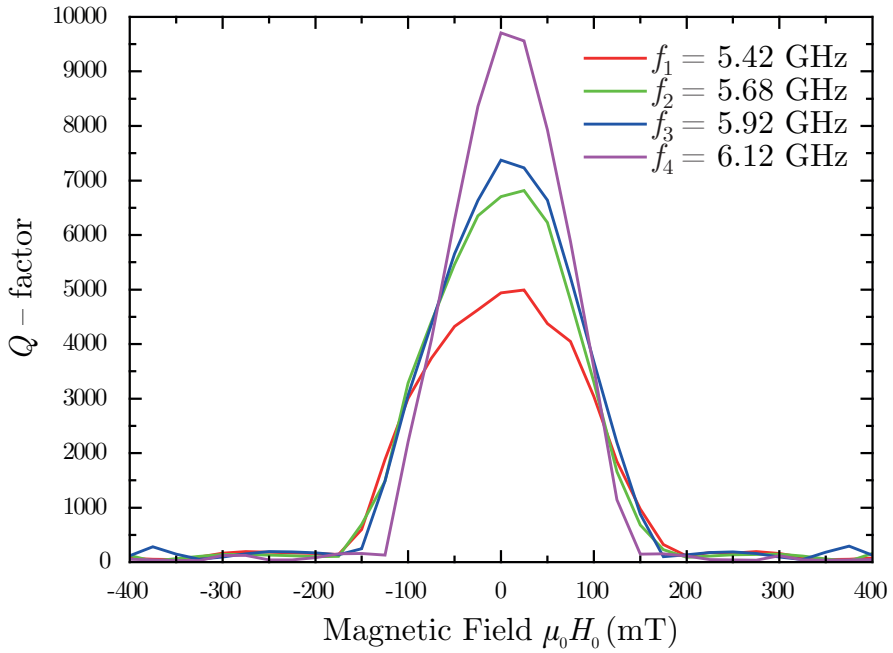

Figure 6.5.: Comparison of the against the magnetic field $\mu_0 H_0$ plotted Q-factors of the 200 nm thick Nb resonators.

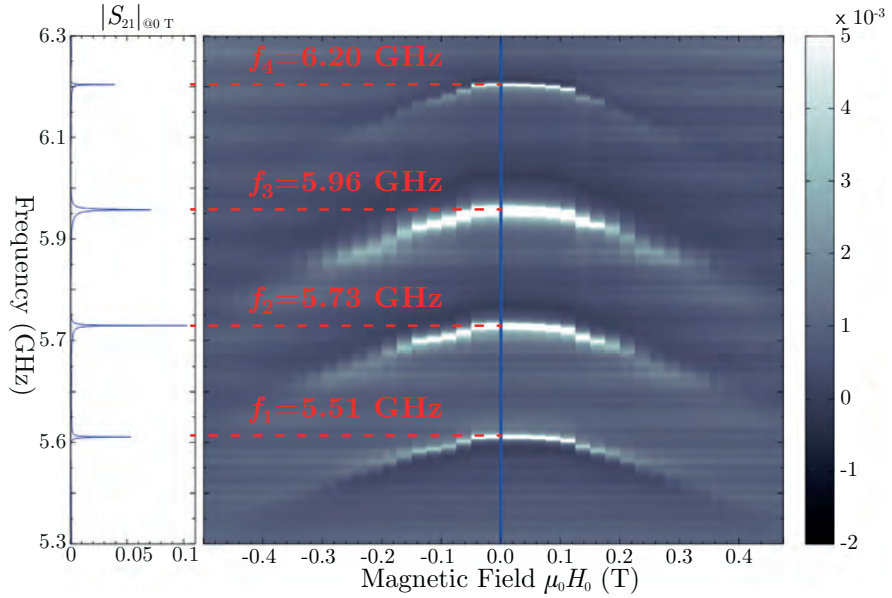

Figure 6.6.: Resonances of the 300 nm thick Nb multi-resonator chip at 2.2 K. To the left resides a plot of a cut at zero magnetic field, illustrated by the blue line and for better visualization connected by a dashed red line. (experimental parameters: 5.3 GHz to 6.3, 100 kHz stepsize, remaining are equal to 100 nm thick resonator)

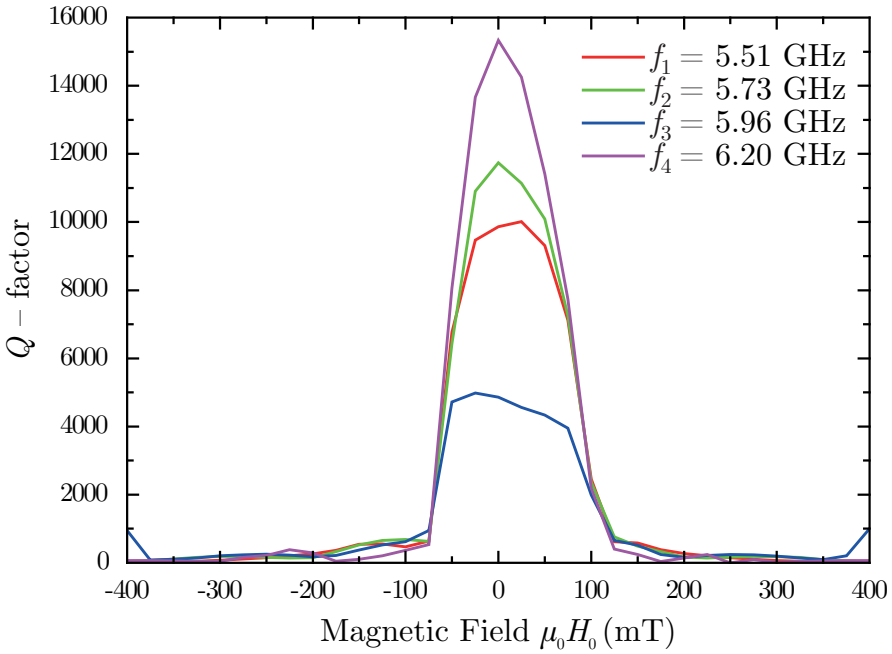

Figure 6.7.: Q-factor comparison of the 300 nm thick multi-resonator chip.

6.2. Strong Coupling in Ferromagnet-Resonator Hybrid System

In this section the interaction between the magnetic system of a Gallium doped YIG bulk crystal and a SC coplanar microwave resonator is presented. The measurement was performed at a temperature of 40 mK with the millikelvin FMR setup (cf. Sec. 4.1). The section finishes with a brief theoretical description of the coupling.

6.2.1. Yttrium Iron Garnet Sample

Yttrium Iron Garnet ($Y_3Fe_5O_{12}$) is a ferrimagnetic insulator. The magnetic moments of the Iron atoms are exchange coupled, resulting in a total magnetic moment of 5 μ_B. The unit cell of a YIG crystal consists of eight formula units, corresponding to a magnetic moment of 40 μ_B per unit cell. With a lattice constant $a_0 = 1238$ pm, this leads to a spin density of 2×10^{22} cm^{-3}. YIG exhibits excellent microwave properties and a narrow line width of approximately 10 μT [72], [73] are reported in the literature, making this system an excellent candidate for exploring the strong coupling regime in a SC microwave resonator-ferromagnet hybrid system.
The YIG bulk crystal used in the experiment was doped with Gallium, reducing the magnetization and increasing the FMR line width.
The sample has the dimension of approximately 2 mm × 1mm × 0.5 mm and is mounted on a multi-resonator chip, with the Nb film thickness of 100 nm, on the resonator with a zero magnetic field resonance frequency $f_4 = 5.97$ GHz.

6.2.2. Millikelvin Data

The measurement of the Ga doped YIG was conducted at a temperature of 40 mK. The microwave output power of the VNA was set to −40 dBm, corresponding to an effective microwave power of −50 dBm (10 nW) at the sample. An If bandwidth of 100 Hz was used. The frequency range of 4 GHz to 7.5 GHz was swept with a stepsize of 1.75 MHz, and the magnetic field ranged from −300 mT to +300 mT, swept in 2 mT steps. The magnetic field was applied in a direction parallel to the resonator surface. From the measured real- and imaginary part of the transmission, the in Fig. 6.8 shown dispersion plot of the magnitude $|S_{21}|$ is obtained.
In the plot, the three resonators, with the resonance frequencies f_1, f_2 and f_4, are

visible. Comparing the first two resonators with their previous measurement at 2.7 K (Fig. 6.2), an increase in robustness to the magnetic field for the resonators at 40 mK is observed which is attributed to the lower temperature. The superconductor has more condensation energy to eject the magnetic field, thus remains longer in the superconducting state with increasing magnetic field $\mu_0 H_0$ [74].

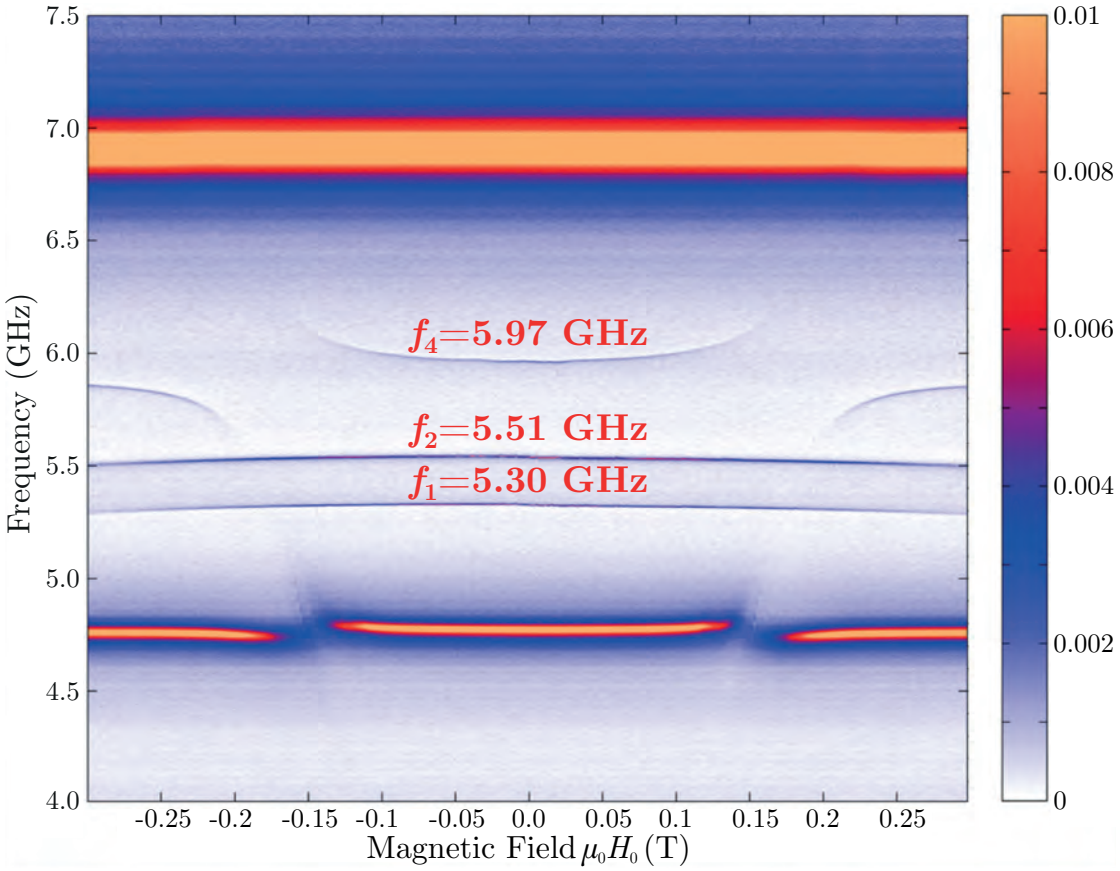

Figure 6.8.: Dispersion plot of the Ga doped YIG sample, mounted on a 100 nm thick Nb multi-resonator chip. At ±170 mT the resonator with zero magnetic field resonance frequency f_4 shows a strong avoided crossing.

The resonator with the resonance frequency f_4 exhibits a strong avoided crossing at ±170 mT. Here, the ferromagnetic resonance of YIG couples to the resonator mode, forming a hybrid system. The FMR dispersion line of YIG is not visible in the dispersion plot, because a transmission resonator geometry is not appropriate to observe an absorption spectrum. The resonator transmits signals, with frequencies in the region of its resonance frequency. Taking this into account as well as the very narrow line width of YIG, the absence of a well defined FMR line can be explained.

At a frequency of about 4.75 GHz, a very broad resonance is situated, not originating from the SC coplanar microwave resonators. Here, the microwave forms a standing electromagnetic wave within the volume of the sample box (cf. Sec. 4.3). This box resonance exhibits also an interaction the FMR of YIG at ±150 mT, which allows to follow the FMR line over 1.5 GHz.

6.2.3. Theoretical Description of the Coupling

The coupling between the ferromagnetic resonance mode and the SC microwave resonator mode is described by the coupling strength g_C. For a exchanged coupled spin ensemble it is given by [18], [16], [75], [11]

$$g_C = g_0\sqrt{N} \; ; \; g_0 \approx m_0\sqrt{\frac{\mu_0 f_C}{2hV_C}} \tag{6.1}$$

where N is the number of coupled spins and g_0 is the coupling strength of a single spin, with magnetic moment m_0, to the resonator cavity, with frequency f_C and mode volume V_C. The mode volume can be estimated with the length of the resonator (3 mm) and the separation of the center conductor and the ground planes (6 μm × 6 μm) [13]. With the magnetic moment of YIG (5 μ_B) and a frequency of $f_C = 6$ GHz, this results in a coupling strength $g_0/(2\pi) \approx 13.5$ Hz. The coupling strength g_0 is not high, but is enhanced by the spin ensemble. The number of participating spins can be estimated with half the mode volume of the resonator (due to the mounting of the sample) and the spin density of YIG (cf. Sec. 6.2.1) to $N = 18 \times 10^{18}$, resulting into an estimated coupling strength $g_C/(2\pi) \approx 443.66$ MHz.
To reach the regime of strong coupling, the losses of the system, governed by the relaxation rate of the spin ensemble γ_S and the decay rate of the resonator κ_C, have to be smaller than the coupling strength g_C.
Figure 6.9 (a) shows the dispersion plot obtained from the the measurement presented in Sec. 6.2.2, zoomed in on the avoided crossing at the positive magnetic field range. In figure 6.9 (b) the dispersion plot is overlayed by a red line, describing the avoided crossing. The red line was calculated by assuming two harmonic oscillators, with a constant microwave resonator frequency of $f_C = 5.96$ GHz and a linear FMR dispersion $f_S = g\mu_B\mu_0 H_0/(2\pi\hbar)$, describing the left red line of Fig. 6.9 (b) by f_{left}, and the

right by f_{right} [18].

$$f_{\text{left}} = \frac{1}{2}(f_{\text{C}} + f_{\text{S}} + \sqrt{(f_{\text{C}} - f_{\text{S}})^2 + {}^{4g_{\text{C}}^2}/_{(2\pi)^2}}), \tag{6.2}$$

$$f_{\text{right}} = \frac{1}{2}(f_{\text{C}} + f_{\text{S}} - \sqrt{(f_{\text{C}} - f_{\text{S}})^2 + {}^{4g_{\text{C}}^2}/_{(2\pi)^2}}). \tag{6.3}$$

For the red lines overlayed in Fig. 6.9 (b) a coupling strength g_{C} of 450 MHz is used to describe the experimental observation, matching the estimated coupling strength very well.

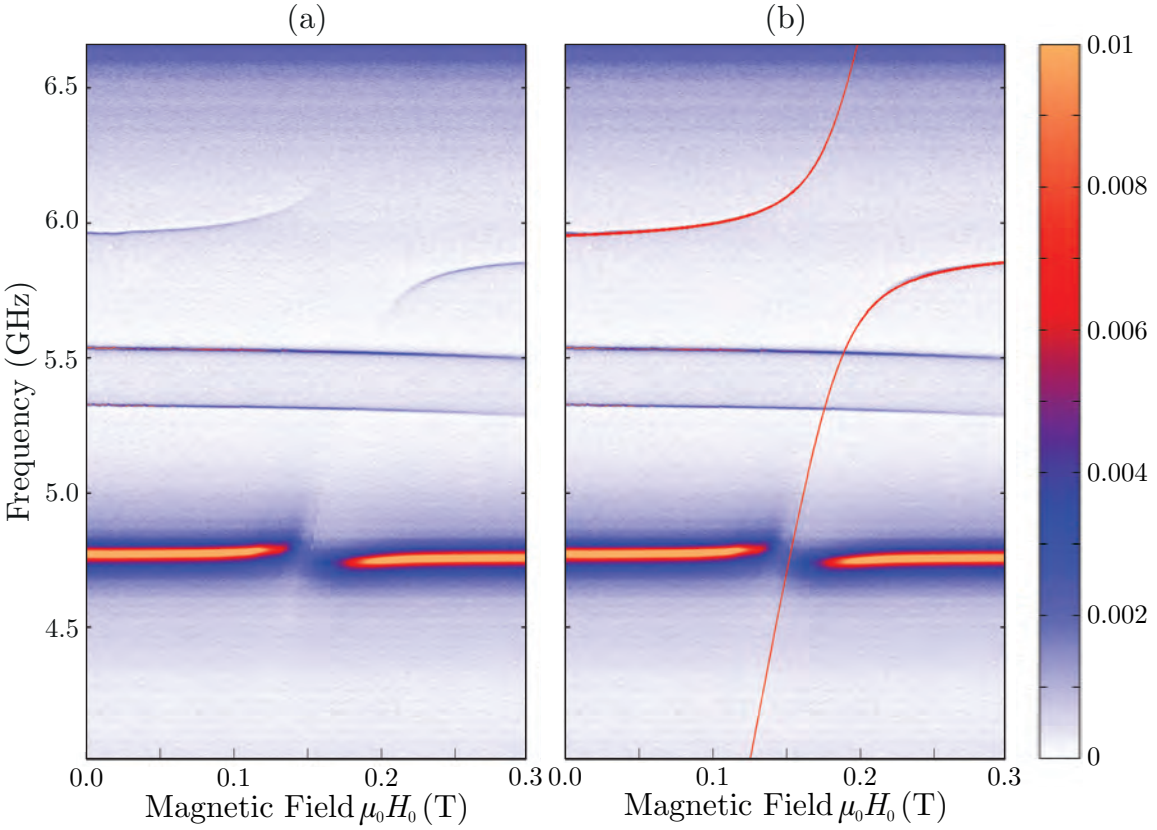

Figure 6.9.: (a) dispersion plot of the Ga doped YIG sample, showing the avoided crossing for the positive magnetic field range. (b) dispersion plot overlayed by a red line, describing the avoided crossing, by assuming two coupled harmonic resonators.

To access the relaxation rates of the system, which are critical parameters for judging if strong coupling is present, the line width κ of the coupled system is investigated as a function of the magnetic field. Figure 6.10 shows the extracted line width as a function of the magnetic field. Here, the line width obtained for zero magnetic field

allows to extract $\kappa_C/(2\pi) = 3$ MHz. According to theory the expected line width κ should take the following form [76]

$$\kappa = \kappa_C + \frac{g_C^2 \gamma_S}{(\omega - \omega_C)^2 + \gamma_S^2}, \tag{6.4}$$

where $(\omega - \omega_C)$ gives the detuning from the zero magnetic field resonance frequency of the resonator. The red line in Fig. 6.10 uses a relaxation rate of $\gamma_S/(2\pi) = 100$ MHz. Directly around the avoided crossing no line width data could be extracted,

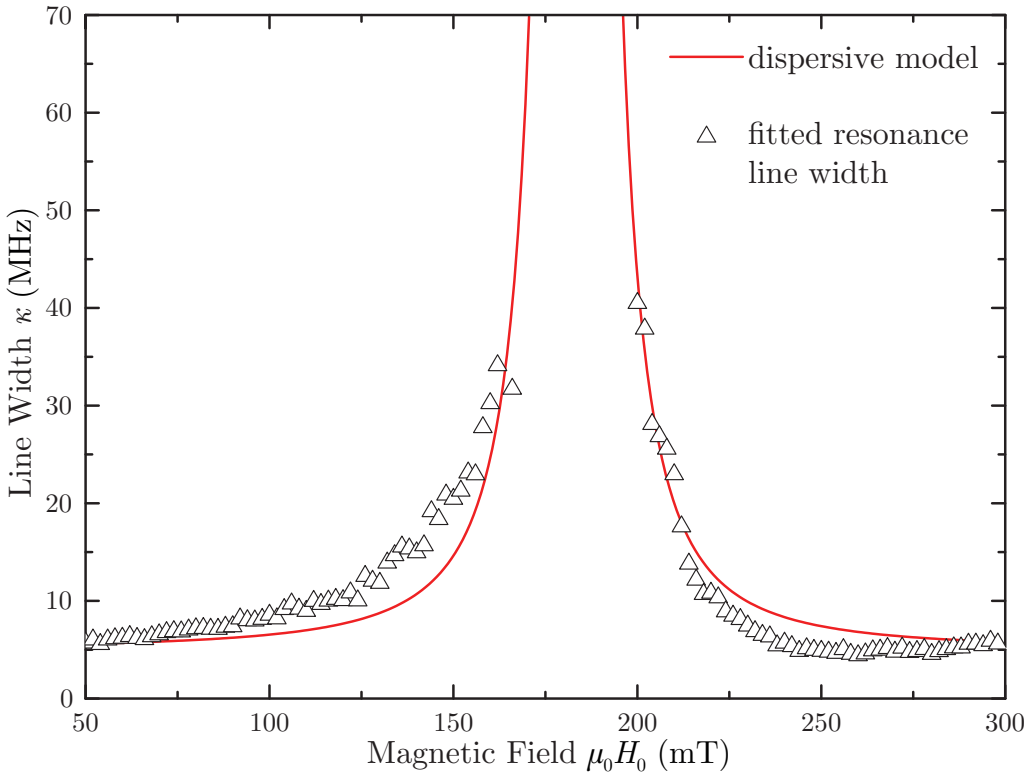

Figure 6.10.: Fitted line width of the microwave resonator resonances, for a region around the avoided crossing (triangles). The red line is a fit to the experimental data, using (6.4).

because the resonance line is pushed out of the transmitting region of the microwave resonator, resulting in a strong suppression of the transmitted microwave signal. Comparing the obtained parameters, shows that $g_C \gg \kappa_C,\ \gamma_S$. In cavity QED the coupling strength is given by the dimensionless cooperativity C [77]:

$$C = \frac{g_C^2}{\kappa_C \gamma_S}. \tag{6.5}$$

The coupling is considered strong when $C > 1$, meaning that every photon entering the cavity is coherently transferred into the spin ensemble [15]. With the determined parameters, a cooperativity of $C = 675$ is obtained, showing that the hybrid system is far in the strong coupling limit.

These first experiments on a SC microwave resonator-ferromagnet hybrid system showed a high cooperativity, though the relaxation rate of the spin ensemble γ_S being relatively high, most probable caused by the Ga doping. Therefore, an experiment with pure YIG should result in a stronger coupling. Further, the microwave resonator structure could be further optimized, effectively reducing the Q-factor, so that the avoided crossing can be traced over a wider frequency range. A goal for these experiments would be the transition from the currently multi photon limit into a single photon limit. This would allow to investigate superpositions of photons with spin waves.

... — dary!

Barney Stinson

Chapter 7.

Summary and Outlook

The work presented in this thesis summarizes two approaches towards measuring ferromagnetic resonance (FMR). On the one, a broadband detection is used, employing a coplanar waveguide, to investigate magnetization damping in Holmium doped Permalloy ($Ni_{80}Fe_{20}$) in the temperature range from room-temperature down to 50 millikelvin. On the other hand, magnon-photon interactions are investigated in a Yttrium Iron Garnet (YIG) - superconducting microwave cavity hybrid, at 40 millikelvin.

To begin with, an existing dilution refrigerator, equipped with high-frequency lines, allowing transmission experiments up to 24 GHz. The setup was tested using a Cobalt thin film, known to show an intensive FMR signal. With this material system, first FMR experiments are performed, demonstrating that the FMR can be detected broadband up to 500 mT at the base temperature of the dilution refrigerator, covering the range where FMR is expected. The intensity of the incident microwave power was varied and FMR could be observed down to the level of 100 fW at the Cobalt thin film. The dispersion, which can be extracted from the datasets, is understood in terms of a free energy approach, showing that the demagnetization and anisotropy parameters do not change at these low temperatures.

Turning to the investigation of magnetization damping in Permalloy, doped with the rare-earth element Holmium. The fundamental interest is the independent tailoring of the magnetic damping and the resonance frequency for magnetic materials. This system was studied by G. Woltersdorf et al. intensively in the temperature range between 100 K and 350 K [8]. Based on their observations and model, which predicts an increase in the FMR line width with decreasing temperature with a peak around 100 K and subsequently a decrease, the temperature range was investigated down

to 50 mK. Since the dilution refrigerator cannot operate up to room temperature, temperatures between 300 K and 4 K were investigated with a helium flow cryostat. The FMR line width extracted corroborates the previously existing data between 300 K and 100 K. A maximum in line width was observed around 100 K, with the line width being almost a factor of 4 larger than at room temperature. For temperatures below 20 K the line width saturated at the magnitude of room temperature. The temperature dependent line broadening is understood in the frame of the slow relaxing impurity model, originally describing this effect for RE doped Yttrium Iron Garnets (YIG), a ferrimagnetic insulator. For temperatures above 140 K the experimental data is in good agreement with this theoretical model. The experimentally observed line width maximum is 25 % larger than the theoretically predicted. This is attributed to additional damping effects, present in metallic materials, like eddy currents, which are not considered in the theoretical model. This also explains that, the predicted zero line width for zero temperature was not observed.

In addition to the expected temperature dependence of the FMR line width, a frequency shift of the FMR was observed. The FMR resonance condition starts to increase in frequency at temperatures below 130 K, saturating in a zero magnetic field resonance frequency of $\sim$ 14 GHz below 20 K. The effect is attributed to the Holmium doping, confirmed by comparison with a pure Permalloy thin film. Pure Holmium exhibits a ferromagnetic transition at 115 K, reaching its maximal magnetic moment at around 20 K [70]. The current model outlined in this thesis assumes, that the Holmium atoms generate an internal offset field, effectively shifting the FMR. A quantitative estimation of the magnitude of the effect indicates that the Holmium atoms do not act entirely decoupled from the Permalloy host material. In the decoupled case the shift is expected in the order of 0.9 GHz, more than a magnitude smaller than the observed. Therefore, the exchange between Permalloy and Holmium has to be taken into account.

Finally, strong coupling in a microwave resonator-ferromagnet hybrid system was studied. Since, for such experiments magnetic fields in the range of hundred millitesla are needed, a characterization of the magnetic field dependency on the quality factor of a superconducting coplanar microwave resonator was carried out. The characterization was performed for three different layer thicknesses of Niobium at a temperature of about 2.5 K. The magnetic field dependent quality factors of the different resonators are compared, showing that the thickest resonator, with a 300 nm Niobium

layer, exhibited the highest robustness to the magnetic field. For the experiment a Gallium doped YIG bulk crystal was used with a spin density estimated to 2×10^{22} cm^{-3}. Millikelvin broadband FMR measurements were performed on the microwave resonator loaded with the Gallium doped YIG sample. At a temperature of 40 mK an avoided crossing of the resonator line is identified at ± 170 mT and about 6 GHz, attributed to the coupling between the resonator and the FMR. The avoided crossing was fitted, by a coupled harmonic oscillator model, yielding a coupling strength of 450 MHz. From the line width of the uncoupled resonator at zero magnetic field the decay rate of resonator was found to be 3 MHz. The magnetic field dependency of the resonator line width in the region of the avoided crossing, allows to extract the relaxation rate of the spin system to 100 MHz. Both decay rates are smaller than the coupling strength, demonstrating the strong coupling regime.

Outlook

In this thesis a new setup was established to investigate magnetic systems with microwaves at millikelvin temperatures. This yet unexplored temperature realm allows to investigate magnetization damping and anisotropy parameters, combining material science with fundamental physics.

With respect to the research on Holmium doped Permalloy presented in this thesis the next obvious steps are to investigate the set of existing rare-earth doped Permalloy thin films systematically in the now accessible temperature regime. The investigation allows to identify the dependency of the line width on temperature, with respect to the rare-earth impurity concentration. Hereby, the slow relaxing impurity model can be further extended for metallic ferromagnets. The itinerant nature of the electrons in metallic materials, gives rise to additional damping mechanisms not present in insulators. Damping by eddy currents is one such possible mechanism. They also exhibit a temperature dependency, since they are direct proportional to the conductivity [31], which increases with decreasing temperature [66]. By taking such effects into account, the larger experimentally observed line width can be explained as well as the saturation of the line width for temperatures below 20 K.

According to the model presented in Chapter 5 a further increase in the zero magnetic field frequency shift of the FMR line is expected with increasing rare-earth impurity concentration, warranting further experimental studies.

Furthermore, magnetization damping can now be studied down to low temperatures.

While Permalloy seems to be dominated by damping mechanisms not related to the rare-earth slow relaxing model at low temperatures, the Garnets are known not to suffer this limitation. In the Garnets rare-earth doping is generally applied commercially to tailor the high frequency properties in terms of saturation magnetization and magnetic damping. The properties of doped systems are generally dominated solely by these dopants. Doped Garnets are investigated down to temperatures of pumped helium of about 1 K, showing a decrease in the line width as a function of temperature [5]. Smallest line width are reported for bulk single crystal Yttrium Iron Garnet spheres of approximately 10 μT [72]. Because the line width directly translates to a lifetime of the magnonic system of 0.6 μs [78], this material system is a prime candidate for the investigation of magnon-photon coupling on a single photon level, besides the investigation of the magnetic damping of YIG in this temperature range.
The strong coupling experiment presented here yielded promising results for future projects. But first, the individual components need further optimization. The avoided crossing of the resonator line could only be traced in a narrow frequency range. This is a result of the high quality factor of the superconducting microwave resonator. To increase the transmitting region of the resonator the quality factor has to be reduced, i.e. by increasing the coupling capacity. Hereby, the avoided crossing can be traced over a wider frequency range, allowing for a better investigation of the avoided crossing. To further increase the coupling strength the spin ensemble relaxation rate can be reduced. The relaxation rate of 100 MHz in the experiment showed to be rather high, which was attributed to the Gallium doping of the YIG. Therefore, the use of pure YIG surely will improve the coupling, giving room for a quality factor reduction of the resonator.
An important achievement for this experimental course will be the transition from the current multi photon limit to the single photon limit. To realize such a transition, the incident microwave power has to be reduced. Therefore, the signal-to-noise ratio of the current setup needs to be improved significantly, e.g. by a cold amplifier. In the single photon limit only a single photon remains in the resonator on average. The photon can be absorbed by the strongly coupled spin ensemble, converting the photonic state into a spin wave state and back again. In other words, information is transfered to the spin system on a quantum level, which is very appealing for the investigation of quantum mechanical effects.
Additionally, a great advantage of the resonator-ferromagnet hybrid system, is its high

spin density. The number of spins required to reach strong coupling can be integrated in a volume of about one cubic micron, forming a micro magnet. This would allow to investigate multiple spin ensembles coupled to a single superconducting microwave resonator and thus indirectly coupled with each other. To individually tune the resonance frequency of each spin ensemble additional current lines need to be installed to locally control the magnetic environment of the micro magnets. Hereby, each spin ensemble could be addressed separately.

Appendix A.

$Ni_{80}Fe_{20}$:Ho_1 Temperature Series

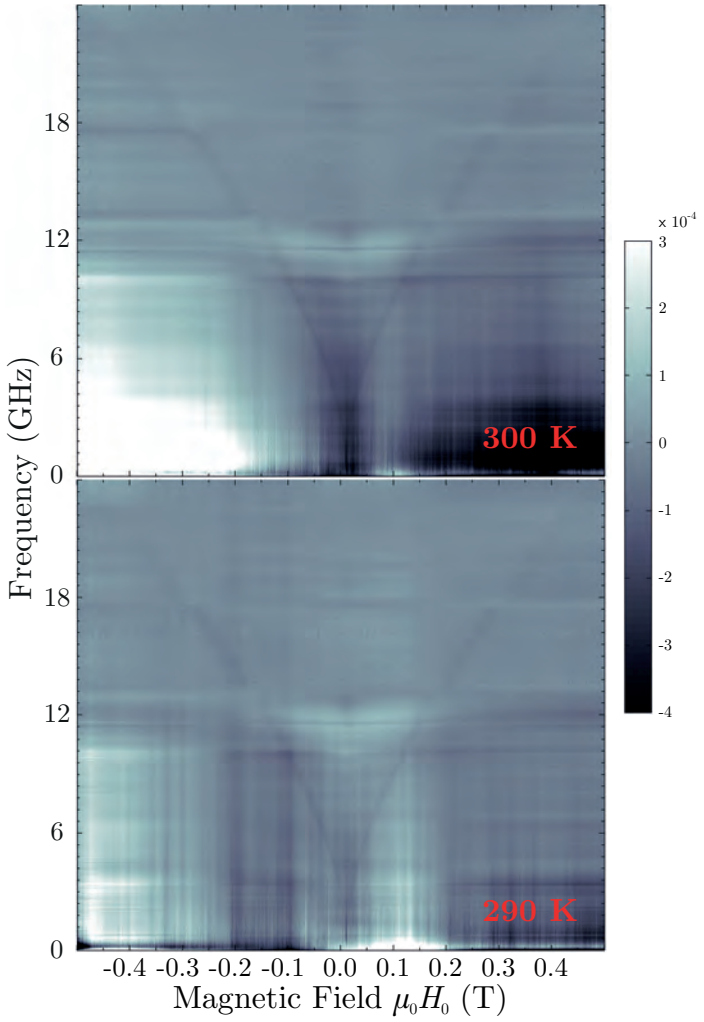

Figure A.1.

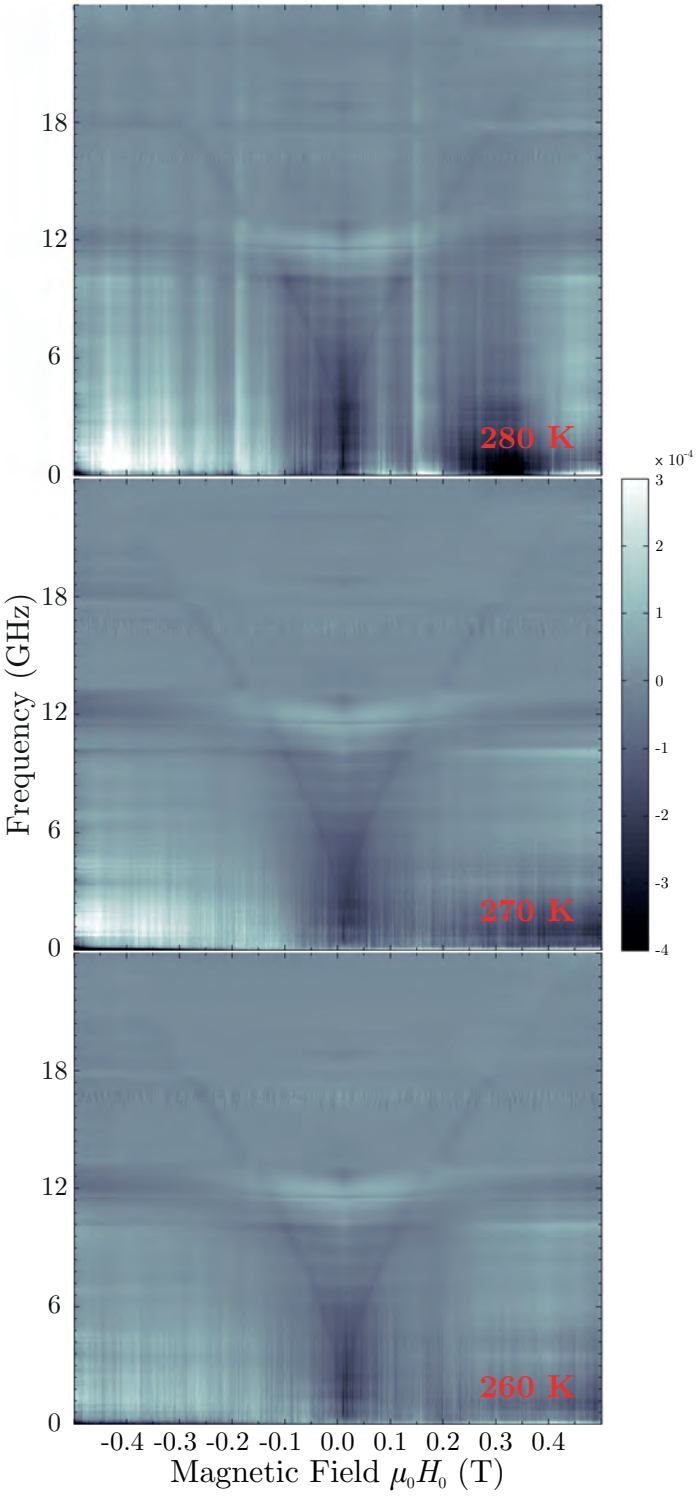
280 K
270 K
260 K
Frequency (GHz)
0
6
12
18
-0.4 -0.3 -0.2 -0.1 0.0 0.1 0.2 0.3 0.4
Magnetic Field $\mu_0 H_0$ (T)
x 10^-4
3
2
1
0
-1
-2
-3
-4

Figure A.2.

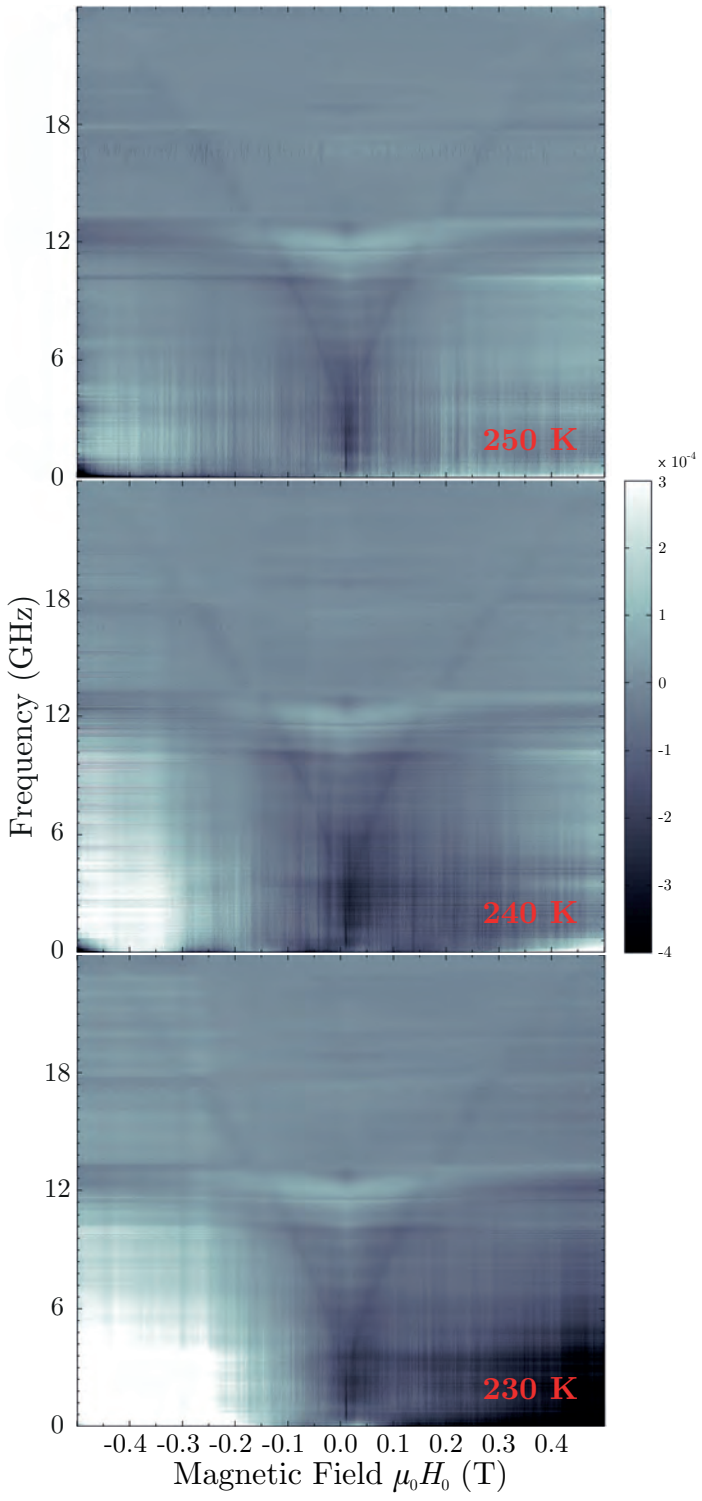
250 K
240 K
230 K
Frequency (GHz)
0
6
12
18
-0.4 -0.3 -0.2 -0.1 0.0 0.1 0.2 0.3 0.4
Magnetic Field $\mu_0 H_0$ (T)
x 10^-4
3
2
1
0
-1
-2
-3
-4

Figure A.3.

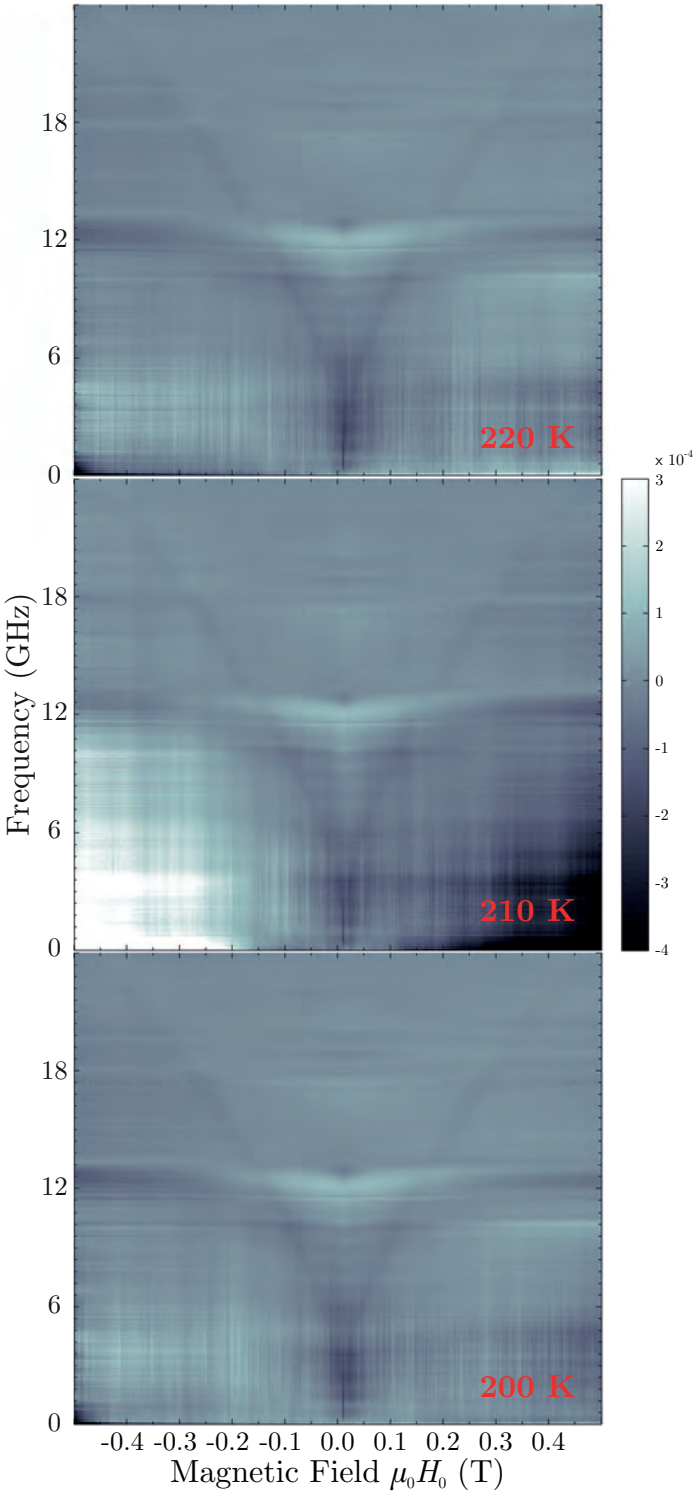
220 K
210 K
200 K
Frequency (GHz)
18
12
6
0
-0.4 -0.3 -0.2 -0.1 0.0 0.1 0.2 0.3 0.4
Magnetic Field $\mu_0 H_0$ (T)
x 10^-4
3
2
1
0
-1
-2
-3
-4

Figure A.4.

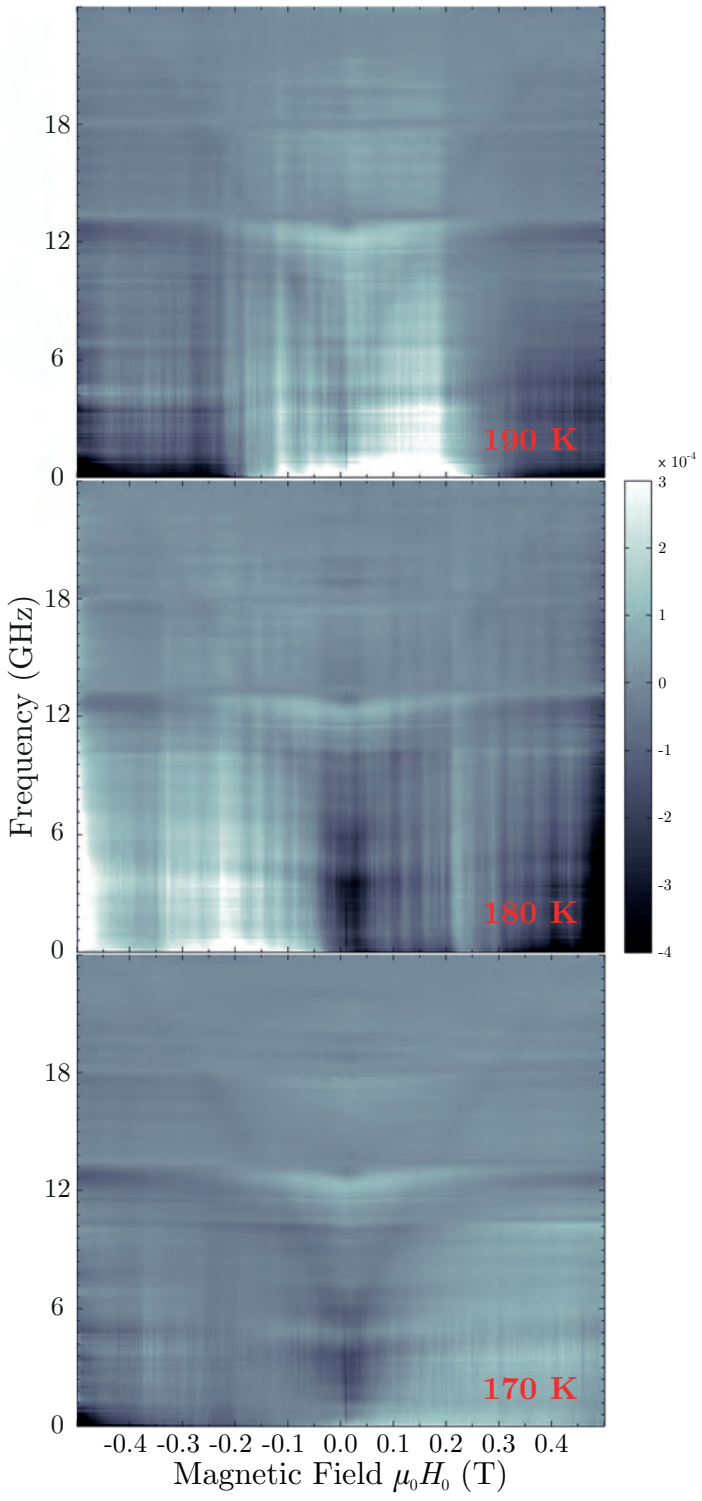

Figure A.5.

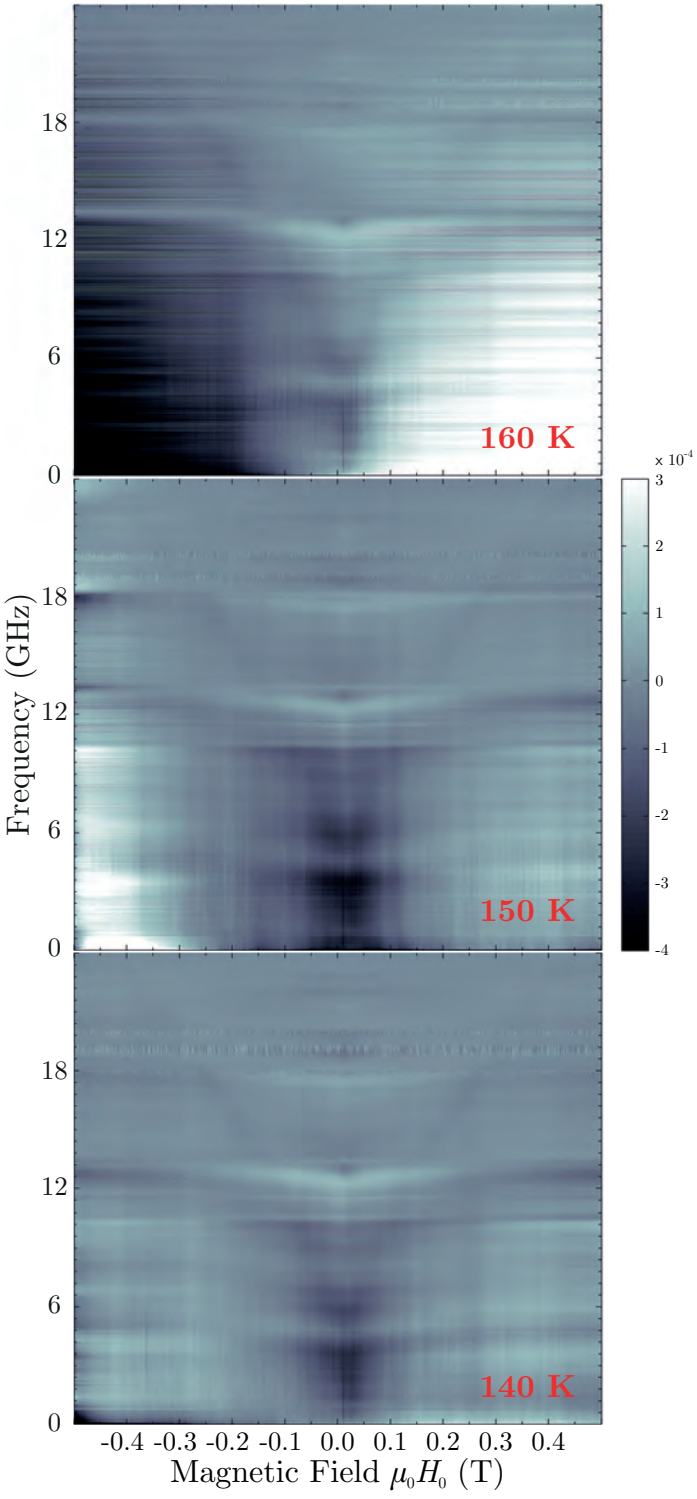

Figure A.6.

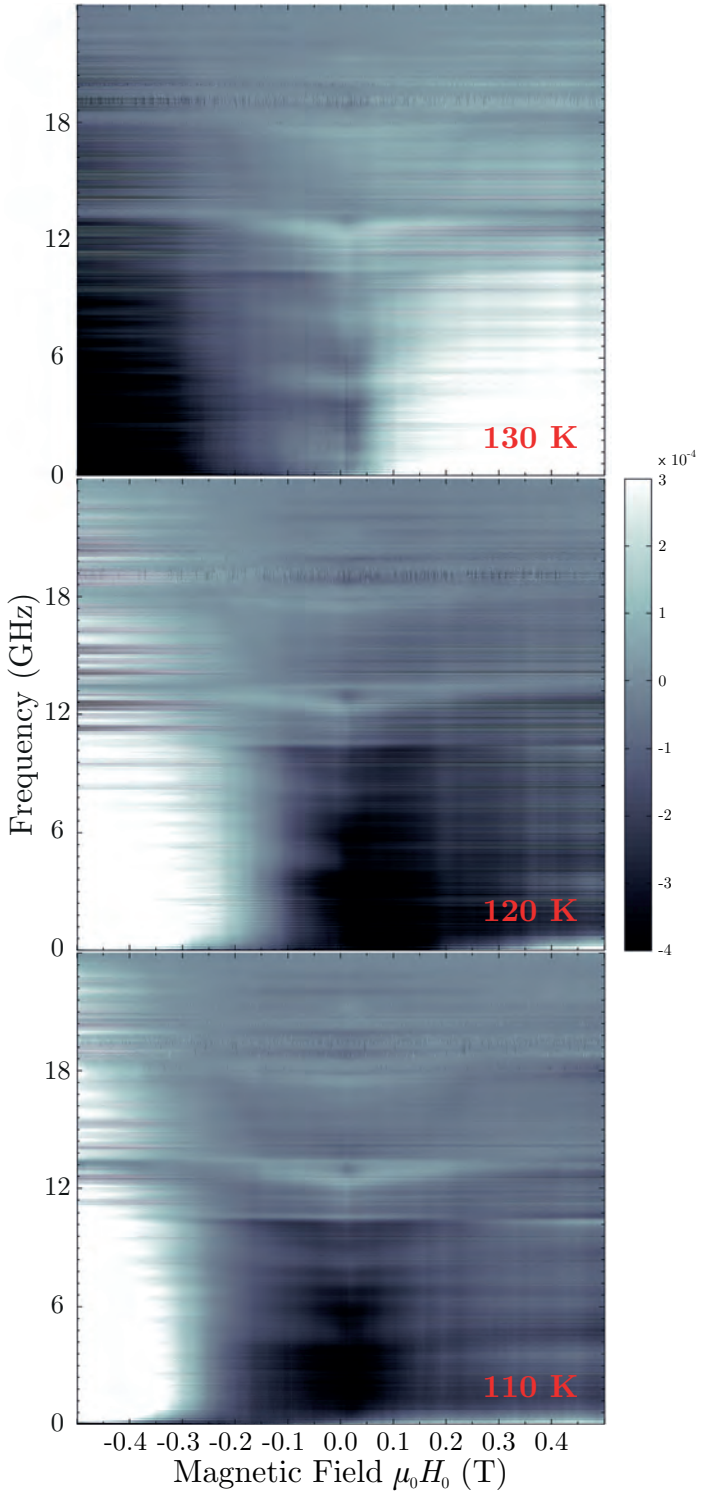

Figure A.7.

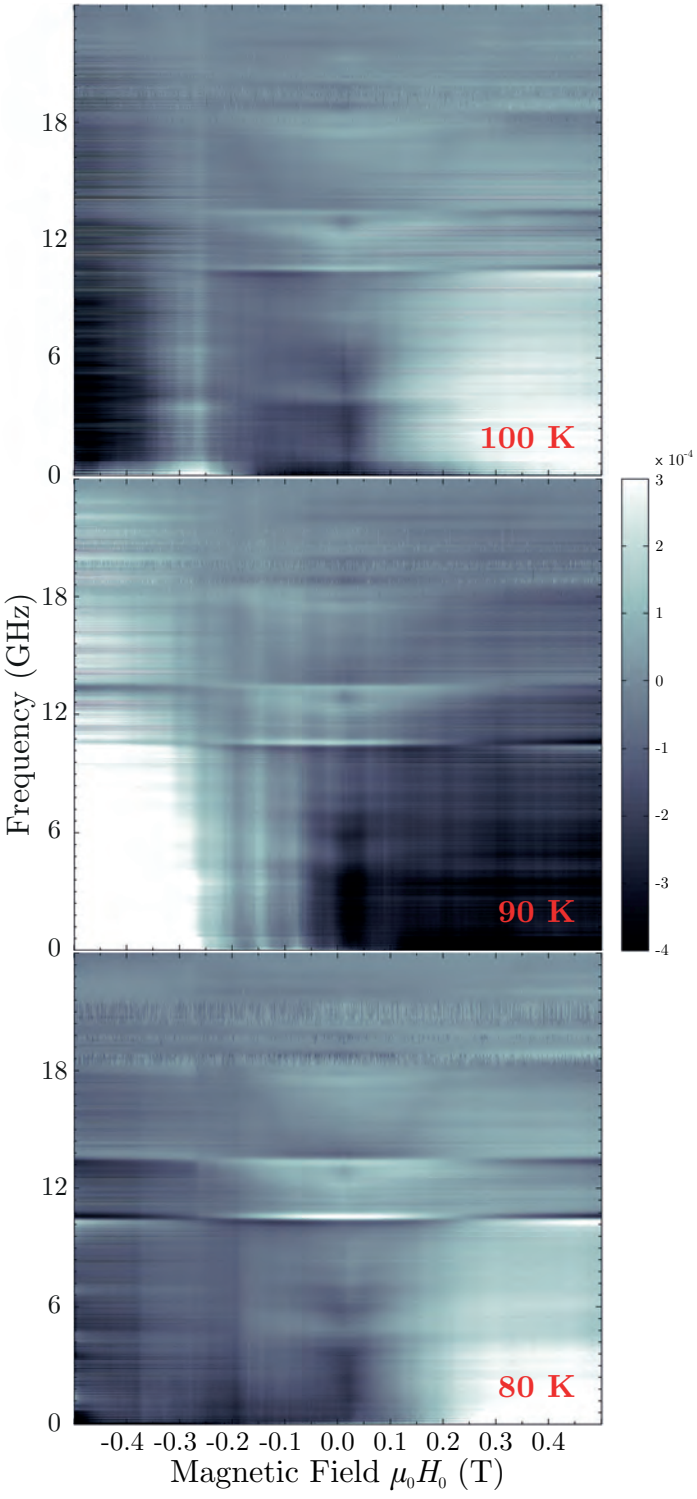
100 K
90 K
80 K
Frequency (GHz)
0
6
12
18
-0.4 -0.3 -0.2 -0.1 0.0 0.1 0.2 0.3 0.4
Magnetic Field $\mu_0 H_0$ (T)
x 10^-4
3
2
1
0
-1
-2
-3
-4

Figure A.8.

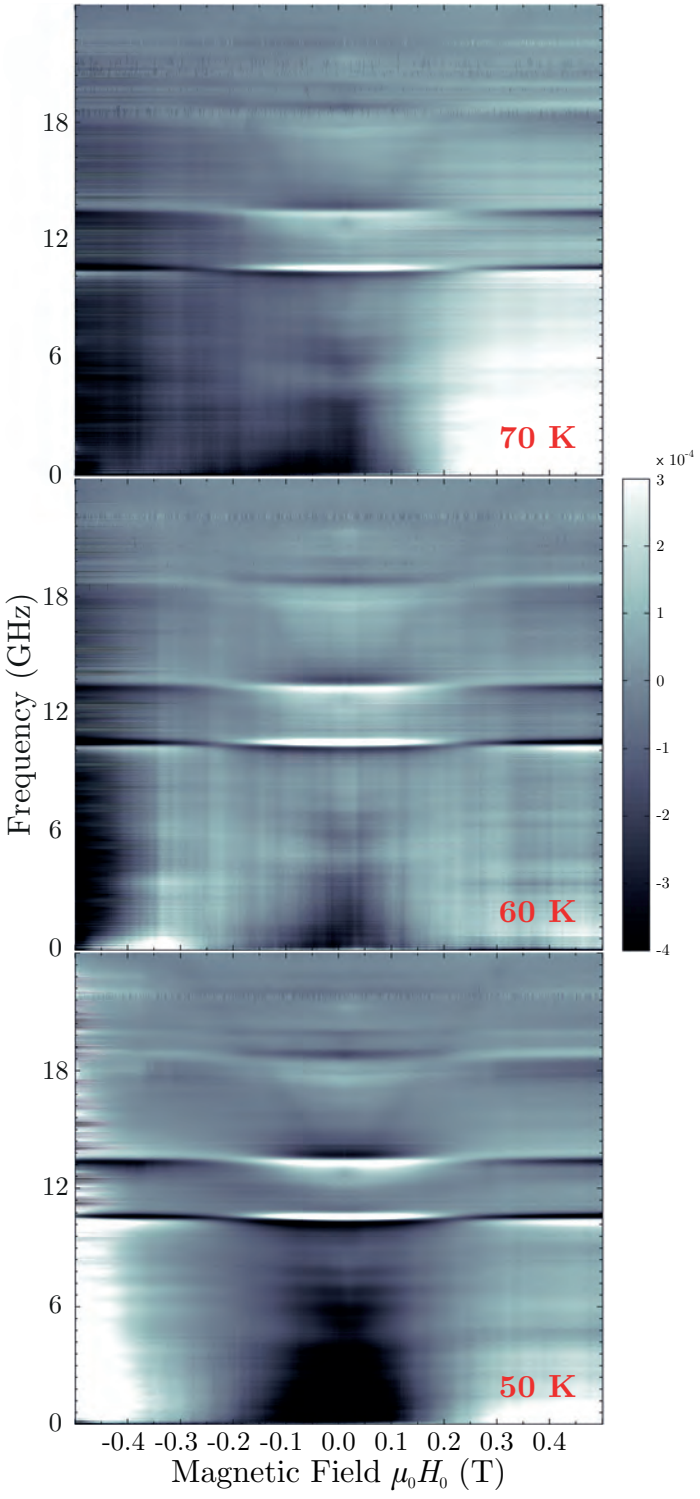
70 K
60 K
50 K
Frequency (GHz)
0
6
12
18
-0.4 -0.3 -0.2 -0.1 0.0 0.1 0.2 0.3 0.4
Magnetic Field $\mu_0 H_0$ (T)
x 10^-4
3
2
1
0
-1
-2
-3
-4

Figure A.9.

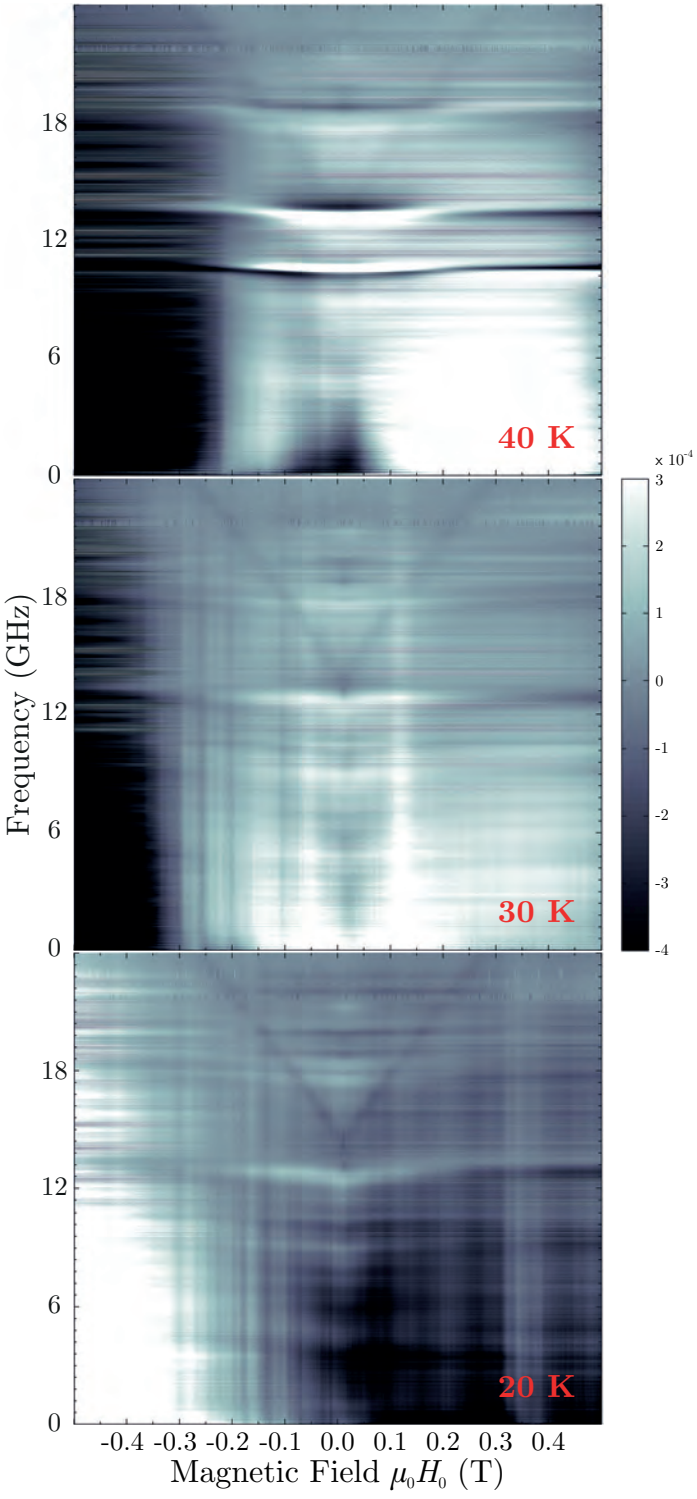
40 K
30 K
20 K
Frequency (GHz)
0
6
12
18
-0.4 -0.3 -0.2 -0.1 0.0 0.1 0.2 0.3 0.4
Magnetic Field $\mu_0 H_0$ (T)
x 10^-4
3
2
1
0
-1
-2
-3
-4

Figure A.10.

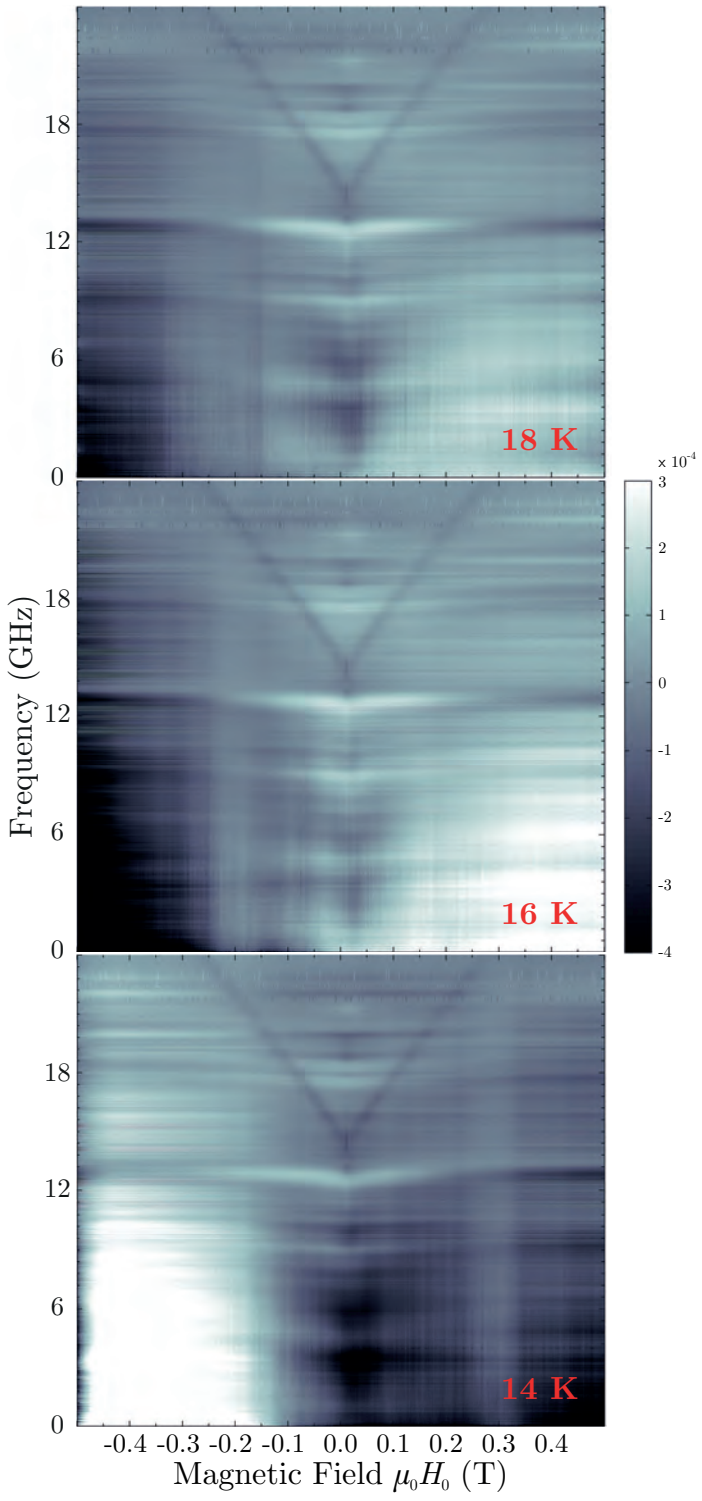

Figure A.11.

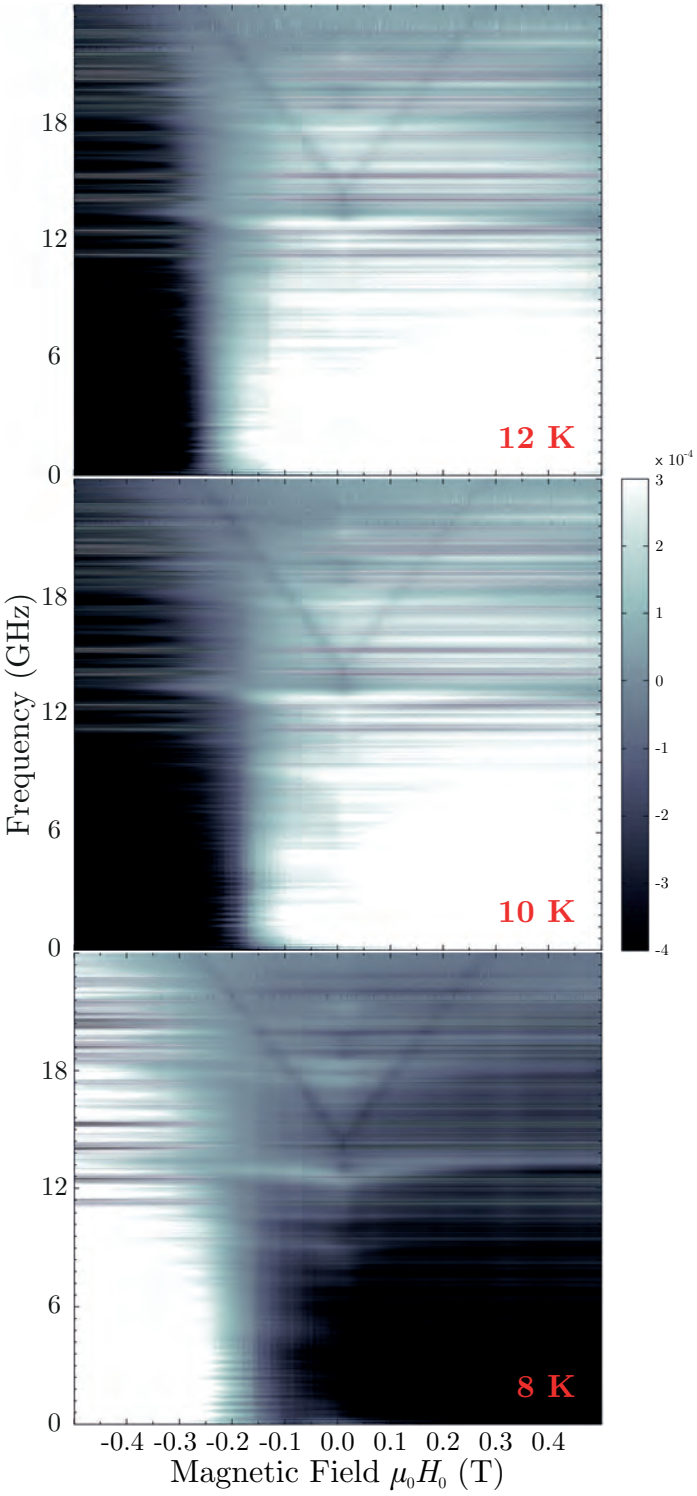

Figure A.12.

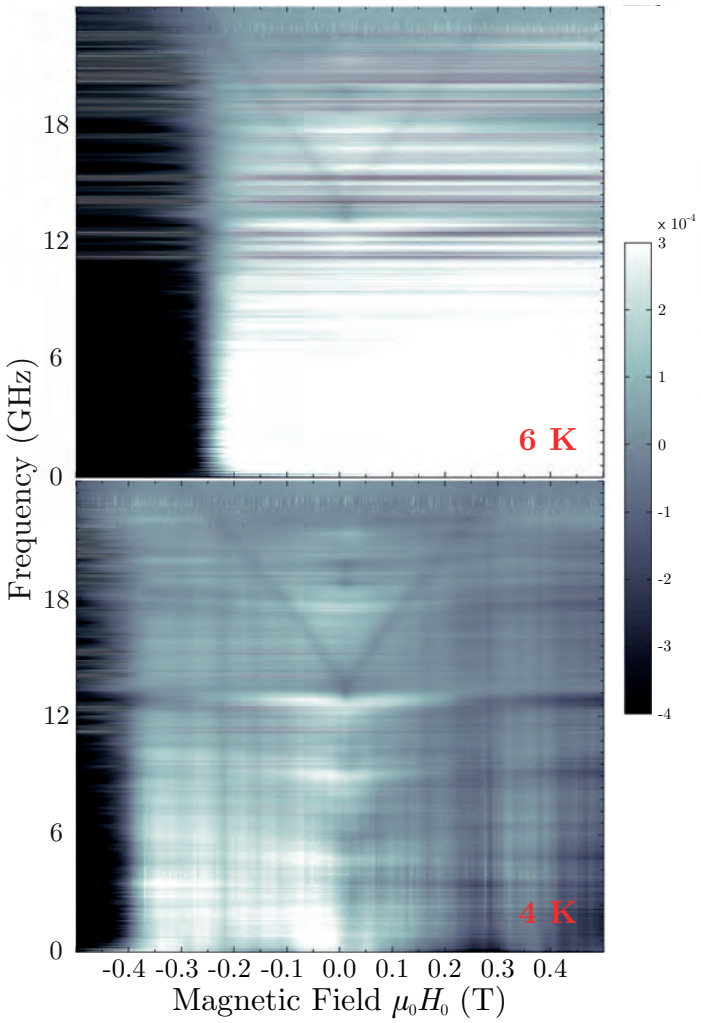
18
12
6
0
6 K
18
12
6
0
4 K
Frequency (GHz)
-0.4 -0.3 -0.2 -0.1 0.0 0.1 0.2 0.3 0.4
Magnetic Field $\mu_0 H_0$ (T)
x 10^-4
3
2
1
0
-1
-2
-3
-4

Figure A.13.

Bibliography

[1] J. H. E. Griffiths, Nature **158**, 670 (1946).

[2] E. K. Zavoiskii, Journ. Phys. USSR **10**, 197 (1946).

[3] S. V. Vonsovskii, *Ferromagnetic Resonance* (Israel Program for Scientific Translations Ltd., Published under the guidance of the editorial board of "Uspekhi Fizicheskikh Nauk", Jerusalem, 1964).

[4] R. Gross, *Tieftemperaturphysik 2 lecture notes* (TU München, 2004-2010).

[5] M. Sparks, *Ferromagnetic-Relaxation Theory* (McGraw-Hill Book Company New York San Francisco Toronto London, 1964).

[6] W. E. Bailey, P. Kabos, F. Mancoff, and S. Russek, IEEE Trans. Magn.I **37**, 4 (2001).

[7] S. G. Reidy, L. Cheng, and W. E. Bailey, Appl. Phys. Lett. **82**, 8 (2002).

[8] G. Woltersdorf, M. Kiessling, G. Meyer, J.-U. Thiele, and C. H. Back, Phys. Rev. Lett. **102**, 257602 (2009).

[9] G. Nahrwold, J. M. Scholtyssek, S. Motl-Ziegler, O. Albrecht, U. Merkt, and G. Meier, J. Appl. Phys. **108**, 013907 (2010).

[10] T. Niemczyk, *From strong to ultrastrong coupling in circuit QED architectures*, Ph.D. thesis, Technische Universität München (2011).

[11] R. Amsüss, C. Koller, T. Nöbauer, S. Putz, S. Rotter, K. Sandner, S. Schneider, M. Schramböck, G. Steinhauser, H. Ritsch, J. Schmiedmayer, and J. Majer, Phys. Rev. Lett. **107**, 060502 (2011).

[12] H. Paik, D. I. Schuster, L. S. Bishop, G. Kirchmair, G. Catelani, A. P. Sears, B. R. Johnson, M. J. Reagor, L. Frunzio, L. I. Glazman, S. M. Girvin, M. H. Devoret, and R. J. Schoelkopf, arXiv: **1105.4652v4** (2011).

[13] A. Imamoğlu, Phys. Rev. Lett. **102**, 083602 (2009).

[14] J. H. Wesenberg, A. Ardavan, G. A. D. Briggs, J. J. L. Morton, R. J. Schoelkopf, D. I. Schuster, and K. Mølmer, Phys. Rev. Lett. **103**, 070502 (2009).

[15] D. I. Schuster, A. P. Sears, E. Ginossar, L. DiCarlo, L. Frunzio, J. J. L. Morton, H. Wu, G. A. D. Briggs, B. B. Buckley, D. D. Awschalom, and R. J. Schoelkopf, Phys. Rev. Lett. **105**, 140501 (2010).

[16] Y. Kubo, F. R. Ong, P. Bertet, D. Vion, V. Jacques, D. Zheng, A. Dre´au, J.-F. Roch, A. Auffeves, F. Jelezko, J. Wrachtrup, M. F. Barthe, P. Bergonzo, and D. Esteve, Phys. Rev. Lett. **105**, 140502 (2010).

[17] I. Chiorescu, N. Groll, S. Bertaina, T. Mori, and S. Miyashita, Phys. Rev. B **82**, 024413 (2010).

[18] E. Abe, H. Wu, A. Ardavan, and J. J. L. Morton, Appl. Phys. Lett. **98**, 251108 (2011).

[19] O. O. Soykal and M. E. Flatté, Phys. Rev. B **82**, 104413 (2010).

[20] O. O. Soykal and M. E. Flatté, Phys. Rev. Lett. **104**, 077202 (2010).

[21] A. Brandlmaier, *Electric-field Control of Magnetization in Multifunctional Hybrid Devices*, Ph.D. thesis, Technische Universität München (2011).

[22] J. D. Jackson, *Klassische Elektrodynamik* (Walter de Gruyter, Berlin: 4. Auflage, 1999).

[23] C. Kittel, Phys. Rev. **71**, 270 (1947).

[24] L. Landau and E. Lifshitz, Sow. Phys. **8**, 153 (1935).

[25] C. Kittel, *Einführung in die Festkörperphysik* (Oldenbourg Wissenschaftsverlag GmbH, München, 2006).

[26] T. L. Gilbert, Phys. Rev. **100**, 1243 (1955).

[27] F. Bloch, Phys. Rev. **70**, 7 (1946).

[28] S. Balac and L. Chupin, Fast approximate solution of Bloch equation for simulation of RF artifacts in magnetic resonance imaging,
Institut Camille Jordan, France
`http://math.univ-lyon1.fr/~chupin/FICHIERS-RECHERCHE/Balac-Chupin.pdf` (called 07.10.2011).

[29] N. Bloembergen, Phys. Rev. **78**, 572 (1950).

[30] R. S. Codrington, J. D. Olds, and H. Torrey, Phys. Rev. **95**, 607 (1954).

[31] J. A. C. Bland and B. Heinrich, *Ultrathin Magnetic Structures 3* (Springer-Verlag, Berlin, 2005).

[32] R. D. McMichael, M. D. Stiles, P. J. Chen, and W. F. Egelhoff, J. Appl. Phys. **83**, 7037 (1998).

[33] F. Giesen, *Magnetization Dynamics of Nanostructured Ferromagnetic Rings and Rectangular Elements*, Ph.D. thesis, Universität Hamburg (2005).

[34] R. Meckenstock, *Untersuchung der magnetischen Eigenschaften von Fe/Ag-Schichtsystemen mit der konventionellen und der ortsaufgelösten ferromagnetischen Resonanz*, Ph.D. thesis, Ruhr-Universität Bochum (1997).

[35] D. D. Stancil and A. Prabhakar, *Spin Waves Theory and Application* (Springer Science+Business Media, New York, 2009).

[36] M. Oogane, T. Wakitani, S. Yakata, R. Yilgin, Y. Ando, A. Sakuma, and T. Miyazaki, Jap. J. Appl. Phys. **45**, 3889 (2006).

[37] B. A. Mazin, *Microwave Kinetic Inductance Detectors*, Ph.D. thesis, California Institute of Technology (2004).

[38] D. C. Mattis and J. Bardeen, Phys. Rev. **111**, 412 (1958).

[39] He3-He4-phase diagram
`http://de.wikipedia.org/wiki/Datei:He3-he4-phasendiagramm.png`
(called 15.09.2011).

[40] C. Enss and S. Hunkling, *Tieftemperaturphysik* (Springer-Verlag Berlin, 2000).

[41] T. Varitanen, *Numerical Calculations of Quasiparticle Dynamics in a Fermi Liquid*, Ph.D. thesis, Department of Physics University of Oulu (2011).

[42] L. D. Landau and E. M. Lifshitz, *Course of Theoretical Physics Volume 9 Statistical Physics Part 2* (Pergamon Press, Oxford, 1980).

[43] R. A. H. Hartmut Frey, *Tieftemperaturtechnologie* (VDI-Verlag, Düsseldorf, 1981).

[44] T. Fließbach, *Statistische Physik Lehrbuch zur Theoretischen Physik IV* (Spektrum Akademischer Verlag, Heidelberg: 5. Auflage, 2010).

[45] J. W. Ekin, *Experimental Techniques: Cryostat Design, Material Properties and Superconductor Critical-Current Testing* (Oxford University Press, New York, 2006).

[46] W. D. Schleifer, *Hochfrequenz- und Mikrowellen-Meßtechnik in der Praxis* (Dr. Alfred Hütig Verlag, Heidelberg, 1981).

[47] M. Hiebel, *Grundlagen der vektoriellen Netzwerkanalyse* (Rohde & Schwarz GmbH & Co. KG, München, 2006).

[48] D. M. Pozar, *Microwave Engineering* (John Wiley and Sons Inc., New York, 1998).

[49] FMR linewidth measurement skriptum
University of Idaho
`http://www.mrc.uidaho.edu/em/Files/FMR_measurement.pdf` (called 14.11.2011).

[50] R. N. Simons and R. K. Arora, IEEE Trans. MIicrowave Theory Tech. **30**, 1094 (1982).

[51] M. Bahte, F. Herrmann, and P. Schmüser, Proceedings of the 1997 Workshop on RF Superconductivity, Abano Terme (Padova), Italy .

[52] OFHC information
`http://en.wikipedia.org/wiki/OFHC` (called 17.09.2011).

[53] specifications on Rosenberger connectors
http://www.rosenberger.de/PDF/Products_10_Communication_Standard/SMA.pdf (called 17.09.2011).

[54] specifications on Rosenberger SR coaxial cables
http://www.rosenberger.de/PDF/Publications/50_cables_alles/MCC_Cable_2009.pdf (called 18.11.2011).

[55] specifications on Astrolab SR steel coaxial cables
http://www.minibend.com/catalog_viewcable.asp?cnid=35 (called 18.11.2011).

[56] specifications of superconducting Niobium coaxial cables
http://www.docstoc.com/docs/39235766/Superconducting-semi-rigid-coaxial-cable (called 22.11.2011).

[57] specifications of Rosenberger flexible RF cables
https://www.micro-coax.com/secure/MCDlgCableDetails.aspx?Cable=UFA210A (called 18.11.2011).

[58] specifications on Teledyne Reynolds flexible RF cables
http://www.teledynereynolds.co.uk/ (called 18.11.2011).

[59] general information on Cobalt
http://en.wikipedia.org/wiki/Cobalt (called 09.11.2011).

[60] M. Radlmeier, Breitbandspektroskopie ferromagnetischer Mikrostrukturen bei tiefen Temperaturen. Diploma thesis, Technische Universität München (2010).

[61] C. J. Oates, F. Y. Ogrin, P. C. Riedi, S. L. Lee, G. Smith, and T. Thomson, J. Magn. Magn. Mater **242-245**, 402 (2002).

[62] Z. Frait, Czech. J. Phys. B **11**, 360 (1961).

[63] KUHNE LNA BB amplifier
http://www.kuhne-electronic.de/en/products/low-noise-amplifiers/ku-lna-bb-202-a.html (called 20.10.2011).

[64] P. E. Seiden, Phys. Rev. **133**, 3A (1964).

[65] Lakeshore low temperature hall porbe specifications
`http://www.lakeshore.com/mag/hs/hsts.html` (called 11.11.2011).

[66] R. Gross, *Festkörperphysik-Vorlesungsskript* (TU München, 2009).

[67] R. Orbach, J. Appl. Phys. **33**, 2144 (1962).

[68] B. H. Clarke, K. Teweedale, and R. W. Teale, Phys. Rev. **139**, 6A (1965).

[69] M. Sparks, J. Appl. Phys. **38**, 3 (1967).

[70] B. L. Rhodes, S. Legvold, and F. H. Spedding, Phys. Rev. **109**, 5 (1958).

[71] general information on Holmium
`http://en.wikipedia.org/wiki/Holmium` (called 17.11.2011).

[72] M. Sparks, Phys. Rev. Lett. **22**, 1310 (1969).

[73] J. M. D. Coey, *Magnetism and Magnetic Materials* (Cambridge University Press, Cambridge, 2010).

[74] J. F. Annett, *Superconductivity, Superfluids and Condensates* (Oxford University Press, New York, 2004).

[75] P. Bushev, A. K. Feofanov, H. Rotzinger, I. Protopopov, J. H. Cole, G. Fischer, A. Lukashenko, and A. V. Ustinov, arXiv: **1102**, 3841 (2011).

[76] P. F. Herskind, A. Dantan, J. P. Marler, M. Albert, and M. Drewsen, Nat. Phys. **5**, 494 (2009).

[77] D. Walls and G. J. Milburn, *Quantum Optics* (Springer-Verlag, Berlin, 2008).

[78] D. E. Kaplan, Phys. Rev. Lett. **14**, 254 (1965).

Acknowledgement

I would like to express my thanks to all people who helped and supported me during the time of my diploma thesis at the Walther-Meissner-Institut. I sincerely thank:

Prof. Dr. Rudolf Gross, for the opportunity of this diploma thesis and this great year at the WMI. For his markedly good lectures on solid state physics and low temperate physics, always inspiring me, during my study.

Dr. Hans Hübl, for being a remarkably good advisor and mentor. For letting me partake in his experience on physics, and teaching me the instruments of physics. For his elaborate discussions on measurement results and the mechanisms behind them. For always encouraging me and my work, and pave the way for my PhD position, and future science carrier.

Dr. Sebastian T. B. Gönnenwein, who introduced me to the magnetics group of the WMI, via his seminar on "*Spin Mechanics and Spin Dynamics*", and such got to this diploma thesis. And of course for his colorful dialogs, mostly about physics.

Fredrik Hocke, for his supervision during my thesis. For teaching me the handling of a dilution refrigerator. For introducing me to the work in the clean room, and how to manufacture micro-structured samples. For his insightful discussions, allowing me to see things from new perspectives.

Matthias Althammer, for teaching me the handling of the MORIA cryostat, and helping me with its peculiarities. For being a great office mate, and his discussions on physics and non-physics.

Mathias Weiler, for his help with the measurement program. For the discussions on FMR, and also being a great office mate.

All members of the magnetics group at the WMI who supported me and my work.

Dr. Karl Neumaier, for his kind help with the handling of the dilution refrigerator, further increasing my understandings of these cooling systems.

Robert Müller, for the renewal and expansion of my once learned knowledge about metal working.

Every person at the WMI, for a great time during the last year.

My fellow students Marco Halder and Sascha Mülbrandt, for the recreational coffee breaks, and the interesting insights on their works.

All my friends, for their support and encouragement, and patience with me during the last weeks of my diploma thesis.

And most of all, my parents and family, for their unswerving faith in me and my goal to become a physicist. Without them, all this would not have been possible. Many thanks.